Dc transport and optical measurements on the charge-density-wave compounds $(K,Rb)_{0.3}(Mo,W)O_3$

Dissertation zur Erlangung des Doktorgrades
der Mathematisch-Naturwissenschaftlichen
Fakultät der Universität Augsburg

vorgelegt von
Ali Khairi Abdul-Qader Al-Hadeethi

November 2012

Erstgutachter:	Prof. Dr. C.A. Kuntscher
Zweitgutachter:	Prof. Dr. Bruetting

Tag der mündlichen Prüfung: 26.04.2013

Contents

1 Introduction

This work is focusing on one-dimensional conductors, whose electrical conductivity is high only along one crystallographic axis. Nevertheless the anisotropy in the electrical conductivity is not necessarily the indication of the one-dimensional character. One-dimensional conductors do satisfy the following conditions: $l_{\parallel} \geq d_{\parallel}$ and $l_{\perp} \ll d_{\perp}$, where $l_{\parallel}$ and $d_{\parallel}$ are the electron mean free path and the interatomic distance along the one-dimensional axis, respectively. While $l_{\perp}$ and $d_{\perp}$ are the ones perpendicular to the one-dimensional axis. [1] Once it had been able to synthesize one-dimensional conductors, experimental studies in the beginning of 1970's have started to investigate them. Those experimental studies have given birth to many phenomena, regarding one-dimensional materials. An important phenomenon is the Peierls phase transition, which is a metal to insulator transition with an associated formation of a charge-density-wave (CDW). Also it has been observed that the CDW does carry current, enhancing the electrical conductivity of the material along the one-dimensional axis. [1] The phenomenon of the CDW was first theoretically predicted by Peierls in 1950s and first observed in 1970s. Since that date CDWs have been being observed in many inorganic low-dimensional compounds: [2]

1. The transition-metal chalcogenides for example TaS_2, $NbSe_3$, and TaS_3.
2. The transition metal bronzes ($A_{0.3}MoO_3$ where the alkali metal A can be K, Rb, or Tl).

In ordinary text books of solid state physics, they always start with a one-dimensional conduction band to explain the properties of metal and semiconductors for the sake of simplicity. Also I would mention here that the close cooperation with chemists has been always important to understand the physics of materials. [1] Three transition metal oxides ($K_{0.3}MoO_3$, $(K_{0.5}Rb_{0.5})_{0.3}MoO_3$, and $K_{0.3}Mo_{0.99}W_{0.01}O_3$) are studied in this thesis. A short theoretical description of a simple one-dimensional metal, a short overview of materials exhibiting CDWs, and the physical properties of our studied samples are presented in Chapter 2. The introduction to the experimental techniques (the infrared spectroscopy, low-temperature reflectivity measurements technique, dc transport measurements technique, and other techniques) used to investigate our studied samples are presented in Chapter 3. The analysis methods, required for extracting the physical information together with the obtained data are presented in Chapter 4. A discussion about the obtained data is presented in Chapter 4 too. Finally summarizing the findings of this work is presented in Chapter 5.

2 Theory

2.1 Introduction

2.1.1 Dimensionality

In contrast to Marcuse's one dimensional man, it was fashionable some time ago to adore physicists who could think in four dimensions. Any object exists in the three-dimensional space of our every day life. Each object has a length, width, and thickness and therefore is considered to be three-dimensional. But some objects like dishes have a greater length and width than thickness and therefore they look flat and may be considered to be two-dimensional. Similarly some other objects such as wires and snakes look one-dimensional. Also the motion of an object could be considered as one- or two-dimensional like a train on a trail or a boat on a river, respectively. So as a conclusion of what is written above; one- and two-dimensional objects and one- and two-dimensional motions of objects seem to be more common for us than their three-dimensional existence. In solid state physics we can treat solids either as objects or as the space, where electrons and phonons do exist. The layers of a crystal, the ab-plane of graphite for an example, can be considered as two-dimensional objects with some interaction between them or the two dimensional space where electrons move easily. [3]

2.1.2 Approaching one-dimensionality from outside and from inside

There are two approaches to low-dimensional or quasi low-dimensional systems in solid state physics: [3]

1. Geometrical shaping as an "external" approach.
2. Increase of anisotropy as an "internal" approach.

If electrons are confined in a box, quantum mechanics tell us that the electrons can have only discrete values of kinetic energy. The energetic spacing of the eigenvalues depends on the dimensions of the box; the smaller the box the larger the spacing (see Fig. 2.1). This relation is shown in Eq. 2.1. [3]

$$\Delta E_L = h^2/2m(\pi/L)^2 \tag{2.1}$$

Where $\Delta\mathrm{E}_L$ is the spacing and L is the length of the box. The Fermi level is the highest occupied state (at absolute zero). If the energy difference between the Fermi level and the next level is much larger than the thermal energy ($\Delta\mathrm{E}_L \gg \kappa_B\mathrm{T}$), then we have only completely occupied and completely empty levels and the system is an insulator. A thin wire is a small box for electronic motion perpendicular to the wire axis, but it is a very large box for electronic motion along the wire axis. Hence in two dimensions (radially) the wire represents an insulator, while in one dimension (axially) it is a metal. [3]

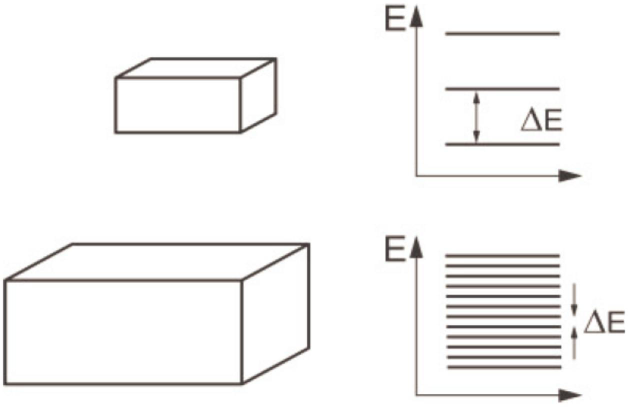

Figure 2.1: Electrons in small and large boxes and energy spacing of the eigenstates. [3]

The internal approach to one-dimensional solids comprises the gradual increase of anisotropy. In crystalline solids the electrical conductivity is often different in different crystallographic directions. If the anisotropy of the conductivity is very large in one direction and almost zero in the two perpendicular directions, a nearly one-dimensional conductor could result. [3]

2.1.3 Peculiarities of one-dimensional systems

Strictly one-dimensional systems behave unusual, i.e., they look *pathological* [3]. Real systems look less pathological, which means that real systems are just quasi one-dimensional systems and not strictly one-dimensional systems. Ideal systems have chains of infinite length. Also the chains of the ideal systems do not show imperfections. While real systems have chains of finite rather than infinite length. Also the chains of real systems show some imperfections such as kinks, twists, bends, or impurities because they do not exist in a perfect vacuum. [3]

Let us talk about some trivial aspects of one-dimensionality to make it clear for our understanding:

1. Bond percolation: almost everybody, who has the driving licence has painfully experienced driving a car behind a very slow truck on a one side mountain road (*obstacles can never be circumvented* [3]). This fact can be explained in terms of the bond percolation. *Bond percolation means the microscopic paths from one side of the sample to the other side* [3]. The idea of the bond percolation can be understood by a grid (Fig. 2.2), where bonds are cut randomly. If we imagine that the grid is a two-dimensional lattice, then a few cuts change the electrical conductivity a little bit. This will lead to the percolation threshold, which is the percentage of bonds enough to ensure electrical conductivity in the sample. The higher the percolation threshold, the lower the dimensionality. [3]

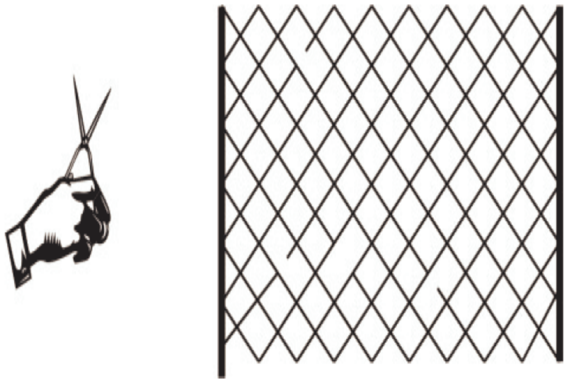

Figure 2.2: Bond percolation demonstrated on a two-dimensional grid, where bonds are successfully cut in a random way. [4]

2. Another aspect of one-dimensionality is the low connectivity: each atom is connected to two other atoms on the right- and left-hand sides. While in three-dimensional systems there are additional connections to another neighbors in the back and front and some other neighbors above and below. A consequence of the low connectivity is the strong electron-lattice coupling. This means that if we break the bonds between two atoms, then the sample will split into two parts. So in the case of one-dimensional systems, the percolation threshold is

100 percents. Normally complete breaking of bonds does not happen (usually one bond of the double bond in the system). [3]

2.2 Crystal structure of one-dimensional systems

The simplest lattice is a one-dimensional lattice, which is a line of equidistant atoms (see Fig. 2.3). So there is no need to consider the angular positions of atoms in a strictly one-dimensional lattice. Atoms are arranged in a zigzag line in many real one-dimensional systems, as illustrated in Fig. 2.4. Such a zigzag chain can be distorted by introducing some defects as illustrated in Fig. 2.5, where the perfect alternation vanishes. [3]

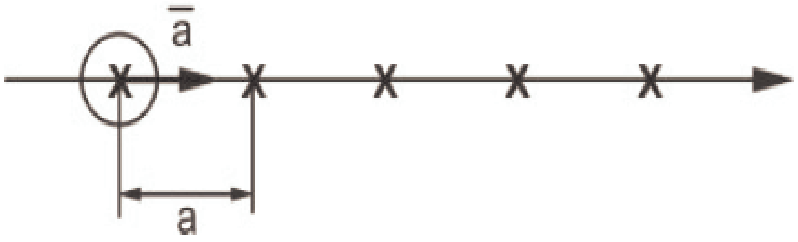

Figure 2.3: One-dimensional lattice. [3]

Figure 2.4: Zigzag chain. [3]

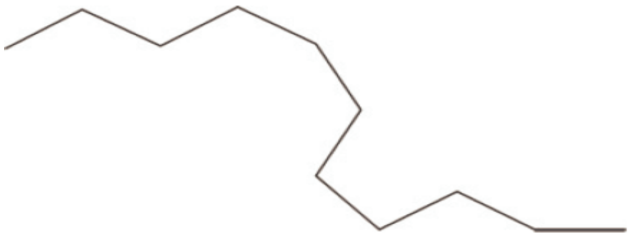

Figure 2.5: Zigzag chain with defects. [3]

Electron-lattice coupling, Peierls transition:

Fig. 2.6 illustrates the simplified structure of polyacetylene, where the chain is lined rather than zigzagged with a bond angle of 180° rather than 120°. In this system single and double bonds do alternate (see Fig. 2.6). Single bonds are weaker than the double bonds and accordingly the single bond is longer than the double bond. As mentioned before, the atoms in one-dimensional solids have only two neighbors (see Fig. 2.3). So if one single bond is broken, then the system will break apart. But if one double bond is weakened by breaking one of its bonds, then the system will be distorted because of the lengthening of the corresponding interatomic distance (see Fig. 2.6). [3]

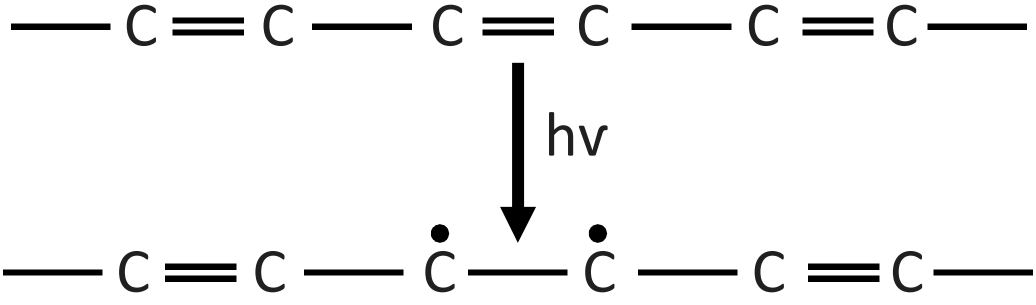

Figure 2.6: Bond scission in polyacetylene to demonstrate the strong electron - lattice coupling in one - dimensional solids. [3]

Peierls in 1955 showed that the metallic mono-atomic chain is not stable. A metal to insulator phase transition takes place at low temperatures with the formation of a charge-density-wave (CDW). [5]

2.3 What is a charge-density-wave?

Metals suffer from a phase transition, when they are cooled down. Iron and nickel become ferromagnetic, while lead and aluminum become superconductors. A lot of quasi-one-dimensional metals have been discovered a long time ago, which show a different type of phase transition at certain temperatures; they become charge-density-wave (CDW) conductors. [2] CDW materials do share the same architecture; electrons can move freely along the chains axis, while they move less freely along the perpendicular axes. This kind of architecture gives these materials the quasi-one-dimensional property, which is crucial for the formation of the charge-density-wave. Blue bronze is a good example of that. Corner-sharing MoO_6 octahedra form chains along the b axis (see Fig. 2.7), along them electrons can move freely as mentioned above. [2]

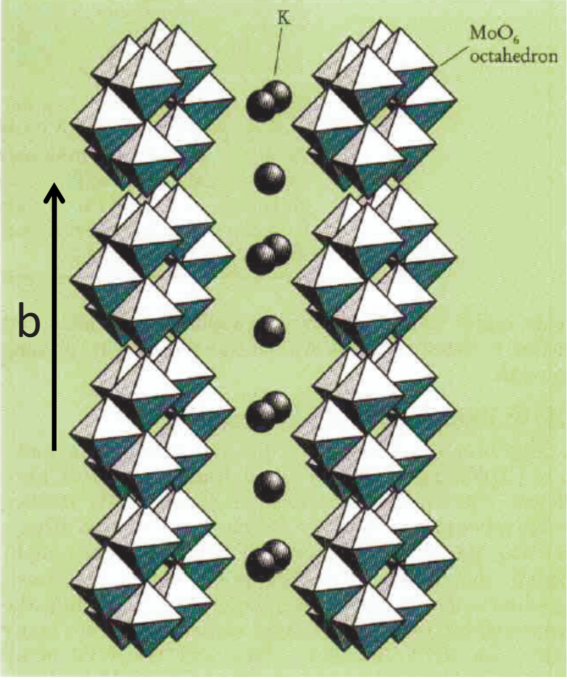

Figure 2.7: Crystal structure of the pure blue bronze. [2]

In a one-dimensional-metal, the lattice atoms are equally spaced. Consequently, the electron density is highly uniform (see the upper part of Fig. 2.8). The lattice atoms suffer from a periodic distortion, when the temperature is lower than the phase transition temperature. As a result of that, the electron density is not uniform any more; instead it gets also periodically modulated (see the lower part of Fig. 2.8). The modulation of the electron density is called charge-density-wave (CDW). [2]

The electron-phonon interaction mentioned above results in an instability of the metallic Fermi surface, opening an energy gap at the Fermi surface (see the lower part of Fig. 2.8). The CDW wavelength λ_c is π/k_F, where k_F is the Fermi wave vector. Peierls and Fröhlich have been the first to predict all that. [2] CDW has been experimentally observed in many quasi-low-dimensional organic and inorganic compounds ($NbSe_3$, TaS_2, $TaSe_2$, $(NbSe_4)_{3.33}I$, and $(TaSe_4)_2I$). [6] The electronic transport in the CDW state has two contributions:

1. Normal charge carriers, which are thermally excited across the gap (like in semiconductors). [2]

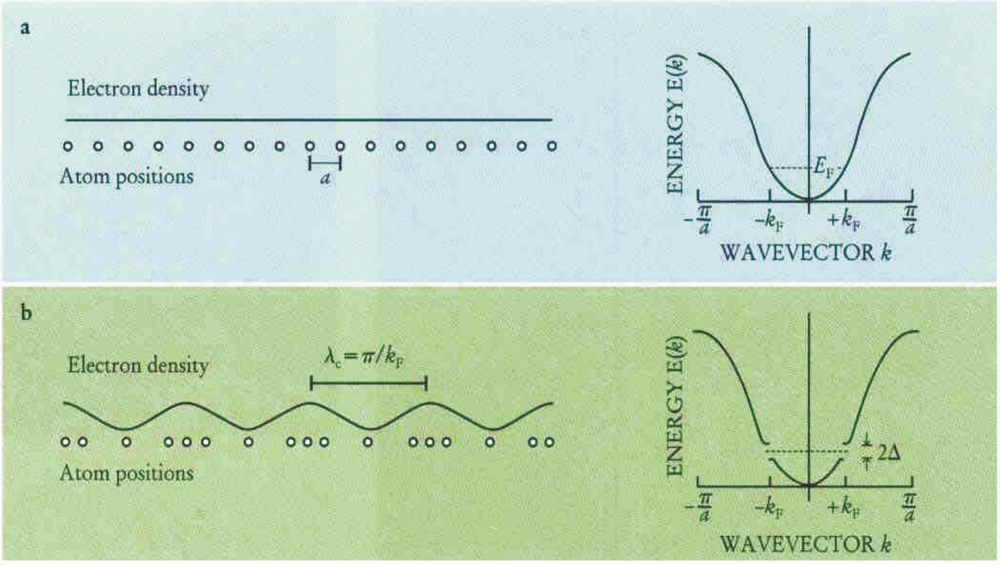

Figure 2.8: Peierls distortion in a one-dimensional metal. [2]

2. The collective response of the CDW condensate (CDW sliding): the CDW condensate interacts with the underlying lattice and lattice imperfections (impurities and defects). Consequently, the CDW condensate can not move easily because it is pinned. [2] But if one applies an electric field exceeding a critical value E_T along the chains direction, then the CDW begins to slide through the crystal. The CDW sliding contributes additionally to the electronic transport, increasing the conductivity of the sample. The CDW sliding is easily observable, because it results in a nonlinear I-V response. [7]

Below around 40 K in $K_{0.3}MoO_3$, a more complicated I-V response is also observable after exceeding a second threshold field $E_T{}^*$. Above $E_T{}^*$, a sharp increase of current by many orders of magnitude is observable. [8–10]

2.4 Molybdenum oxide bronzes

Because of the unusual properties of these bronzes, they have been investigated extensively. They do show quasi one-dimensional character and charge-density-wave (CDW) driven metal to insulator phase transition. Because of the anisotropic structure of these compounds, oriented single crystals are needed to extract the physical properties. In the next sections the physical properties of this type of bronzes are explained.

2.4.1 Introduction

The term bronze was originally coined for Na_xWO_3 compounds by Wohler in 1825. [11] It is now applied to many crystalline phases of the transition metal oxides, which are usually ternary compounds of the type $A_xM_zO_y$ with intense color, metallic luster, and metallic or semiconducting properties. Ternary bronzes have been prepared, in which M is Ti, V, Nb, Mn, Ta, W, Mo, or Re and A is H, NH_4^+, an alkali, an alkaline earth, a rare earth, group 11, group 12, or other metal ion. [6]

The basic structural unit of the transition metal oxides is a cluster, which is a transition metal (M) surrounded by group VI and VII elements. So, transition metal oxides can be considered as condensations of clusters. Fig. 2.9 depicts a trigonal prism with 6 selenium atoms at the corners and a niobium atom at the center as an example. Fig. 2.10 shows the MoO_6 octahedron as another example, which is the basic structural unit of the molybdenum oxide bronzes (A_xMoO_3). [3]

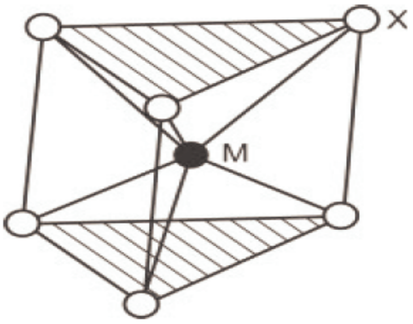

Figure 2.9: Trigonal prism of $NbSe_6$ as basic structural unit of low-dimensional niobium-selenide solids. [3]

The clusters condense by sharing corners, edges, or faces. The prismatic condensation is shown in Fig. 2.11, where edge-sharing results in the layered structure of $NbSe_2$ and face-sharing leads to the fibrillar $NbSe_3$. $NbSe_3$ is one of the most important inorganic quasi one-dimensional solids, which has been studied for understanding the charge-density-wave phenomena. [3]

$(MX_4)_nY$ is an example of a corner-sharing cluster condensation (see Fig. 2.12), where M is a transition metal such as Ta or Nb, X is a chalcogenide such as Se or S, and Y represents halogen ions between the fibers. [3]

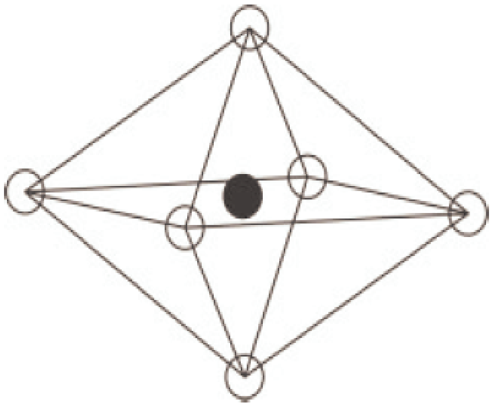

Figure 2.10: MoO_6 octahedron as the basic unit of blue bronzes. [3]

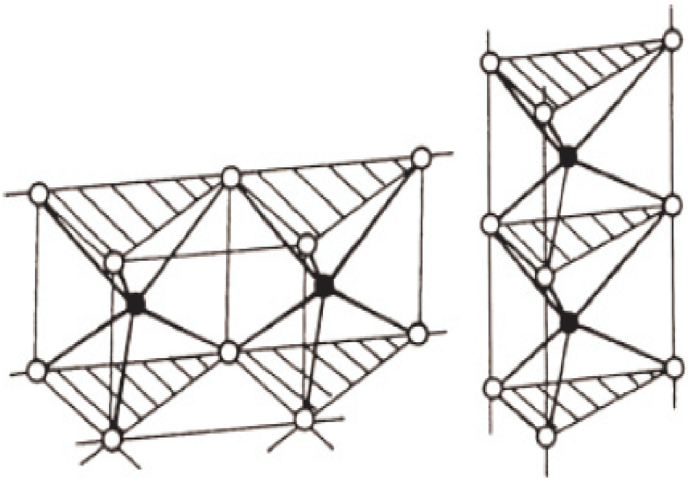

Figure 2.11: Condensation of MX_6 prisms to form layers by edge-sharing (left) or fibers by face-sharing (right). [12]

Molybdenum oxide bronzes are classified into several categories: [6]

1. Blue bronzes ($A_{0.3}MoO_3$), where A is K, Rb, or TI.
2. Red bronzes ($A_{0.33}MoO_3$), where A is Li, K, Rb, Cs, or TI.
3. Purple bronzes ($A_{0.9}Mo_6O_{17}$), where A is Li, Na, K, or TI.

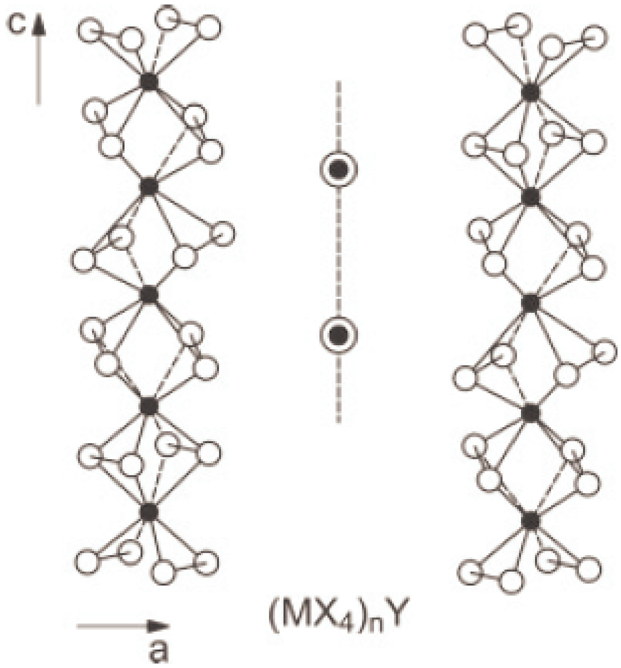

Figure 2.12: Crystal structure of $(MX_4)_nY$. [3]

2.4.2 Preparation

The first molybdenum oxide bronzes, $K_{0.3}MoO_3$, $K_{0.33}MoO_3$, and $Na_{0.9}Mo_6O_{17}$, have been synthesized by Wold et al. [13] by electrolytic reduction of A_2MoO_4-MoO_3 melts under carefully controlled conditions of temperature and composition. Later this technique has been used to synthesize several alkali metal molybdenum bronzes in the single crystal form [14–27]. [6] Most of the single crystals prepared by using this technique has the following features: [6]

1. They are platelet-like and they can cleaved parallel to the plate plane.
2. Their size is $(5 \times 2 \times 1)$ mm^3.

A stoichiometric mixture of A_2MoO_4, MoO_3, and MoO_2 in evacuated quartz tubes has been used to prepare all of the known alkali metal molybdenum oxide bronzes in the polycrystalline form at the proper temperature for each of them [28–36]. [6]

More recently a temperature gradient flux technique has been developed to grow good quality single crystal Mo oxide bronzes. In this technique a stoichiometric mixture of reactants is being used to synthesize a variety of Mo oxide bronzes according to Eq. 2.2 [31–36]: [6]

$$nA_2MoO_4 + 2(1-n)MoO_3 + nMoO_2 \longrightarrow 2A_nMoO_3 \tag{2.2}$$

The procedure of this technique is as below [31–36]: [6]

1. The reactant mixture must be first pelletized.
2. Then it is sealed in a quartz tube.
3. Then the tube is placed in a two zone furnace. The charge end of the tube is placed in the hot zone of the furnace, while the other end of the tube is placed in the cold zone of the furnace.
4. Then by setting the cold zone of the furnace to ~50 °C lower than the hot zone of the furnace, a temperature gradient along the quartz tube is achieved.
5. Then the charge do melt throughout the quartz tube. Accordingly, single crystal bronzes do grow at different temperature regions in the tube. The type and quality of each crystal depend on the value of n and the temperature gradient along the tube.

2.4.3 The blue bronzes

Crystal structure:

The structure of the potassium blue bronze has been first solved by Graham and Wadsley. [37] More recent X-ray diffraction structural refinement of $K_{0.3}MoO_3$, $Rb_{0.3}MoO_3$ [38] and $Tl_{0.3}MoO_3$ [27] has confirmed the work of Graham and Wadsley; it has shown that all of blue bronzes form with monoclinic symmetry, in space group C2/m. [6] The structure is built of clusters. The cluster consists of ten edge/corner-sharing distorted MoO_6 octahedra [see Fig. 2.13(a)]. The clusters share corners along the monoclinic b axis to form MoO_6 octahedra infinite chains held together by the A atoms [see Fig. 2.13(d)], while the clusters form two-dimensional MoO_6 octahedra infinite sheets perpendicular to the monoclinic b axis by sharing corners too [see Fig. 2.13(c)]. Fig. 2.13(b) illustrates the top view of the MoO_6 octahedra sheets (please notice that the unit cell is drawn with doubled c axis). [39]

X-ray diffraction studies have shown that the cleavage plane includes the monoclinic b axis and the [101] axis, i.e., the plane illustrated in Fig. 2.13(c) is the cleavage plane. [15]

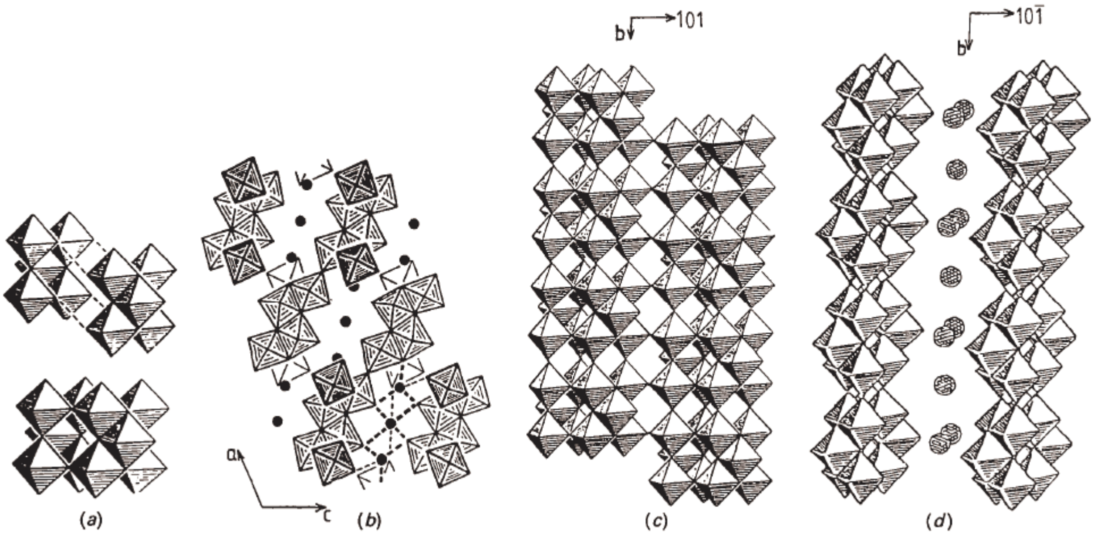

Figure 2.13: Schematic diagrams for the basic structure of the blue bronze, described in the right-handed Graham and Wadsley (1966) cell with doubled c axis. (a) $Mo_{10}O_{30}$ cluster. (b) View along $[0\bar{1}0]$, showing the upper view of octahedra slabs. The oxygen octahedra are outlined. (c) View along $[10\bar{1}]$, four unit cells along b are drawn. (d) Prespective view along [101], four unit cells along b, infinite sheets of $Mo_{10}O_{30}$ clusters are seen. [39]

The *A* atoms are arranged between the MoO_6 octahedra chains along the monoclinic b axis as below: [37]

Two different arrangements of the *A* atoms do alternate along the monoclinic b axis; (i) *A*(1) arrangement, in which the *A* atom is surrounded by ten oxygen atoms. Eight of the oxygen atoms do form an irregular cube and two oxygen atoms are sitting in the centers of two opposing faces of the irregular cube. So the A atom in this case has ten neighbors and sits in the center of the irregular cube. (ii) *A*(2) arrangement, in which the *A* atom sits in the center of a trigonal prism of six oxygen atoms with an additional oxygen atom (the seventh one) at the center of one face of the prism. Fig. 2.14 illustrates the alternation of the *A* atoms arrangements. [37]

There three different sites in each cluster, where the MoO_6 octahedra are located. These sites are labeled as Mo(1), Mo(2), and Mo(3). Four MoO_6 octahedra are located at the Mo(2) site, four MoO_6 octahedra are located at the Mo(3) site, and two MoO_6 octahedra are located at the Mo(1) site. Zachariasen's method has shown that over 80 percents of the 4d electron density is on the Mo(2) and Mo(3) sites in the infinite MoO_6 octahedra chains along the monoclinic b axis. This is the reason why the eight

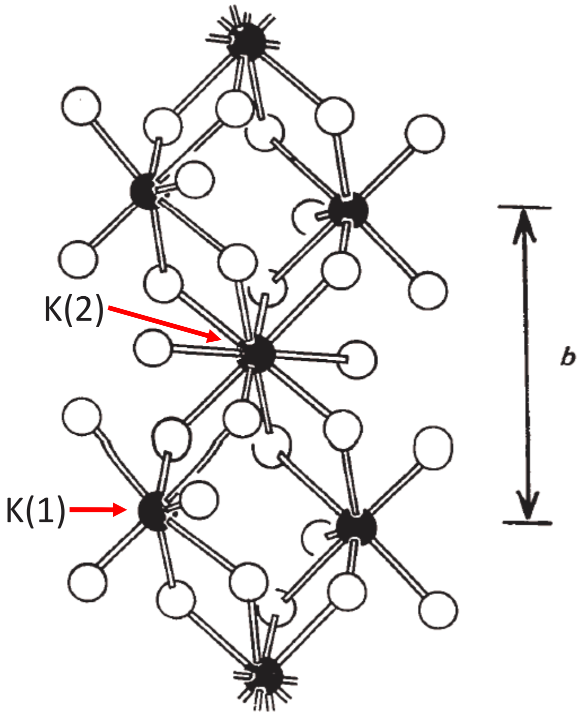

Figure 2.14: Three-dimensional view of the chain of oxygen polyhedra around the K cations. [37]

MoO_6 octahedra at sites Mo(2) and Mo(3) are called the chain octahedra. [27,38,40,41] Fig. 2.15 shows the locations of the chain octahedra in the cluster.

Unit cell parameters of three known $A_{0.3}Mo0_3$ phases are given in Table 2.1. There are significant changes in a, c, and β. While the monoclinic b axis remains more or less the same with increasing the effective size of the A atom. This suggests that the chainlike coupling of the corner-sharing MoO_6 octahedra along the monoclinic b axis is independent of the nature of the A atom in blue bronzes. [6]

	$K_{0.3}MoO_3$	**$Tl_{0.3}MoO_3$**	**$Rb_{0.3}MoO_3$**
Unit cell space group	**Monoclinic C2/m**	**Monoclinic C2/m**	**Monoclinic C2/m**
a (Å)	**18.2587 (7)**	**18.486 (1), 18.543 (3)**	**18.6354 (3)**
b (Å)	**7.5502 (4)**	**7.5474 (6), 7.567 (4)**	**7.555 (1)**
c (Å)	**9.8614 (4)**	**10.0347 (7), 10.067 (2)**	**10.094 (2)**
β (degree)	**117.661 (4)**	**118.377 (6), 118.39 (2)**	**118.842 (5)**

Table 2.1: Unit cell parameters of $A_{0.3}MoO_3$ bronze phases. [6]

Finally, the crystal structure of $K_{0.3}MoO_3$ is illustrated in detail in Fig. 2.16 where

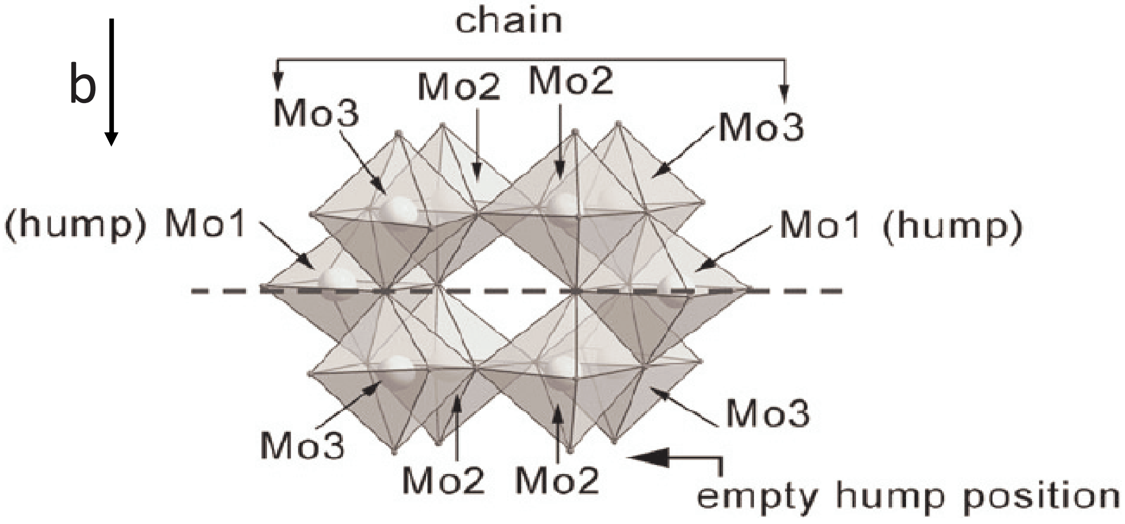

Figure 2.15: The $Mo_{10}O_{30}$ cluster. [41]

the zigzag chain structure of K ions and the MoO_6 octahedra are shown very clearly. [42]

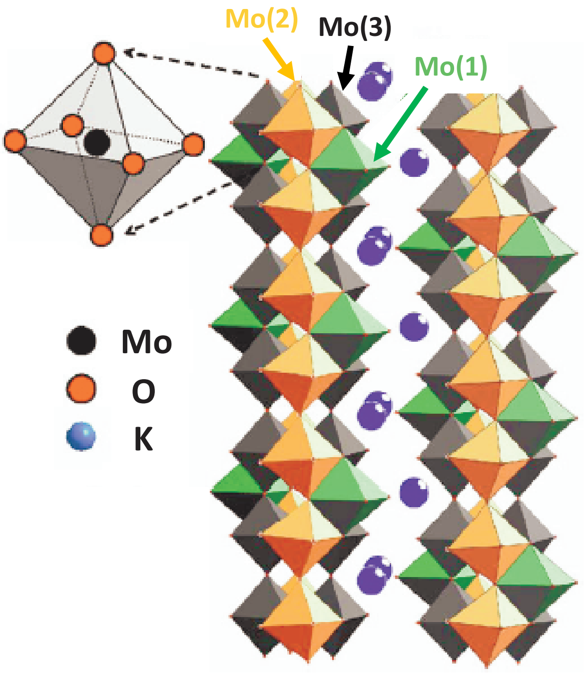

Figure 2.16: The crystal structure of $K_{0.3}MoO_3$. [42]

Band structure:

Goodenough has developed a band structure for ReO_3. [43] Dickens et al. [44] has been the first to apply it to the molybdenum bronzes. Fig. 2.17 illustrates the schematic diagram of the band structure of the molybdenum bronzes.

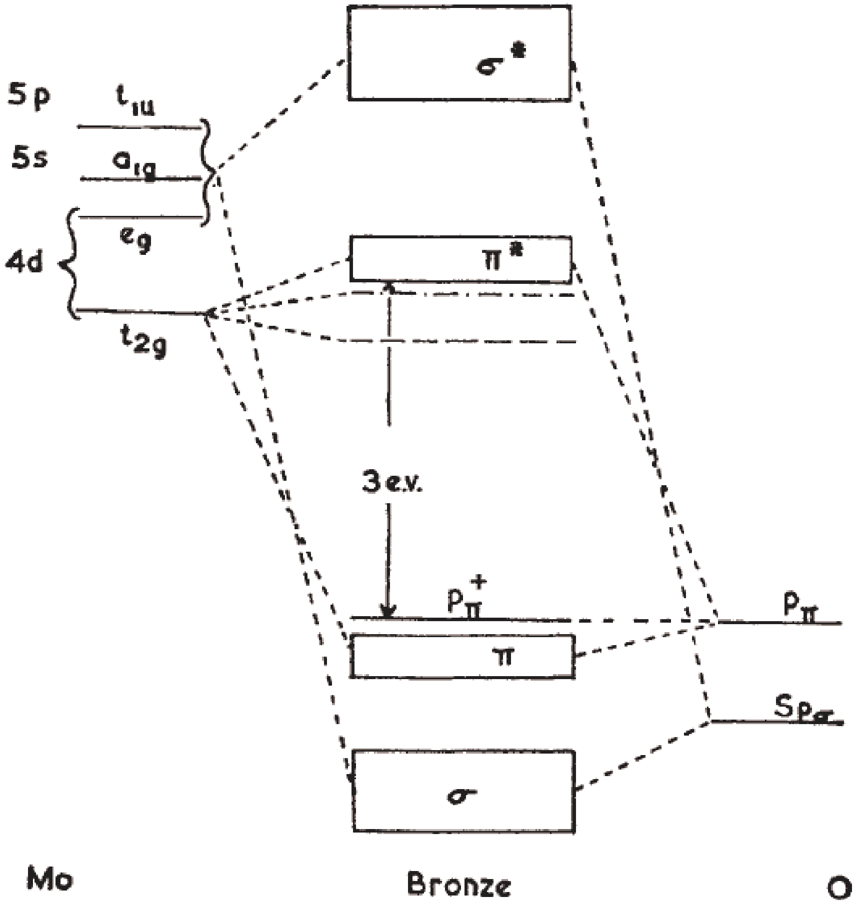

Figure 2.17: Electronic energy level diagram for the molybdenum bronzes. [44]

The following explanation is considered for a discrete MoO_6: The 5p, 5s, and 4d (e_g) orbitals of the central molybdenum atom combine with six sp hybrid orbitals of the oxygen atoms (one orbital per one oxygen atom). The combination of these orbitals gives rise to six bonding σ and six anti-bonding σ^* molecular orbitals (see Fig. 2.17). The discrete energy levels, which result from the combination above broaden into bands in an extended lattice. Also three of the surrounding oxygen $p\pi$ orbitals per each octahedron combine with the central molybdenum 4d (t_{2g}) orbitals. The combination of these orbitals results in bonding π and anti-bonding π^* orbitals (see Fig. 2.17).

Again the discrete energy levels, which result from this combination broaden into bans in an extended lattice. Now we have three of the oxygen pπ orbitals per each octahedron, which do not combine with any molybdenum orbitals. So non-bonding pπ^* levels are formed by those orbitals (see Fig. 2.17). The π band, σ band, and pπ^* levels form the valence band. While π and π^* bands form the conduction band. The energy gap is about 3 eV (see Fig. 2.17). It is assumed in the case of the molybdenum bronzes (A_xMoO_3) that the A cations act as electron donors to the conduction bands of the MoO_6 octahedra, so that they transfer their valence electrons to the conduction band. This charge transfer fills the conduction bans partially, signaling the metallic behavior. [44]

The A cations do not participate in the formation of the band structure, as confirmed by several experiments [45, 46]. Fig. 2.18 shows the density of states of $K_{0.3}MoO_3$. The participation of the molybdenum and oxygen atoms in the formation of the band structure is very observable. Also it is clear that the potassium atoms are not involved in the formation, confirming that the potassium atoms act as electron donors to the conduction bands of the MoO_6 octahedra. [47]

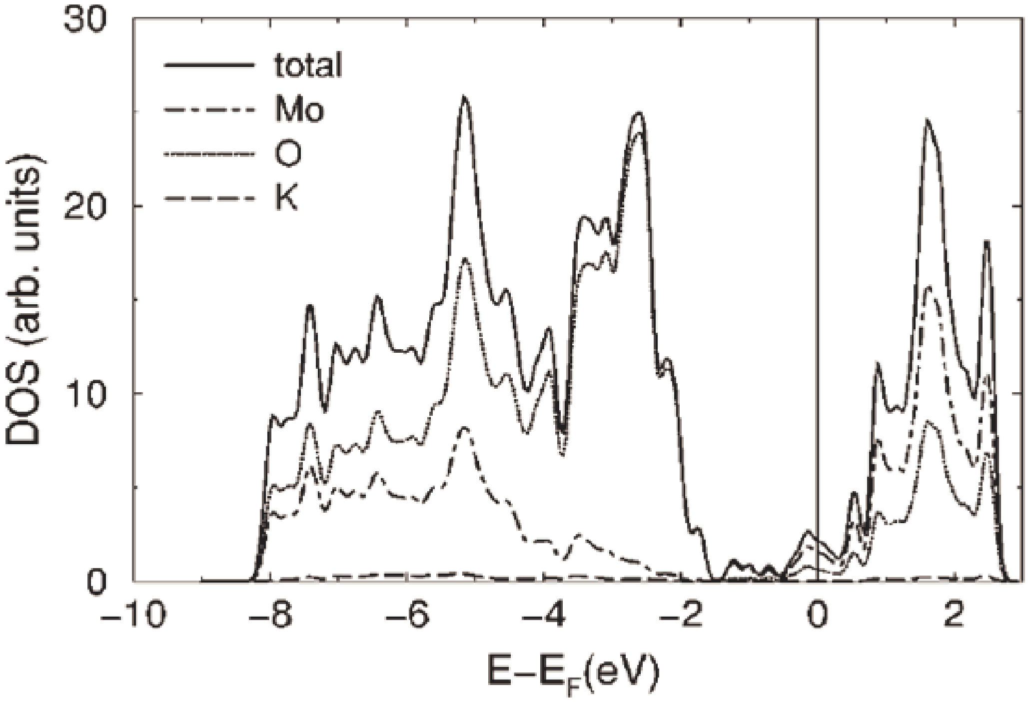

Figure 2.18: Total and projected density of states of $K_{0.3}MoO_3$ projected onto the Mo, O, and K sites. [47]

Physical properties of blue bronzes:

(a) Metal - semiconductor Peierls transition:

Wold et al. [13] and Bouchard et al. [14] have been the first to study the electrical properties of $K_{0.3}MoO_3$ and found the existence of a metal to semiconductor transition near 180 K. Later, it has been shown by Perloff et al. [15] that the electrical resistivity is highly anisotropic. Fig. 2.19 is a plot of logρ vs. 1000/T of $K_{0.3}MoO_3$ along the [010] ($\parallel$ b axis) and [102] ($\perp$ b axis) directions (see Fig. 2.13).

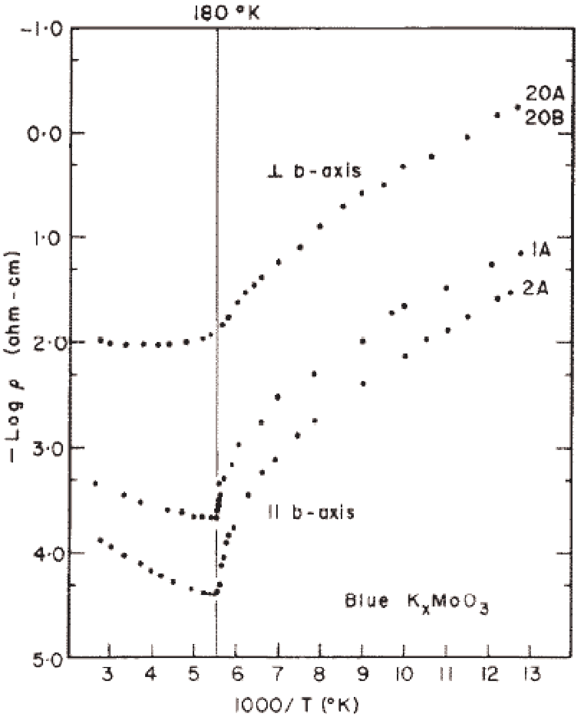

Figure 2.19: Plot of logρ vs. 1000/T representative samples of the blue potassium molybdenum bronze oriented parallel to the monoclinic b-axis (along the [010] direction) and perpendicular to the b-axis (along the [102] direction). [15]

Samples 20A and 20B have been cut from the same crystal and they have given similar results as shown in Fig. 2.19, while samples 1A and 2A have been cut from different crystals and they have given different results as plotted in Fig. 2.19; this suggest that the absolute value of the electrical resistivity in $K_{0.3}MoO_3$ is different in different specimens. Also it is obvious from Fig. 2.19 that the difference in the specific resistivity for the two crystallographic directions signals the conductivity anisotropy. [15] More recently, Brusetti et al. [20] has measured the electrical resistivity of $K_{0.3}MoO_3$ and shown that the electrical resistivity of $K_{0.3}MoO_3$ is about an order of magnitude larger along [102] in the plane of the layers than along b and even higher perpendicular to the layers. Similar anisotropy has been found for $Rb_{0.3}MoO_3$ [48] and $Tl_{0.3}MoO_3$ [33] (see Fig. 2.20 and Fig. 2.21).

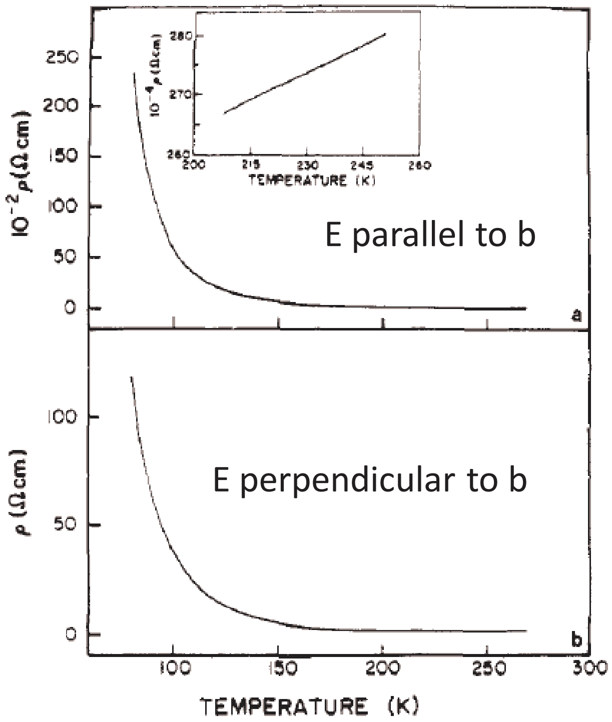

Figure 2.20: Temperature variation of the resistivity of $Tl_{0.3}MoO_3$: (a) current and voltage in the plane of the platelet crystals parallel to the b axis; (b) current and voltage perpendicular to b and the cleavage plane. Inset shows the details of decreasing resistivity with decreasing temperature in the range ~(250-200) K. [33]

Fig. 2.20 shows the temperature dependence of the specific resistivity along the [010] (|| b axis) and $[10\overline{2}]$ (perpendicular to b and the cleavage plane) directions (see Fig. 2.13). The room temperature conductivity, measured along the b-axis 8.4 X 10^2 $(\Omega cm)^{-1}$ is ~250 times larger than that perpendicular to b and the cleavage plane 260 $(\Omega cm)^{-1}$. While Fig. 2.21 shows the specific resistivity (logarithmic scale) versus temperature along the [010] (|| b axis) direction (see Fig. 2.13), along [102] (⊥ b axis) direction (see Fig. 2.13), and perpendicular to b and the cleavage plane ($[10\overline{2}]$ direction) (see Fig. 2.13). The resistivity is one order of magnitude larger along the plane of layers

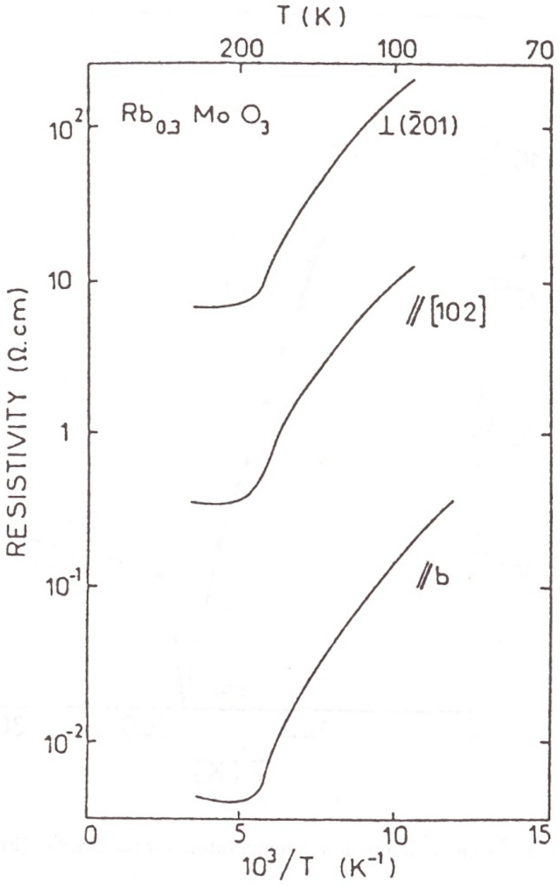

Figure 2.21: Electrical resistivity (logarithmic scale) of $Rb_{0.3}MoO_3$ versus inverse temperature along b, [102] and perpendicular to the octahedral layer's plane. [48]

(along [102]) than along b, while the resistivity is higher perpendicular to b and the cleavage plane. More recently anisotropy ratio ($\sigma_{\parallel}/\sigma_{\perp}$) of 100:10:1 has been given by Bruetting et al. [49]. Raman scattering studies have shown the appearance of a line at ~50 cm^{-1} below 180 K, which has a temperature dependence as illustrated in Fig. 2.22. This has been related to the Peierls phase transition. [50]

A specific heat anomaly has been found between 150 K and 190 K in $K_{0.3}MoO_3$ and $Rb_{0.3}MoO_3$. Fig. 2.23 shows the specific heat versus temperature of $K_{0.3}MoO_3$, in which the anomaly has been found at 179 K. This has been also attributed to the Peierls phase transition. [51]

A thermal expansion anomaly has been found in $K_{0.3}MoO_3$. Fig. 2.24 shows the temperature dependence of the linear thermal expansion, normalized to the length at

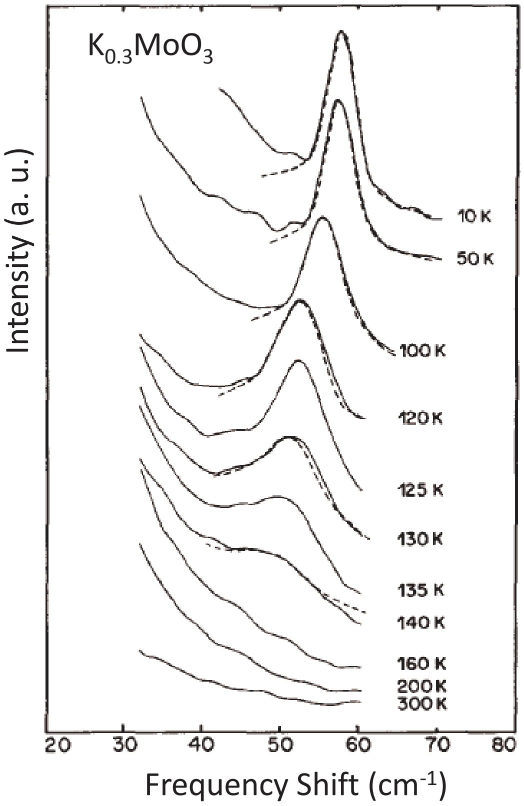

Figure 2.22: Raman spectrum of $K_{0.3}MoO_3$ at various temperatures. [50]

4.2 K along the monoclinic b axis. The hump at 183 K along the monoclinic b axis has been related to the Peierls phase transition. [52]

X-ray diffraction studies by Sato of the blue bronzes have shown that the phase transition at 180 K is a Peierls phase transition, resulting in a semiconducting state with the formation of an incommensurate CDW. [53] Sato et al. [54] and Fleming et al. [55] have found a clear incommensurate-commensurate transition of the CDW near 100 K. Several investigators [14, 20, 23, 25, 56, 57] have measured the magnetic susceptibility of $K_{0.3}MoO_3$ and found it to be highly anisotropic as shown in Fig. 2.25. The drop near 180 K in the magnetic susceptibility has been related to the Peierls phase transition as well. [6]

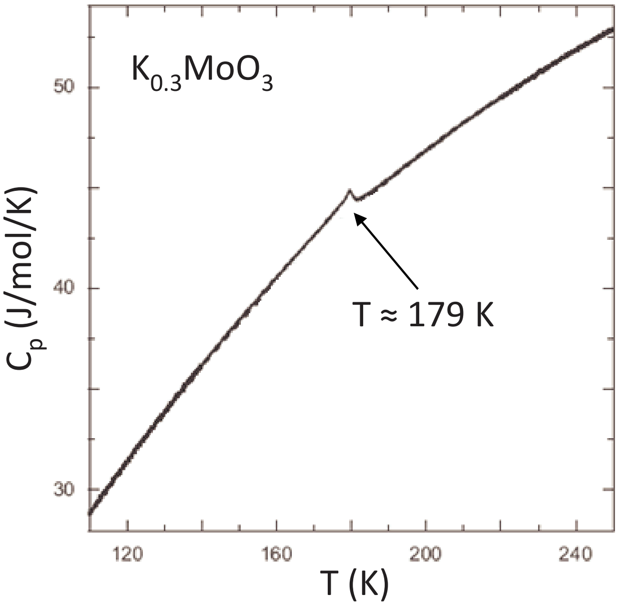

Figure 2.23: Specific heat versus temperature of $K_{0.3}MoO_3$. [51]

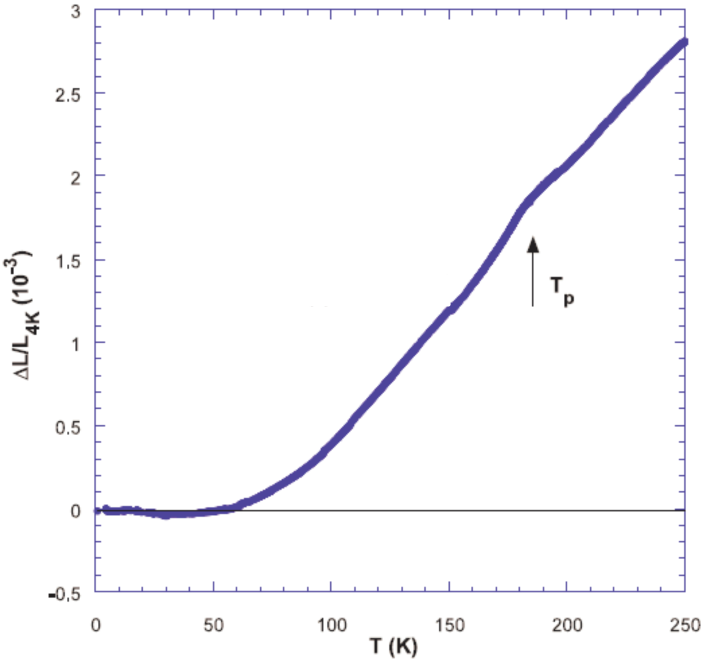

Figure 2.24: Linear normalized thermal expansion along b axis of $K_{0.3}MoO_3$. [52]

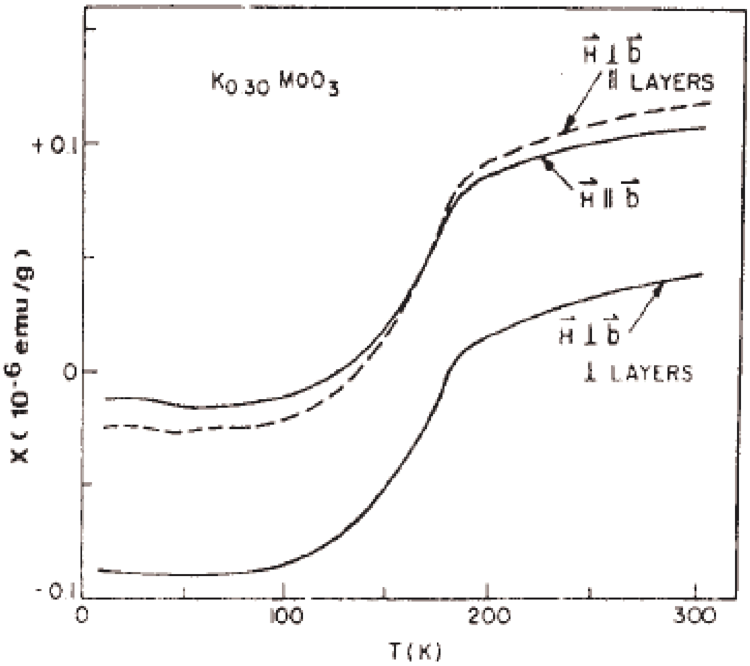

Figure 2.25: Temperature variation of the magnetic susceptibility of $K_{0.3}MoO_3$ as a function of temperature for different orientations of the magnetic field. [23]

(b) Moving charge density wave:

The motion of an incommensurate CDW, which does enhance the conductivity has been first suggested by Fröhlich. [57] Nonlinear conductivity due to the sliding of CDW was first reported in $NbSe_3$ in 1976 by Monceau. [58] Since then, a big amount of work has been devoted to the study of cliding CDWs and associated phenomena in NbS_3, TaS_3, $(TaSe_4)_2I$, and the blue bronzes. [58] Dumas et al. [59] has been the first to show that $K_{0.3}MoO_3$ shows a nonlinear transport due to the CDW sliding. Since then, the blue bronzes have been studied extensively. [58] There are two phenomena associated with the moving CDW, which are very important to mention in this thesis:

(i) Non-linear dc conductivity:

Fig. 2.26 shows the current-voltage (I-V) characteristics of $Tl_{0.3}MoO_3$ at T = 77 K. The figure shows actually two regimes:

1. Ohmic regime below a threshold electric field (E_T) of more or less 300 mV/cm, where current is proportional to voltage linearly as shown in Fig. 2.26. In the

Ohmic regime the CDW is "pinned" to the underlying lattice either by impurities and lattice defects or by commensurability. [58]

2. Above E$_T$, the CDW is "depinned". It starts to move under the applied electric field and contributes additionally to the conductivity. The movement of CDW results in a nonlinear (non-Ohmic) current-voltage response, as illustrated in Fig. 2.26. [58]

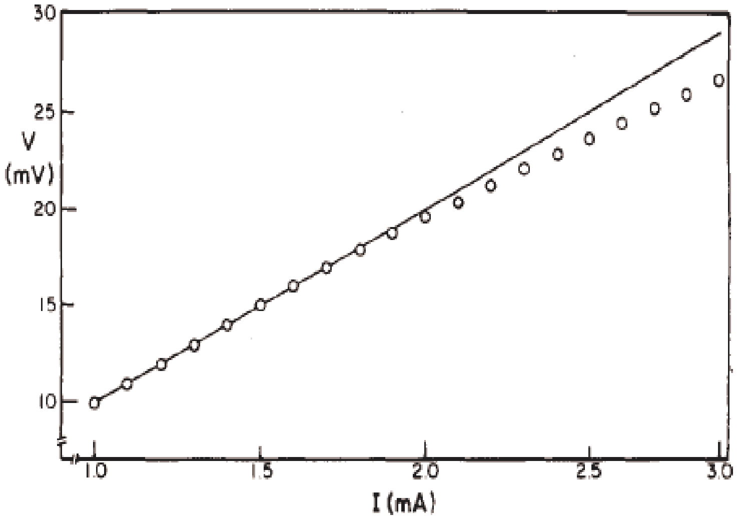

Figure 2.26: Current-voltage characteristics of $Tl_{0.3}MoO_3$. [58]

(ii) CDW metastability:

The metastability of the CDW has been first seen by Gill in $NbSe_3$. [60] After that Fleming in Ref. [61] has confirmed the CDW metastability in the same compound; he has shown the nonlinear voltage response of $NbSe_3$ to a series of unidirectional and bidirectional constant-current pulses, exceeding the threshold near the transition temperature 46 K. He has seen that samples of moderate threshold fields (around 15 mV/cm) have a very slow response, rise time on the order of 50 μs, to a series of unidirectional pulses. While a voltage overshoot occurs with a fast rise time, when the pulse has the opposite polarity in the case of alternating bidirectional pulses. Interestingly; he has found that the response to a series of unidirectional pulses is much faster, when the sample has a better impurity (threshold field of about 8 mV/cm). But the voltage overshoot remains the same even if the sample has a better purity. The upper part of Fig. 2.27 shows the response to a series of three unidirectional pulses, where a very fast response has been observed. While the lower part of Fig. 2.27 shows the response, when the current direction is reversed; a fast response with a voltage overshoot beyond the steady state value, followed by a slow decay to the steady state value has been observed. The voltage overshoot has been related to the existence of a metastable state, induced by the CDW sliding. It seems that the CDW has a memory, meaning that the CDW knows in which direction it last has moved (the so called memory effect). So by reversing the current direction, an instantaneous increase of the conductivity above the steady state value occurs. The momentary enhanced conductivity is held responsible for the voltage overshoot in the response. [61]

So it seems that the current pulse in excess of threshold leaves the CDW in a metastable state, which depends on the current direction. The CDW knows the direction it last has moved, as mention above. So if the next pulse has the opposite polarity, then a transition from one metastable state to another occurs. That results in a lower resistance, which holds for the voltage overshoot with a fast response initially (see Fig. 2.27). The nature of the metastable state is still puzlling, but it could be due to the distortion of the magnitude of the CDW wave vector or the CDW amplitude while moving along random pining centers. [61] No significant change in the magnitude of the overshoot has been observed, when the interval between the current pulses had been increased from 3 μs to 25 minutes. This indicates a long lifetime of the metastable state, meaning that the CDW takes a long time to relax to the ground state. [60]

Also I would mention here another observed phenomena in the work of Fleming, which is the periodic voltage response. In Fig. 2.27 one can see an integral number of wavelengths in each pulse, which holds for the periodic voltage response. The periodic voltage is a fraction of the nonlinear voltage; it occupies 10 percents of the nonlinear voltage for current pulses twice the threshold as the case in Fig. 2.27, while it approaches 100 percents of the nonlinear voltage for current pulses very close to the threshold as the case in Fig. 2.28. Therefore, the CDW in this case stops completely whenever it moves one unit length; the unit length might be one CDW wavelength (around 14 Å) or it might be the separation between discommensurations (around 500 Å). [61]

Later Fleming and Schneemeyer in Ref. [62] have found that the nonlinear response of $K_{0.3}MoO_3$ is qualitatively similar to that of $NbSe_3$. Fig. 2.29 shows the comparison between the responses of the two materials. In the case of $K_{0.3}MoO_3$ the linear response has not been subtracted, since the nonlinear contribution is very large. As a consequence of that the voltage overshoots in the $NbSe_3$ experiment appear as voltage lags in the $K_{0.3}MoO_3$ experiment. In the case of $K_{0.3}MoO_3$ if the next pulse has the same polarity, then the response is fast. And if the next pulse has the opposite polar-

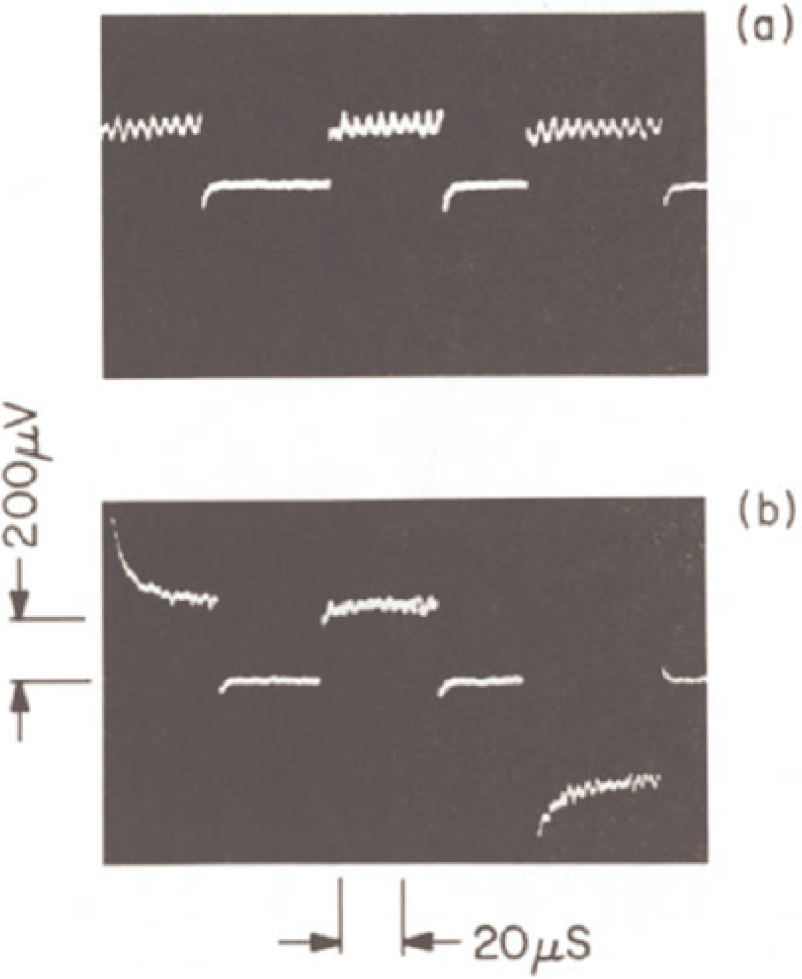

Figure 2.27: The non-linear response of $NbSe_3$ with a threshold field of 8 mV/cm to (a) uni-directional and (b) bi-directional current pulses. T = 46 K. The rise time of the voltage is limited by the instrumental resolution. If the preceding pulse has opposite polarity, a large overshoot of the non-linear voltage is observed. [61]

ity, then the response is initially fast with a lag and then it gets slower than that of $NbSe_3$. The decay time in the case of $NbSe_3$ is 20 μs, while in the case of $K_{0.3}MoO_3$ the rise time is 500 μs (see Fig. 2.29). Actually the very slow response in $K_{0.3}MoO_3$ can cause a large hysteresis loops in the I-V response curve at low frequencies, when the current direction is reversed. [62]

Interestingly; the slow response has been also seen in $K_{0.3}MoO_3$ even if the current

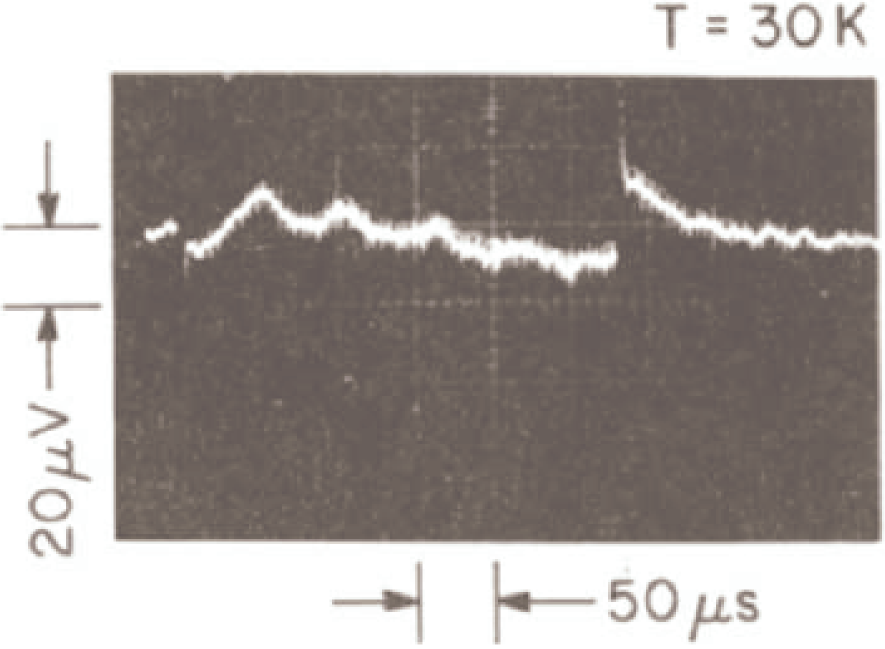

Figure 2.28: The non-linear response of $NbSe_3$ with a threshold field of 15 mV/cm at 34 K. Near threshold the periodic response comprises 100 percents of the non-linear voltage. [61]

direction is not reversed, as long as the pulses are in excess of threshold. This is attributed to the domain structure of the CDW; it is thought that the CDW is not rigid, instead it contains different domains. Each domain has its own pinning strength and phase. These domains are coupled to each other, so that the CDW does not start moving until all domains are depinned. If a voltage in excess of threshold is applied, then the phase shifts of the neighboring domains come to an arrangement and the whole CDW moves. If the applied voltage drops to zero, then the phase arrangement of the domains does relax to the zero-field phase arrangement. If the off interval is very short, then the domains will not have enough time to come back to the zero-field phase arrangement. In this case a very fast response is expected, when the next pulse comes. But if the off interval is long enough, then a very slow response is expected. That means that the phase arrangement takes some time, which is hold responsible for the slow response. [62]

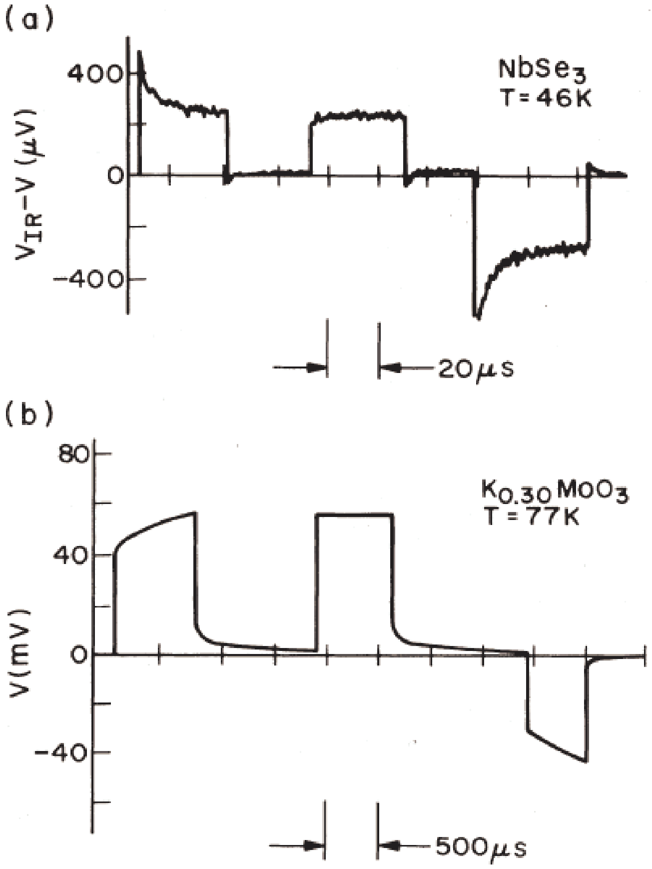

Figure 2.29: Comparison between response of $NbSe_3$ and $K_{0.3}MoO_3$ to a repetitive series of constant-current pulses consisting of two positive followed by one negative pulse. All pulses are in excess of threshold. Both materials show a slow response when the current direction is reversed. [62]

(c) Thermal memory effect:

The temperature dependence resistivity curve in blue bronze suffers from a hysteresis, while cooling down and warming up below the Peierls transition temperature. The hysteresis can be magnified by irradiating the sample, signaling the defect origin of that hysteresis. Also below the transition temperature a new phenomena takes place (the so called thermal memory effect). [63] Fig. 2.30 shows the resistance of an irradiated $K_{0.3}MoO_3$ in a log scale as a function of the inverse of temperature. The continuous lines show the cycle, when the temperature varying rate is constant. A relaxation of several hours at 90 K has been done. During the relaxation the resistance has increased, as shown in the figure. On cooling down they have observed a weakened temperature dependence after the relaxation time is over. While on heating up a broad anomaly has been observed next to the relaxation temperature, signaling the thermal memory effect. The heating up curve bends down to try following the slop of the cooling down curve, which has started from the relaxation temperature. Such anomalies can be also observed in the non-irradiated sample, but the effect is more than ten times smaller in temperature and resistance. [63]

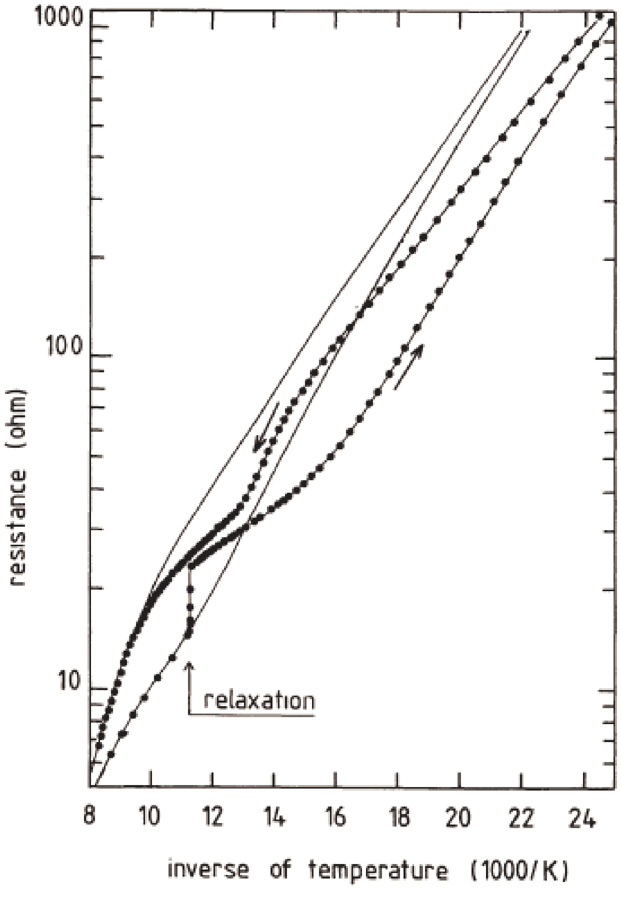

Figure 2.30: Resistance in a log scale as a function of the inverse of temperature for a potassium blue bronze irradiated with 2.5 MeV electrons at a dose of 12 mC/cm^2. The continuous line shows the cycle with the temperature varying at a constant rate. The arrow shows the relaxation for several hours at a bout 90 K. Note the weakened temperature dependence of resistance on cooling after the relaxation and, on heating, the anomaly when the relaxation temperature is approached. [63]

Optical studies of blue bronzes:

The optical reflectivity data of $K_{0.3}MoO_3$ and $Rb_{0.3}MoO_3$ obtained by Travaglini et al. [64] and Jandl et al. [65], respectively have established that above 180 K these bronzes are quasi-1D metals. A general introduction of optical properties of solids is given in the chapter of experiments. The optical conductivity of $K_{0.3}MoO_3$ has been measured, as mentioned above by Travaglini et al. [64] on single crystals for photon energies between 0.03 and 12 eV at temperatures from 10 to 300 K using a polarized light. The interpretation of the measured data says that this compound is a one-dimensional conductor at temperatures above 180 K and that the metal-insulator transition at 180 K is due to a Peierls transition, which results in a gap in the density of states. [64] The reflectivity spectra at 100 K and 300 K along b and perpendicular to it are shown in Fig. 2.31, where no significant temperature dependence has been found below 150 K.

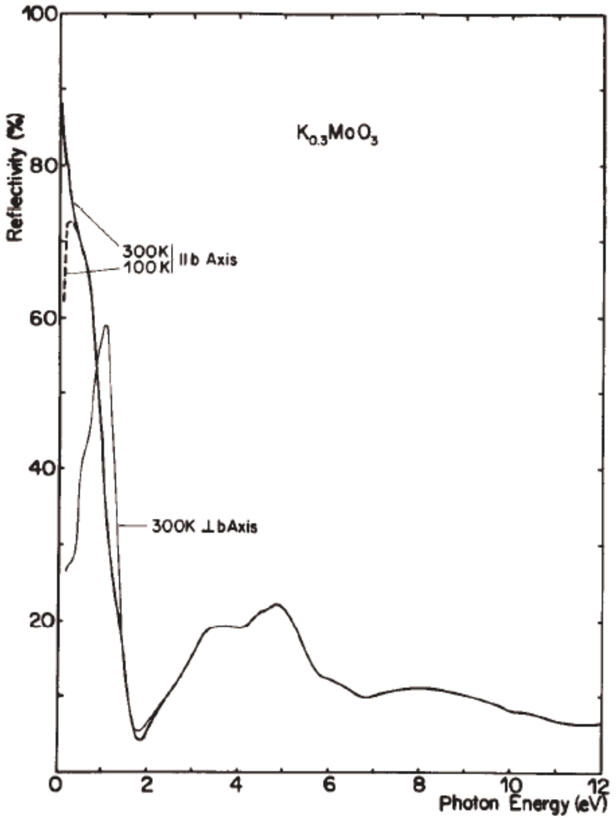

Figure 2.31: The reflectivity spectra of $K_{0.3}MoO_3$ at 300 K and 100 K along b and perpendicular to it. [64]

While Fig. 2.32 illustrates the reflectivity spectra at 100 K and 300 K along b and perpendicular to it in a small infrared (IR) spectral range, noticing that at 300 K the spectral range has been extended to about 1 meV (8.064 cm^{-1}). [64]

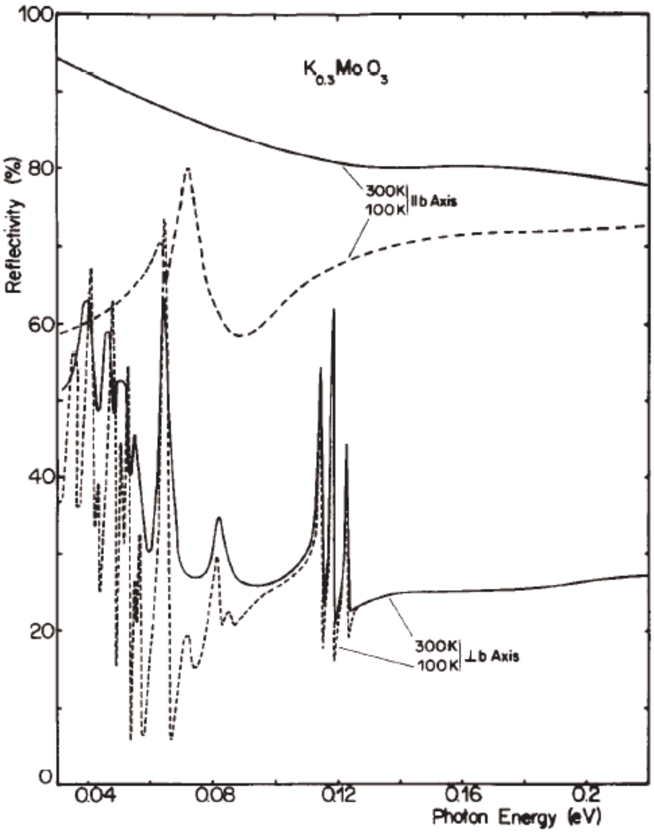

Figure 2.32: The reflectivity spectra of $K_{0.3}MoO_3$ at 300 K and 100 K along b and perpendicular to it in a small IR spectral range. [64]

In the visible spectral range (above 2 eV) there is no polarization dependence, while below 1 eV big changes happen. [64] Thus:

1. For the polarization (P) parallel to the monoclinic b axis, the material is a metal at room temperature with a plasma edge near about 1.3 eV (see Fig. 2.31). This is due to a carrier concentration, which results from a complete charge transfer of the valence s electrons of the alkali metal (K) into the π^* conduction band (see Fig. 2.17). [64]

2. While for P $\perp$ b the material is a semiconductor at 300 K with an absorption edge at about 0.5 eV and many sharp lines appear for photon energies below about 0.12 eV (see Figs. 2.31 and 2.32). [64]

3. At low temperatures the reflectivity for P $\perp$ b does not change qualitatively, but the lines do sharpen up (see Fig. 2.32). While for P $\parallel$ b a decrease in the reflectivity occurs below about 0.2 eV and two sharp peaks appear near about 0.07 eV (see Fig. 2.32). [64]

3 Experiments

The temperature-dependent infrared measurements presented in this work have been performed using a Fourier transform Infrared (FTIR) spectrometer (Bruker IFS66v/S). A reflection unit is coupled to the FTIR spectrometer, which enables the use of the sample compartment of the FTIR spectrometer for performing our low-temperature infrared measurements. So in this chapter the important information about infrared spectroscopy at low temperatures are explained, including the description of the reflection unit design. Also the techniques, which have been used to perform our dc electrical transport measurements are presented including the description of the design of an evaporation unit.

3.1 FTIR spectroscopy

3.1.1 What is FTIR spectroscopy?

FTIR is the abbreviation of **F**ourier **T**ransform **I**nfrared. FTIR spectroscopy has been an important technique to study a lot of materials for quite along time. In this technique, IR radiation is used. When the IR radiation is hitting the material surface, some of the IR radiation is reflected back by the surface and the rest is either absorbed by the material or transmitted through it. The reflection, absorption, and transmission IR spectra provide a molecular fingerprint of the material as illustrated in Fig. 3.1. Two unique molecular structures never give the same IF spectrum like any two fingerprints. This what actually makes the technique very important for investigating many materials. [66]

Older technology:

The dispersive IR instruments were the original ones. They do separate the IR individual frequencies by using a prism or a grating. The IR prism works exactly as the visible prism, which itself splits the white light into it colors (each color corresponds to one specific frequency). A grating is a better dispersive element, which better separates the individual IR frequencies. The detector measures the amount of intensity

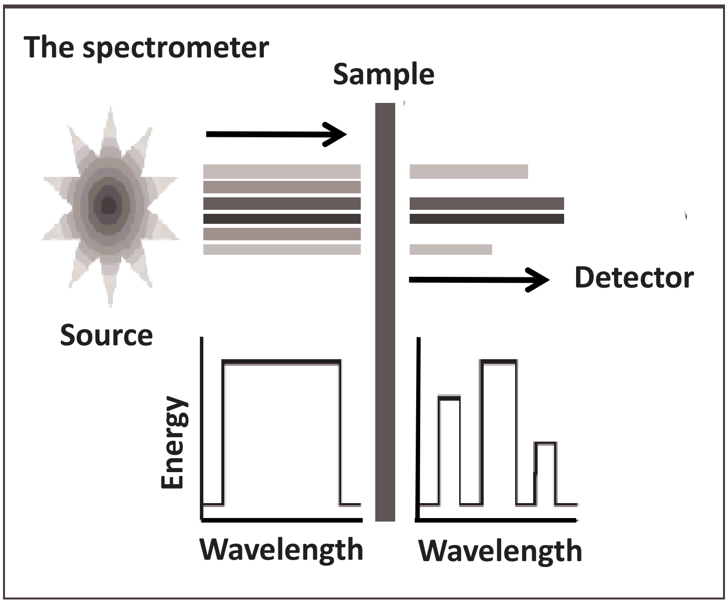

Figure 3.1: Schematic illustration showing that the FT-IR provides a molecular fingerprint. [66]

of each individual frequency, resulting in an IR spectrum which is a graph of intensity versus frequency. [66]

Why FTIR spectroscopy?

In order to be free of limitations due to old dispersive instruments, Fourier Transform Infrared Spectroscopy has been introduced. In dispersive instruments the scanning process is very slow, in which infrared frequencies are being measured individually. The low speed scanning process is the main limitation of dispersive instruments, which could take several minutes. The main optical devise in FTIR spectroscopy is the interferometer. It consists of the following parts (see Fig. 3.2): [66]

1. Fixed plane mirror.
2. Movable plane mirror.
3. Beam splitter.

The red dot in Fig. 3.2 is a monochromatic light source. When the light strikes the beam splitter, it gets split into two optical beams. One beam goes toward the fixed mirror, while the other one travels toward the movable mirror. The two beams

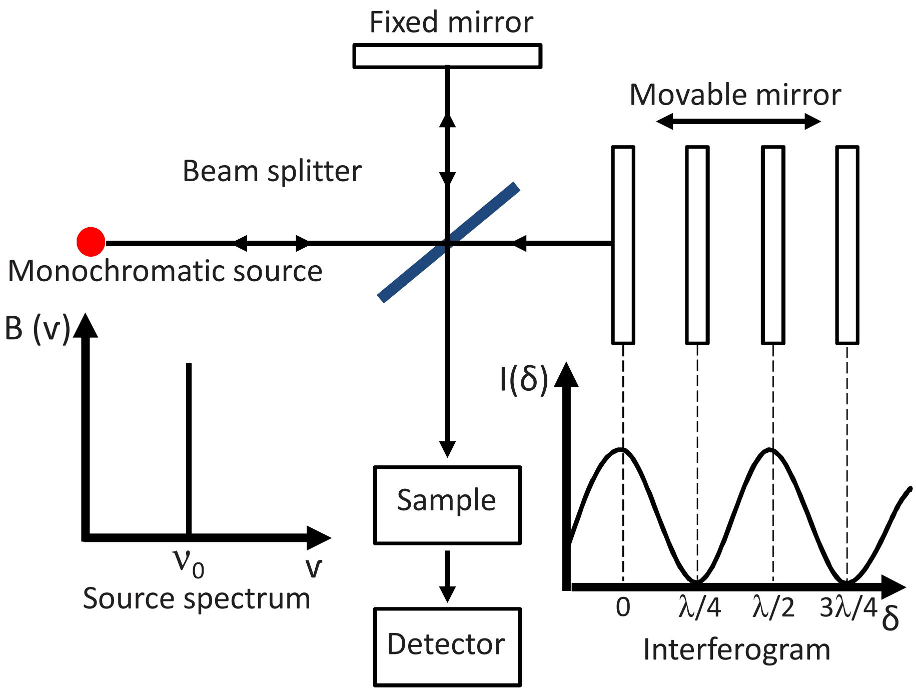

Figure 3.2: Schematic diagram, which explains the working principle of an FTIR spectrometer.

are then reflected back toward the beam splitter, at which they recombine. After that the recombined beams travel toward the detector. If the distance between the fixed mirror and the beam splitter equals to that between the later and the movable mirror, then the difference between the optical paths traveled by the two beams will be zero. But if the movable mirror is moved, then the optical path difference (δ) will not be zero. When the moved mirror is moved away from the beam splitter, the signal received by the detector (the interferogram) alternates between a maximum value and a minimum value. The maximum signal is achieved when (δ) is an integral multiple of the source wavelength (i.e., δ=nλ;n=0, ±1, ±2, etc.), while the minimum signal is obtained when (δ) is not an integral multiple of the source wavelength. Such an interferogram is illustrated in Fig. 3.2 for a monochromatic source. Eq. 3.1 describes the resulting interferogram as a cosine wave: [67]

$$I(\delta) = B(\nu)cos(2\pi\delta\nu) \tag{3.1}$$

where B(ν) is the intensity of the source as a function of frequency ν, while I(δ) is the intensity of the detector signal as a function of the optical path difference. If the source emits many frequencies, then each frequency will result in a cosine wave with its own periodicity. Then the resultant interferogram will be the summation of all cosine waves. So Eq. 3.1 will be written, as shown below: [67]

$$I(\delta) = \sum_{\nu_1}^{\nu_n} B(\nu_i) cos(2\pi\delta\nu_i) \tag{3.2}$$

Any infrared source emits a continuous spectrum, hence the summation is replaced by an integral as shown below: [67]

$$I(\delta) = \int_0^\infty B(\nu) cos(2\pi\delta\nu) d\nu \tag{3.3}$$

Using Fourier transformation, B(ν) can be derived from I(δ) as shown below: [67]

$$B(\nu) = \int_0^\infty I(\delta) cos(2\pi\delta\nu) d\delta \tag{3.4}$$

Fig. 3.3 illustrates a typical interferogram and the resulting spectrum. When δ=0 all cosine waves are in phase and therefore I(δ) has a maximum. As we move away from the maximum in either direction, the phase between the cosine waves is no longer zero and therefore they start to cancel each other. Consequently, the intensity goes into a series of lower amplitude oscillations. [66]

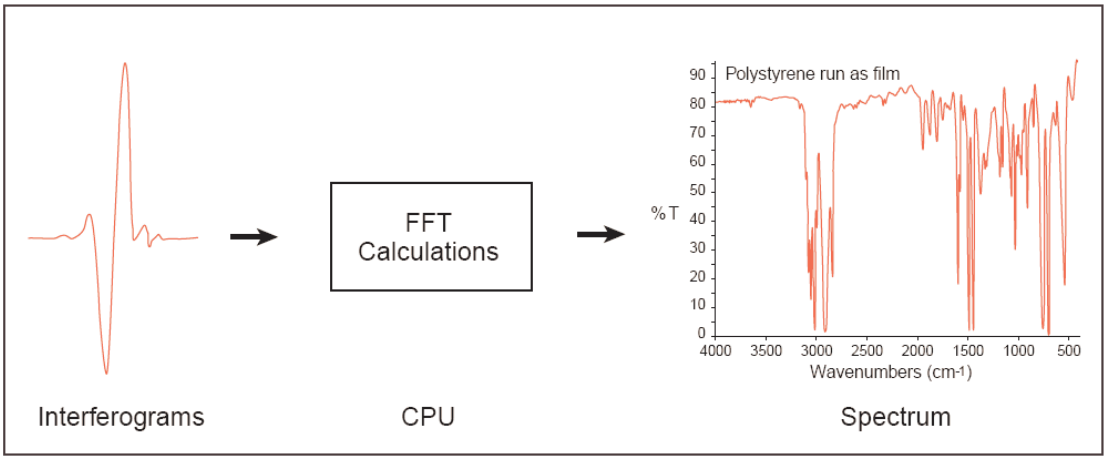

Figure 3.3: A typical interferogram and its corresponding spectrum in the MIR frequency range obtained in by FTIR spectrometer. [66]

Advantages of the FTIR spectroscopy:

Some of the major advantages of the FTIR spectroscopy over the dispersive technique include: [66]

- **Speed:** The measurements are fast to perform, because all frequencies are measured simultaneously. Most FTIR measurements take several seconds than several minutes.
- **Sensitivity:** Sensitivity is better in the FTIR spectrometer, because of many reasons:
  1. The employed detectors are much more sensitive.
  2. Too many scans can be done because of the fast scans. This reduces the noise.
- **Mechanical simplicity:** The only moving part in the instrument is the scanning mirror, so the probability of a mechanical breakdown is very low.
- **Internally calibrated:** The FTIR spectrometer involves a He-Ne laser as an internal wavelength calibration standard. So the instrument is self-calibrating. No need to calibrate it by the user. This advantage is called the Connes advantage.

Bruker spectrometer and the IR-microscope:

All optical IR measurements in this thesis have been performed using a Bruker IFS 66v/s infrared (IR) spectrometer. The schematic set-up is shown in Fig. 3.4. After the beam is reflected and focused by a spherical mirror, it passes through an aperture. The aperture wheel is sitting at the focus of the spherical mirror and the aperture size can be changed from 0.5 mm to 12 mm. Then the beam travels to the interferometer. The interferogram travels either to the IR microscope or to the sample compartment (see the movable plane mirror in the figure). The beam is focused in the sample compartment by a special mirror, where low-temperature reflection and transmission measurements can be performed. The the beam is sent to one of the detectors through a couple of mirrors. Since the radiation source, the beam splitter, and the detector do not cover the whole frequency range, hence they all need to be changed with each frequency range (see Table 3.1). The maximum resolution of the spectrometer is better than $\Delta\nu$=0.25 cm^{-1}. However, a resolution of $\Delta\nu$=4 cm^{-1} in the mid-IR range has been enough for the optical mid-IR measurements presented in this thesis. The spectrometer must be always evacuated at a pressure of 3 mbar, while measuring to avoid strong artificial absorptions below 5000 cm^{-1} due to water vapor and CO_2. [68,69]

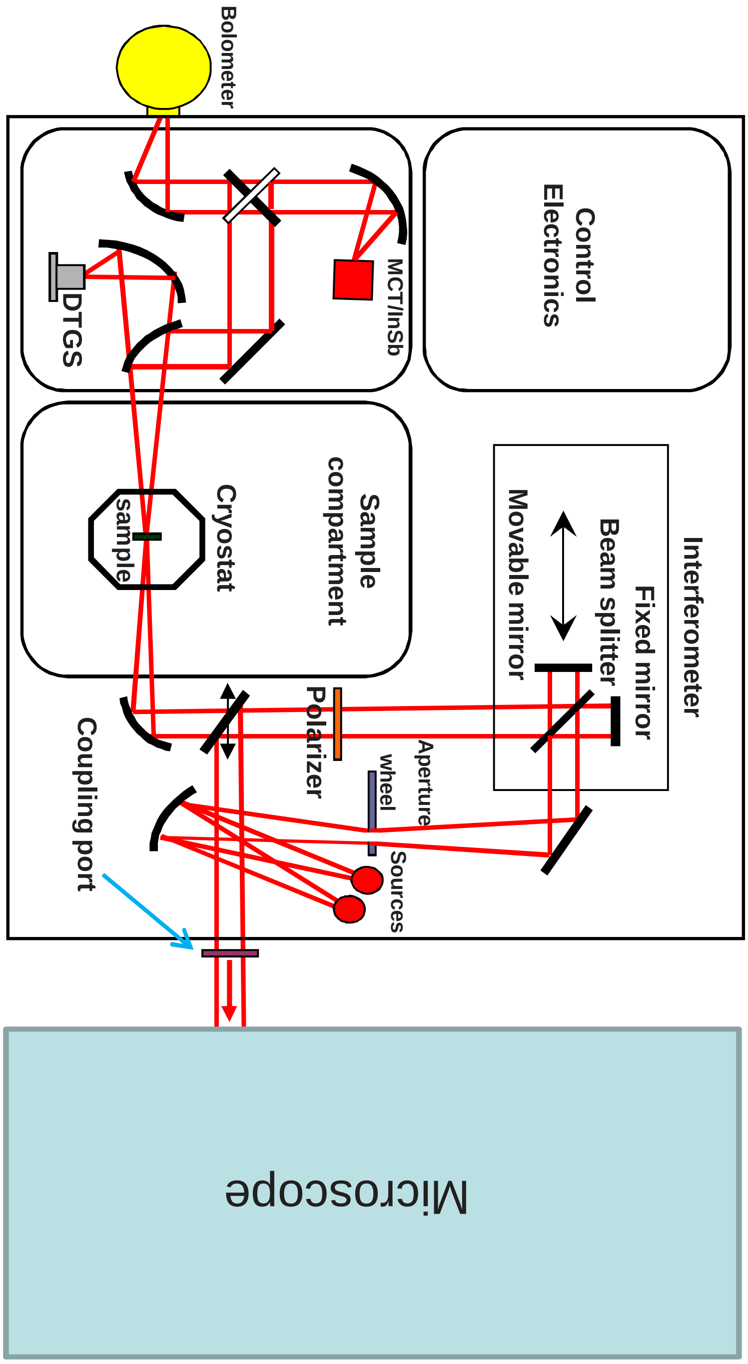

Figure 3.4: Bruker Spectrometer IFS 66v/s. [68]

The temperature-dependent optical mid-IR measurements presented in this thesis have been performed using the sample compartment of the spectrometer shown in Fig. 3.4, while the free standing optical mid-IR measurements at room temperature

Frequency range	**Source**	**Beam splitter**	**Polarizer**	**Detector**
Far infrared 10 - 700 cm^{-1}	Hg discharge lamp	50 μm Mylar/Ge 23 μm 6 μm	Polyethylene	Bolometer DTGS
Mid infrared 500 - 8000 cm^{-1}	Globar	KBr/Ge	KRS-5	MCT detector DTGS
Near infrared 2000 - 12000 cm^{-1}	Tungsten lamp	CaF_2	KRS-5	InSb detector
Visible/UV 10000 - 26000 cm^{-1}	Tungsten lamp	CaF_2	Prism	Si diode GaP diode

Table 3.1: Sources, beam splitters, polarizers, and detectors used for different infrared frequency ranges in the Fourier transform Infrared spectrometer. [68]

have been performed using the IR-microscope illustrated in Fig. 3.5. All optical elements illustrated in Fig. 3.5 are described in Tables 3.2 and 3.3. Actually the two tables are self explanatory.

In the IR-microscope the beam is focused on the sample using two Schwarzschild objectives (see Fig. 3.5). The advantage of using the Schwarzschild objectives is to eliminate the aberrations in the measured frequency range. A visible light from an additional source can be sent to an ocular, where the sample can be viewed (see Fig. 3.5). Thus one can choose the proper position on the sample surface for the measurements. Apertures from 0.3 mm to 3.75 mm are used, so the beam size can also be changed in the IR microscope. It is not possible to evacuate the IR microscope, so instead it is flooded with nitrogen gas to avoid strong absorptions below 5000 cm^{-1} due to water vapor and CO_2 as in the spectrometer. [69]

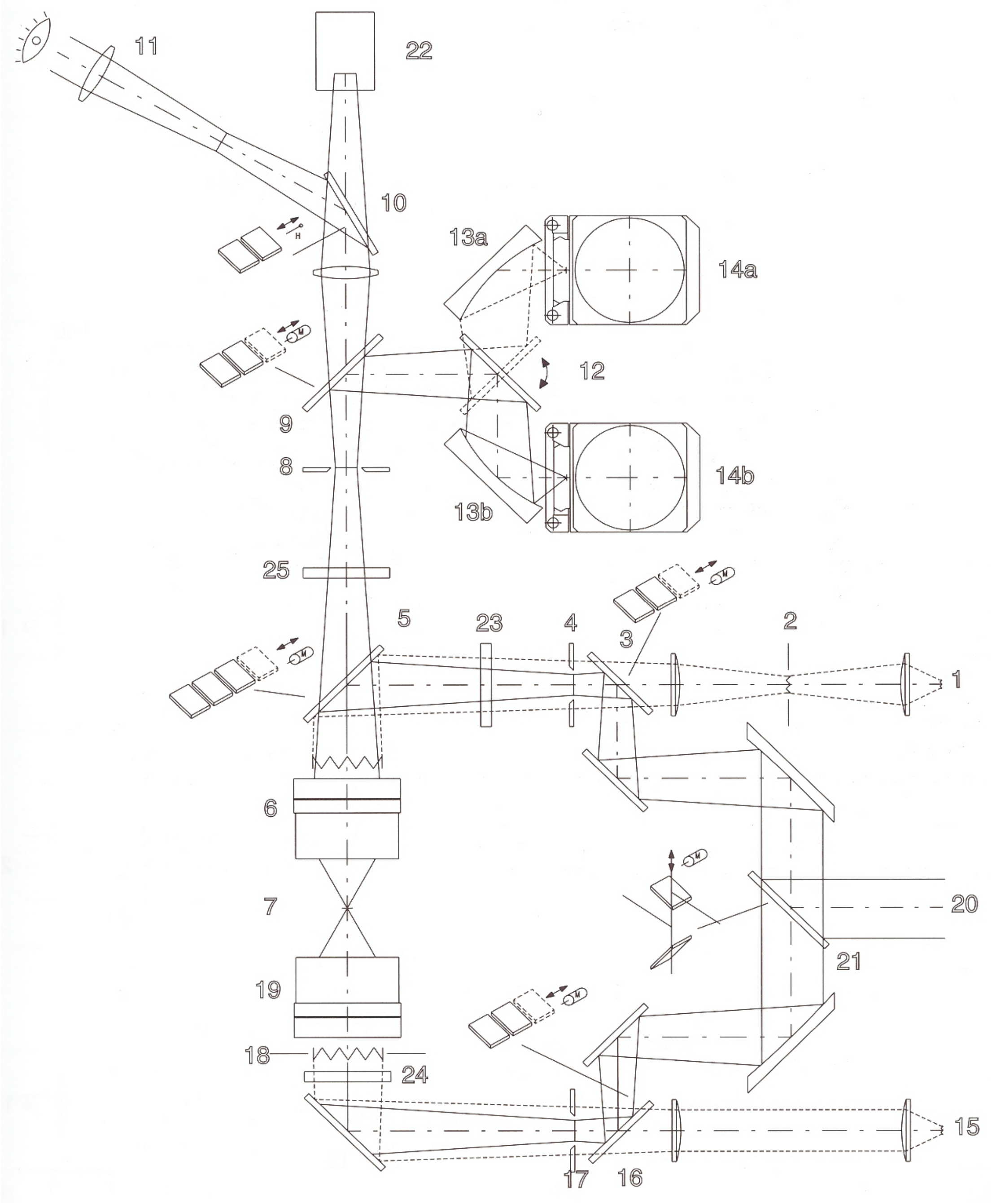

Figure 3.5: Optical path of the IR microscope. [69]

Optical properties of solids:

Introduction:

There are three phenomena, into which the optical properties of solids can be classified (see Fig. 3.6): [70]

Number	**Component and description**
1	Visible light source (reflectance mode).
2	Hoehler aperture: to control the visible light intensity and the contrast in the optional reflectance mode.
3	Three-position motorized changer. 1- Only visible light can pass. 2- Only IR radiation can pass. 3- Both visible light and IR radiation can pass. A special beam splitter is required.
4	Aperture: to define the size of the illuminated area in reflectance mode.
5	Four-position motorized changer. 1- Transmittance mode (open). 2- Reflectance mode (glass beam splitter), for visible light. 3- Reflectance mode (50 percent of the opening area are covered by a mirror), in the IR region. 4- Simultaneous viewing and spectral data acquisition. The IR radiation is directed to the detector, while the visible light is routed to the binocular eyepiece or the camera port.
6	Objective (15x IR and 4x visual objective - standard).
7	Sample.
8	Aperture (normal or automatic knife edge aperture): to define the sample area for the analysis (transmittance or reflectance mode).
9	Three-position motorized changer. 1- Viewing only - an opening allows visible light to reach the binocular eyepiece or the camera port. 2- Spectral data acquisition - IR is routed only to the detector using a mirror. 3- Simultaneous viewing and spectral data acquisition (optional). The IR radiation is directed to the detector, while the visible light is routed to the binocular eyepiece or the camera port.
10	Two-position manual changer. 1- All light goes to the binocular eyepiece (11). 2- All light goes to the camera port (22).
11	Binocular eyepiece: to view the sample.
12	Two-position detector selection mirror: routes IR radiation to detector 1 (14a) or optional detector 2 (14b).
13a	Mirror: routes IR radiation to detector 1 (14a).
13b	Mirror: routes IR radiation to detector 2 (14b).
14a	Infrared detector.
14b	IR detector or FPA detector (optional).
15	Visible light source for transmittance mode.

Table 3.2: The description of the optical elements, illustrated in Fig. 3.5. [69]

Number	Component and description
16	Three-position motorized changer. 1- Only visible light can pass. 2- Only IR radiation can pass. 3- Both visible light and IR radiation can pass. A beam splitter is required.
17	Field aperture (see component no. 8).
18	Aperture for transmittance mode: to define the numerical aperture of the illumination (see component no. 2, but transmittance mode).
19	Condenser (adjustable in beam direction): to maximize the light intensity on the sample in transmittance mode.
20	IR beam from the spectrometer.
21	Three-position motorized changer: 1- Mirror deflects the IR beam to the transmittance optics. 2- Mirror deflects the IR beam to the reflectance optics. 3- No mirror intercepts the IR beam. The beam can go to the external accessory port.
22	Camera port.
23	Optional polarizer (for reflectance mode).
24	Optional polarizer (for transmittance mode).
25	Optional analyzer.

Table 3.3: The description of the optical elements, illustrated in Fig. 3.5. [69]

1. Reflection.
2. Propagation.
3. Transmission.

Fig. 3.6 shows how a light beam interacts with an optical medium. The front surface of the medium reflects back some of the incident light, while the rest enters the medium and propagates through it. If some light reaches the back surface of the medium, then the back surface will act the same as the front surface but the transmitted light in this case will be transmitted through to the other side. So the amount of the transmitted light to the other side of the medium depends on following parameters: [70]

- The reflectivities of the front and back surfaces.
- The way the light propagates through the medium.

Three phenomena take place, when the light propagates through an optical medium:

1. Refraction. [70]

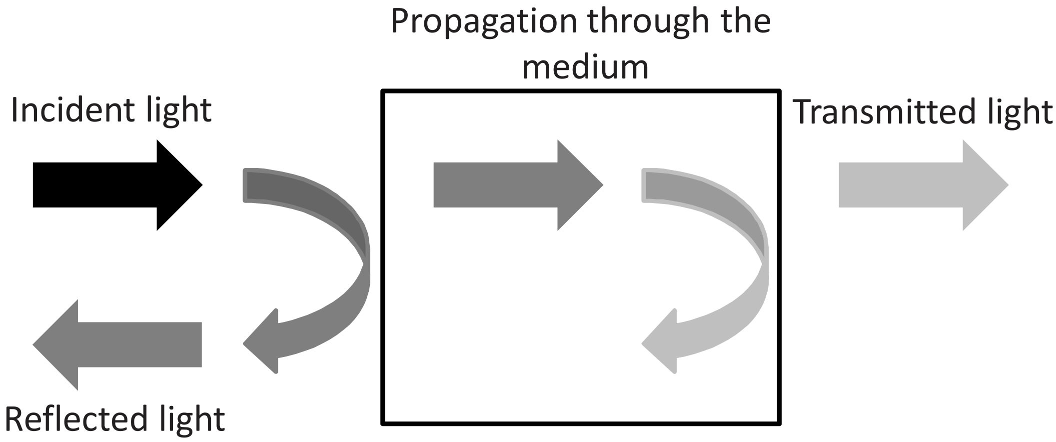

Figure 3.6: Reflection, propagation, and transmission of a light beam incident on an optical medium. [70]

2. Luminescence. [70]
3. Scattering. [70]
4. Absorption, which occurs when the frequency of the propagating light resonates with the transition frequencies of the medium atoms. Only unabsorbed light is transmitted through the medium to the other side, so the transmission of the medium depends on the medium absorption. Selective absorption is held responsible for the colors of many optical materials; rubies are red for example because they do absorb the blue and green light, so the red light is transmitted through the material. [70]

The absorption of light is determined by its absorption coefficient α. The absorption coefficient is the amount of the power, absorbed in a unit length of the medium. [70] If the light is traveling in z direction through the medium and the light intensity (power per unit area) at z is I(z), then the decrease in intensity along dz is given by Eq. 3.5: [70]

$$dI = -\alpha dz \cdot I(z) \tag{3.5}$$

By integrating Eq. 3.5, one can get Beer's law (Eq. 3.6): [70]

$$I(z) = I_0 e^{-\alpha z} \tag{3.6}$$

where I_0 is the optical intensity at z = 0. The absorption coefficient depends strongly on the light frequency. [70]

As mentioned above, the transmission of the medium is dependent on the medium absorption and thus on the absorption coefficient. Also the transmission depends on the reflectivities of the front and back surfaces of the medium. So the transmission T of any optical medium can be obtained by Eq. 3.7: [70]

$$T = (1 - R_1)e^{-\alpha l}(1 - R_2) \tag{3.7}$$

where R_1 and R_2 are the reflectivities of the front and back surfaces, respectively. And l is the thickness of the medium. The first and third terms on the right hand side of Eq. 3.7 give the transmissions of the front and back surfaces, respectively. The middle term in the equation accounts for the exponential decrease in intensity according to Beer's law. If the front and back surfaces have the same reflectivity R, then Eq. 3.7 is simplified to Eq. 3.8: [70]

$$T = (1 - R)^2 e^{-\alpha l} \tag{3.8}$$

Optical materials:

The materials are classified into five general categories: [70]

1. Crystalline insulators and semiconductors.
2. Glasses.
3. Metals.
4. Molecular materials.
5. Doped glasses and insulators.

I would just focus on the main optical properties of only two categories (crystalline insulators and semiconductors and metals) because our studied materials experience a metal-semiconductor phase transition. [70]

Crystalline insulators and semiconductors:

Fig. 3.7(a) shows the transmission spectrum of crystalline sapphire (Al_2O_3) from the infrared to the ultraviolet spectral range. [70]

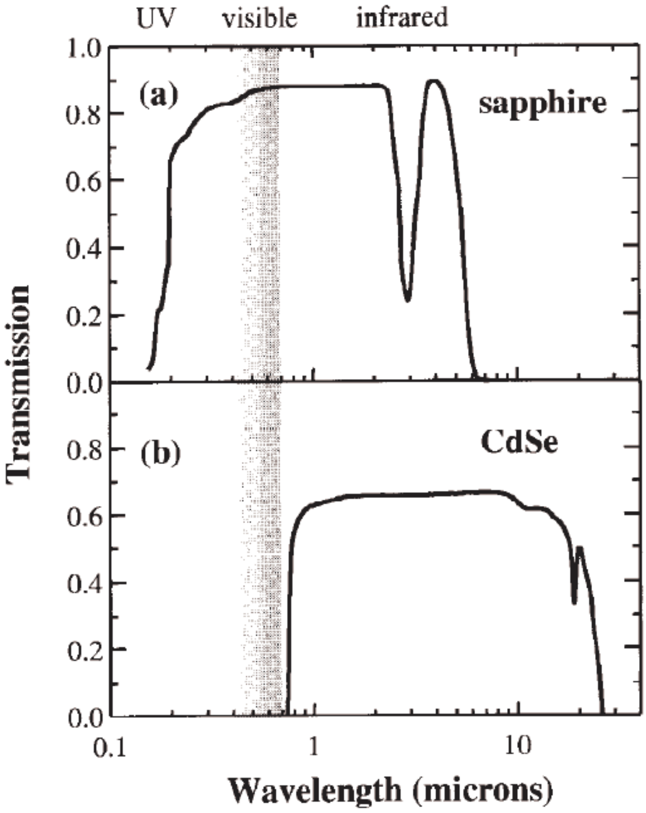

Figure 3.7: (a) Transmission spectrum of a sapphire crystal of thickness 3 mm. (b) Transmission spectrum of a CdSe crystal of thickness 1.67 mm. [70]

This spectrum shows the main features, observed in all insulators. The principle features are summarized, as follows: [70]

1. In the wavelength range (0.2 - 6) μm, the transmission is high.
2. In the infrared spectral range around 3 μm, there is a dip in the transmission. Also the transmission dropes sharply for $\lambda > 6$ μm. They are caused by the lattice absorption (phonons).
3. There is a sharp drop in the transmission in the ultraviolet spectral range for $\lambda < 0.2$ μm. This is due to the absorption by bound electrons (interband transitions). The onset of this absorption is called the fundamental absorption edge. The frequency of this edge is determined by the energy band gap.

The optical properties of semiconductors and insulators are similar except that the electronic and vibrational transitions happen at longer wavelengths, as shown in Fig. 3.7(b). [70]

Metals:

Fig. 3.8 shows the reflectivity of silver from the infrared to the ultraviolet spectral range.

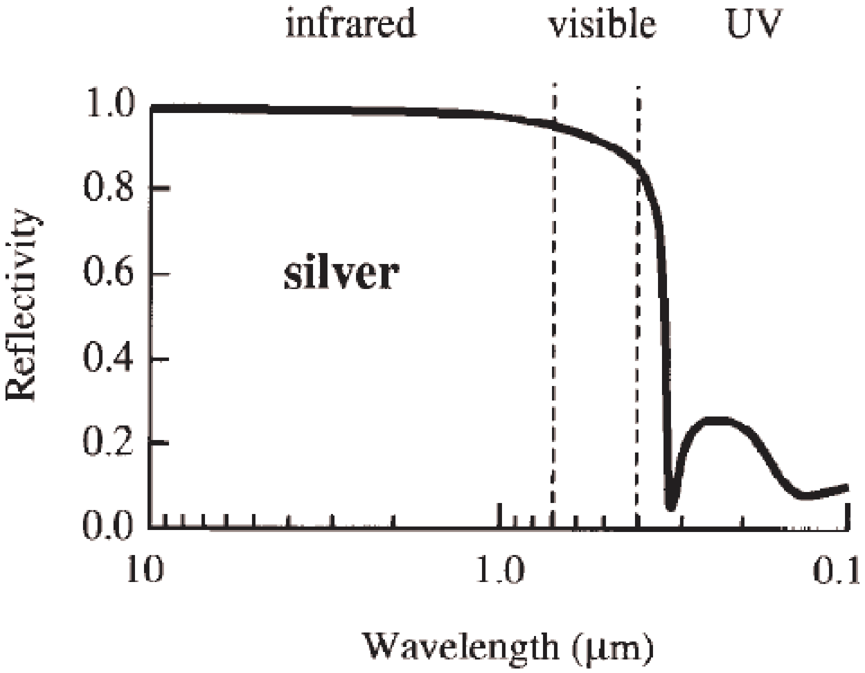

Figure 3.8: Reflectivity of silver from the infrared to the ultraviolet spectral range. [70]

The principle features are summarized, as follows: [70]

- The reflectivity is close to 100 percents in the infrared spectral range.
- The reflectivity remains above 80 percents in the visible spectral range.
- The reflectivity drops sharply in the ultraviolet spectral range.

There is a cut-off frequency (plasma frequency), below which the reflectivity is very high. So the plasma frequency of silver is in the ultraviolet spectral range (see Fig. 3.8). Thus silver reflects infrared and visible frequencies, but transmit ultraviolet frequencies. [70]

3.1.2 Infrared spectroscopy at low temperatures

In order to perform low-temperature optical infrared measurements on the blue bronzes, a Cryovac liquid helium cryostat coupled to the FTIR spectrometer has been used because of the following reasons:

- The reflectivity of the blue bronze is too high along the chain direction. We therefore need a proper reference. The best technique to get a very good reference is the evaporation of gold on top of the sample surface. [71] This can be done in situ using this cryostat.
- The samples are big, so there has been no need to use a microscopic cryostat.
- The samples are irregular in shape with cleavage steps on the surface. We therefore need to evaporate gold on top of the sample surface to compensate for the rough surface.

Getting a very good reference by the evaporation of gold on top of the sample surface has been accomplished by using a Cryovac liquid helium cryostat, where a gold evaporator can be connected to it and the gold evaporation can be done in situ. To understand this technique much better, I would like to divide this section into several sections starting from the free standing reflectivity measurements and then going through the details of this technique.

(1) Free-standing optical IR measurements:

These measurements are being performed using the IR microscope coupled to the FTIR spectrometer, shown in Fig. 3.4. At the focal point between the two objectives (see Fig. 3.5) there is a remotely controlled stage, on which the sample is sitting as shown in Fig. 3.9.

The sample and the reference mirror (usually silver mirror) are sitting on a remotely controlled moving stage. They must be at the focal point between the two objectives and aligned with respect to each other as shown in Fig. 3.9, i.e, they should not be tilted with respect to each other. The radiation focused onto the sample are reflected by it and the reflected radiation from the sample are being traveled toward a detected through some optical elements shown in Fig. 3.5. After measuring the intensity reflected from the sample, the stage is moved to the left as shown by the dark arrow in Fig. 3.9. Then the radiation will be focused this time onto the reference mirror, which reflects the radiation toward the same detector. Now the intensities reflected from the sample and the mirror are measured. By dividing the one from the sample by the one

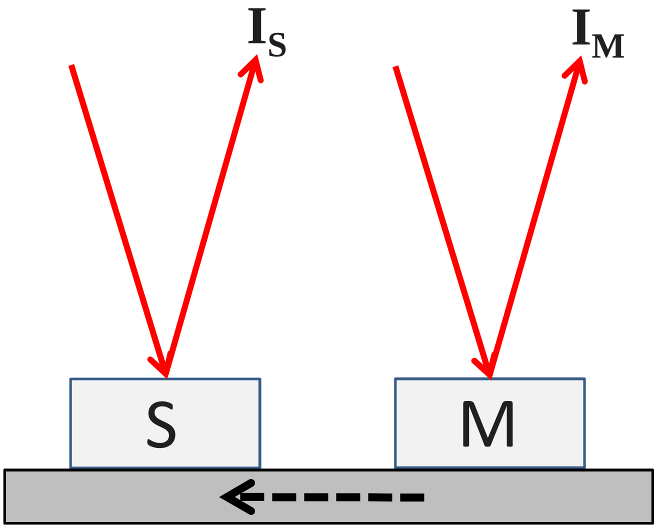

Figure 3.9: Layout of the free-standing technique.

from the mirror, we can get the reflectivity of the sample with respect to the reference mirror.

(2) Cold finger cryostat:

As mentioned above, our studied samples are irregular in shape with cleavage steps on the surfaces. To compensate for the rough surface of the samples in order to get a nice reflectivity spectra of them, the best way is to coat the sample surface with a good metal (typically gold) and use the coated sample as reference in the reflectance measurements. [71]

This can be done using a liquid helium cryostat, as mentioned above. We use two openings in the top of the cryostat. One opening is used to transfer the liquid helium from the helium can to the heat exchanger of the cryostat, using a stainless steel transfer tube. While we connect a pump to the other opening. When the pump is on, the liquid helium starts to flow through the cryostat to cool it down. In the path between the pump and the corresponding opening, there is a magnetic proportional valve. The opening of the magnetic proportional valve is controlled by a temperature controller. So the magnetic proportional valve together with a manual needle valve in the transfer line, the liquid helium flow rate is controlled. Also there is a heater, mounted close to the sample holder. The sample holder is attached to the heat exchanger. The heater is also controlled by the temperature controller, mentioned above. So using the heater, the magnetic proportional valve, and the needle valve with the help of the temperature controller, the required temperature can be achieved. The temperature range of the cryostat is (500 - 5) K. I would also mention in this text that there are two sensors (one is mounted next to the sample and the other one is mounted in the top of the cryostat next to the liquid helium path). The temperature controller is connected to them using an electrical feedthrough in the top of the cryostat. The reading of these two sensors are displayed by the temperature controller, so that one can know the temperature. Also the temperature controller uses the readings of the sensors for stabilizing the required temperature. [72] The cryostat arrangement is illustrated in Fig. 3.10, while the cold finger cryostat is illustrated in Fig. 3.11.

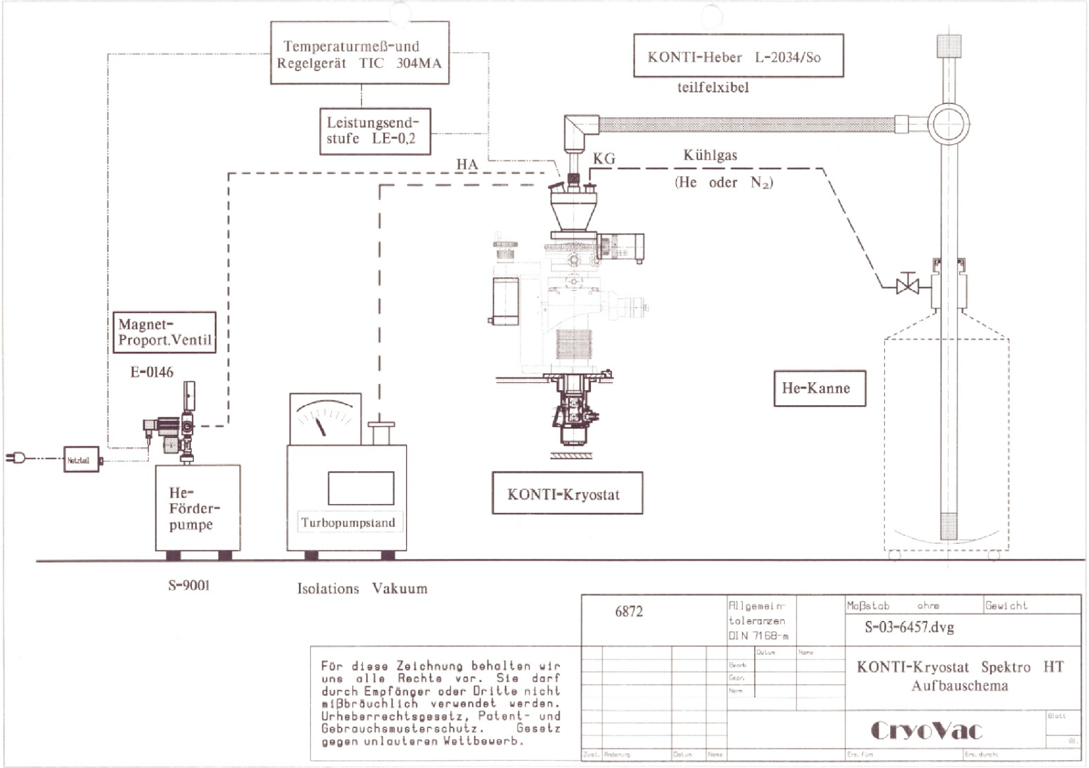

Figure 3.10: Schematic illustration of the arrangement of the cold finger cryostat and the corresponding equipment. [72]

The optical tail of the cryostat has four access ports on its sides to enable the following activities: [72]

- Two optical accesses for transmission measurements.
- Optical access for reflection measurements (see Fig. 3.11).

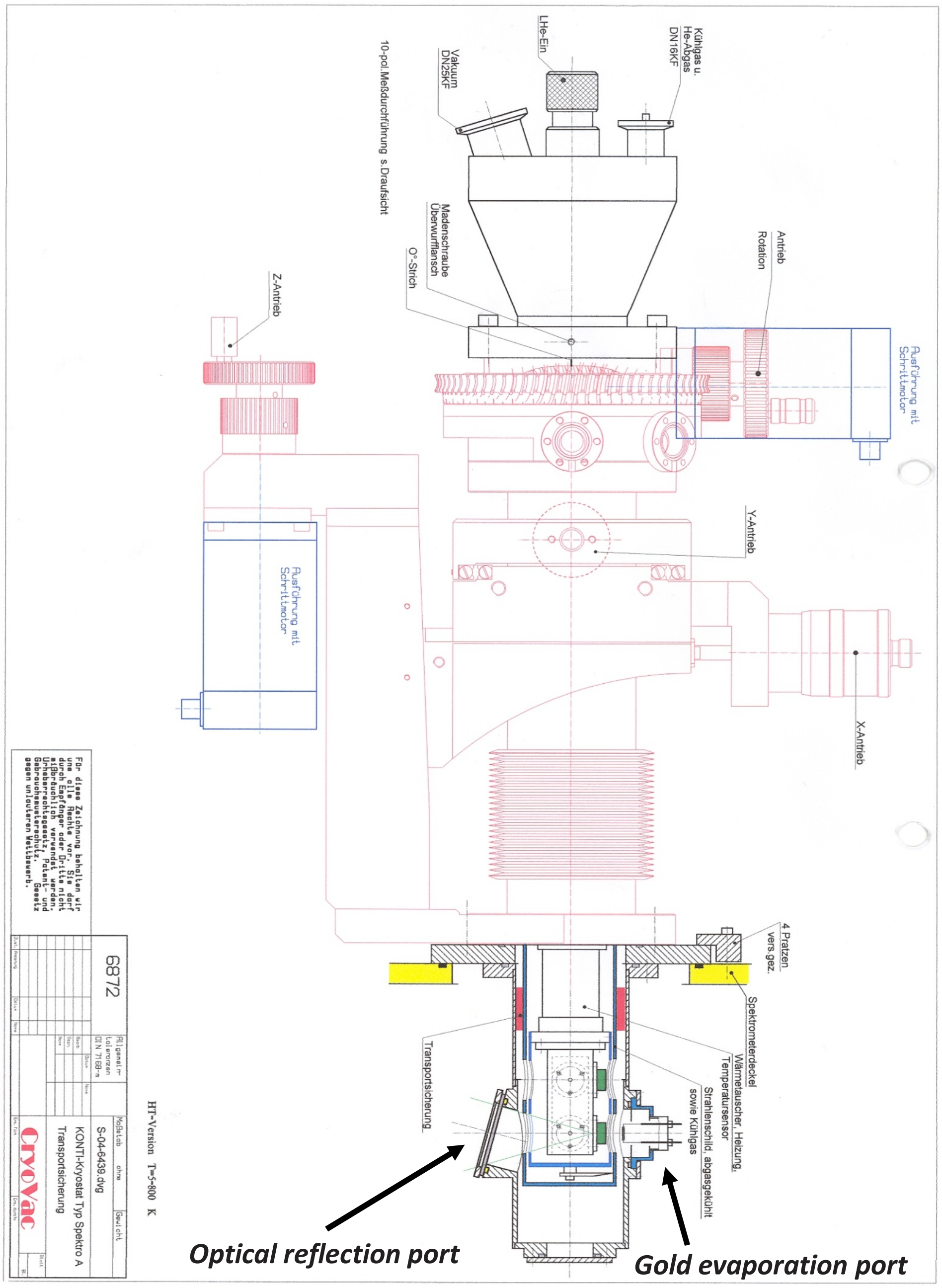

Figure 3.11: Sketch of the cold finger cryostat. [72]

- Gold evaporation access (see Fig. 3.11).

The top view of the optical tail is illustrated in Fig. 3.12. The parts are numbered and the corresponding descriptions of theses numbers are shown below:

1. The sample holder, on which the sample and the side mirror are mounted.

2. The outer box, which has the four access ports.
3. Port for the optical reflection access.
4. Port for the gold evaporation access.
5. Port for the optical transmission access.
6. Another port for the optical transmission access.

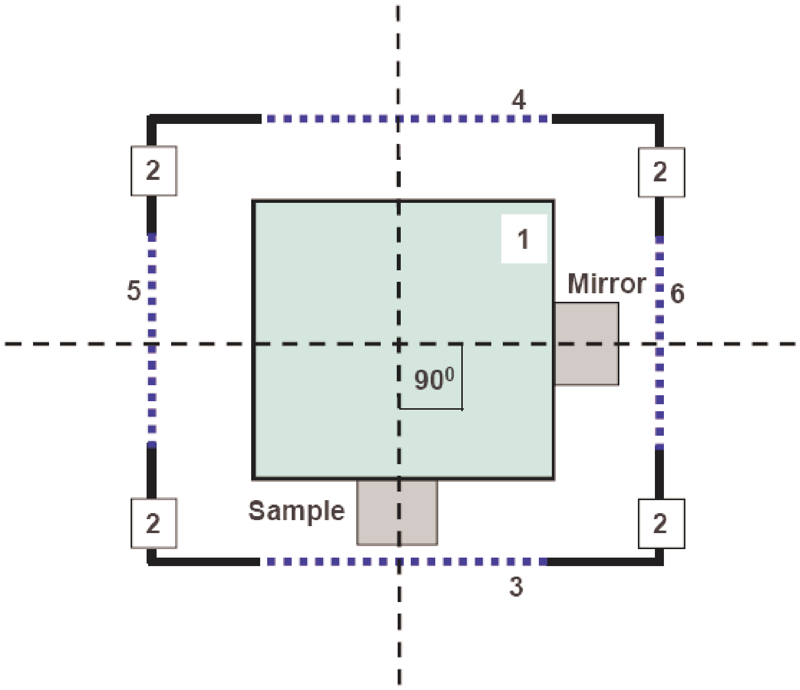

Figure 3.12: Sketch of the optical tail top view of the cold finger cryostat.

The volume between parts 1 and 2 is connected to another pump in order to evacuate it down to 10^{-7} mbar. A good vacuum is required to achieve a good quality gold film on top of the sample surface and to eliminate contamination of the spectra by outgassing, water vapor, and CO_2. The access ports should be blocked while pumping down either using blind flanges or optical windows, depending on the mode of the optical measurements to be performed. Also the types of the optical windows used depend on the spectral frequency range. [72]

In the reflection mode, the beam must pass through the optical reflection access to reach the sample. The corresponding optical window is angled to avoid window reflections, being along the optical beam path. While ports 5 and 6 must be blocked using blind flanges in the reflection mode. One can see in Fig. 3.11 how the optical reflection port is angled.

Actually the sample (the side mirror as well) is attached to the tip of a cone using some epoxy as shown in Fig. 3.13, which shows the sample mounting arrangement. Because of the geometry of the holder, it has the following advantages: [71]

- light which hits the sample is reflected back, while light which misses the sample is scattered out of the optical beam path.
- So, the entire sample area can be measured using a large spot (larger than the sample size). By using a large spot, we can still hit the entire sample area even if the optical tail of the cryostat does shift while cooling down.

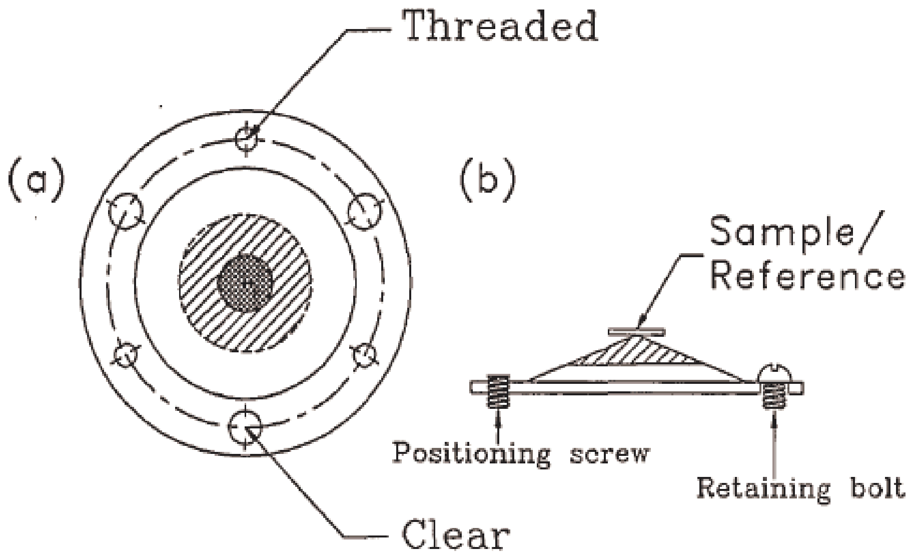

Figure 3.13: Sample mounting arrangement: (a) The top view, showing the location of the mounting screws. The hatched lines indicate the usual size of the aperture on the cone, and the crosshatched area is the size of the sample. (b) The side view, showing the sample. The angle on the cones is typically $\geq 20°$. [71]

(3) How to attach the cold finger cryostat to the FTIR spectrometer:

In Fig. 3.4 one can see the sample compartment, where the IR beam is being focused. It is possible to insert the cold finger cryostat into this compartment, in order to perform the low-temperature reflectivity/transmission measurements on the blue bronzes. As shown in Fig. 3.4 the cold finger cryostat is inserted and a sample is placed at the focal point in a way, in which transmission measurements on the sample can be done. To perform reflectivity measurements, the sample will be no longer facing the focused beam because the sample will be placed in a different way as shown in Fig. 3.12. In this case, we have had to refocus the IR beam in a way in order to hit the sample at near-normal incidence. This has been achieved only by designing and building a reflection unit to perform this task.

Reflection unit:

Fig. 3.14 shows the top view of the sample compartment of the FTIR spectrometer, the inserted cold finger cryostat in the reflection mode, and the reflection unit. The parts in the figure are numbered and tabulated in Table 3.4. Please notice that Fig. 3.12 is the blow up of part no.9.

Item	**Description**
1	Right big plane mirror of the reflection unit
2	Right small plane mirror of the reflection unit
3	1 mm aperture
4	Right spherical mirror of the reflection unit
5	Sample
6	Left spherical mirror of the reflection unit
7	Left small plane mirror
8	Left big plane mirror of the reflection unit
9	The top view of the optical tail of the cold finger cryostat
10	Rectangular metal plate for holding the plane mirrors
11	The borders of the sample compartment of the FTIR spectrometer
12	The holder of the spherical mirrors

Table 3.4: The description of Fig. 3.14 parts.

As mentioned above, the IR beam coming from the interferometer is being focused in the sample compartment as shown in Fig. 3.14 (the yellow beam). When the cold finger cryostat is inserted in the reflection mode, then the sample will be no longer facing the focused IR beam as shown in the figure. We need to reflect and refocus the IR beam in a way, in order to hit the sample at near-normal incidence (blue dot in Fig. 3.14). This can be done only by designing and building a reflection unit shown in Fig. 3.14 to perform this task. I would bring your attention to an important issue about the aperture (part no.3):

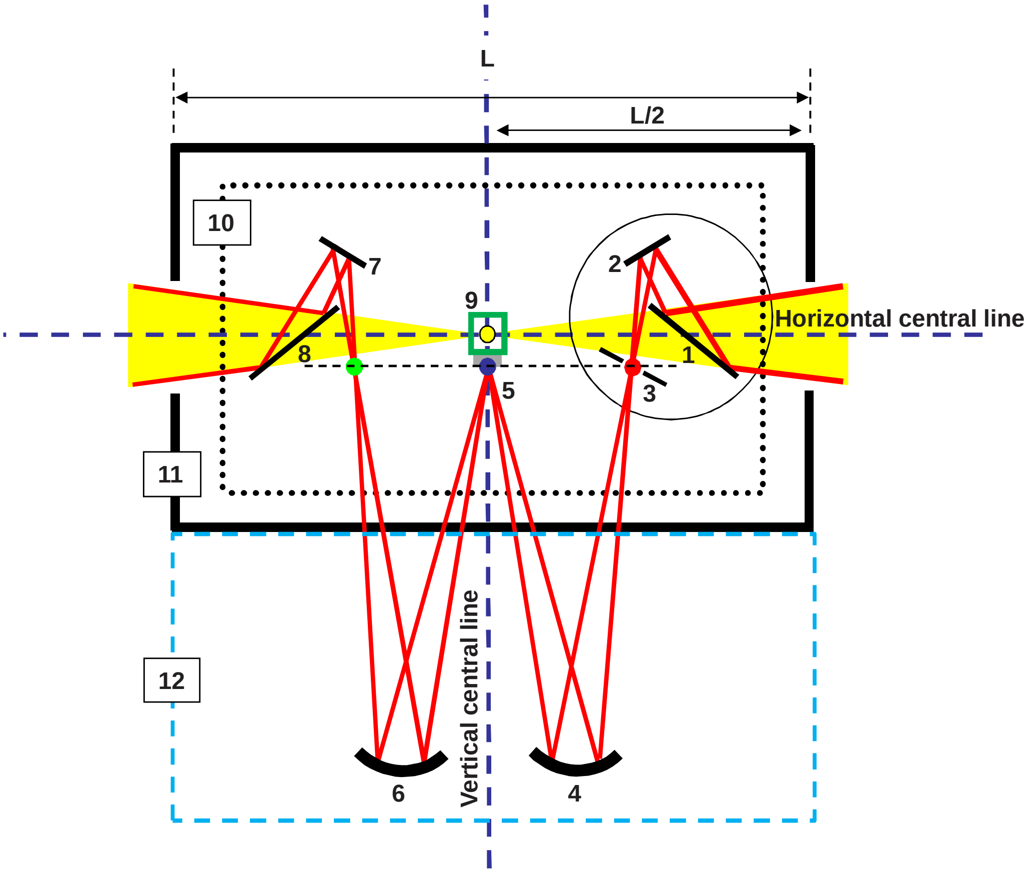

Figure 3.14: Schematic illustration, explaining the working principle of the reflection unit.

The aperture is placed at the focal point (red dot in Fig. 3.14) in order to get rid of instabilities, coming from the interferometer and other optical elements which reflect and focus the IR beam many times before hitting the sample. The actual size of the used aperture has been always 1 mm, which is smaller than the area of the sample surface. The aperture size can be larger than the area of the sample surface, because of the geometry of the sample holder shown in Fig. 3.13.

How does the reflection unit work?

The goal is to make the beam hit the sample at near-normal incidence. To do that, we have had to use two plane mirrors and one spherical mirror in the right part of the sample compartment (parts 1, 2, and 4 in Fig. 3.14), which reflect the IR beam coming from the interferometer and focus it onto the sample (blue dot in Fig. 3.14).

And exactly the same stuff in the left part of the sample compartment (parts 6, 7, and 8 in Fig. 3.14), which reflect the reflected beam from the sample and deflect it finally toward the detector. The procedure of the low-temperature reflectivity measurements is the following:

1. When the IR beam hits the sample (blue dot in Fig. 3.14), we measure the intensity reflected from the sample at room temperature (I_S).
2. Then we rotate part no.9 (see Fig. 3.14) by 90° CW, in order to make the IR beam hit the side silver mirror (see Fig. 3.12). Then we measure the intensity reflected from the side silver mirror at room temperature (I_{Ag1}).
3. Then we cool down to a low temperature (T_1). Then we measure the intensity reflected from the side silver mirror at T_1.
4. Then we rotate part no.9 by 90° CCW to make the IR beam hit the sample. Then we measure the intensity reflected from the sample at T_1.
5. We cool down to a lower temperature (T_2). Then we measure the intensities reflected from the sample and side silver mirror at T_2, starting with the sample.
6. After we finish the temperature cycle, we warm up to 300 K. The IR beam is hitting the sample at this point.
7. Then we rotate part no.9 by 180° CW, in order to make the sample face the gold evaporation port. Then we evaporate gold on top of the sample surface.
8. Then we rotate part no.9 by 180° CCW to make the IR beam hit the sample. Then we measure the intensity reflected by the gold layer on top of the sample surface at room temperature (I_{Au}).
9. Then we rotate part no.9 by 90° CW to make the IR beam hit the side silver mirror. Then we measure the intensity reflected by the side silver mirror again at room temperature I_{Ag2}.
10. Then we cool down to T_1 again. Then we measure the intensity reflected from the side silver mirror at T_1 again.
11. Then we rotate part no.9 by 90° CCW to make the IR beam hit the sample. Then we measure the intensity reflected from the gold layer at T_1.
12. Then we cool down to T_2 again. Then we measure the intensities reflected from the gold layer and side silver mirror at T_2, starting with the gold layer.

13. After we finish the temperature cycle, we warm up to 300 K.
14. By dividing (I_S/I_{Ag1}) by (I_{Au}/I_{Ag2}), we will get the reflectivity of the sample with respect to the gold layer which is on top of the sample surface (I_S/I_{Au}). Please notice that $I_{Ag1} \cong I_{Ag2}$. By doing that at all temperature, we will have the following advantages:
    - While rotating part no.9 CW and CCW by 90° to switch between the sample and side silver mirror at each temperature after and before the gold evaporation, the motor could cause some offset. The offset means that the sample and side silver mirror are tilted with respect to each other. The effect of this offset on the reflectivity spectra is removed by having I_S/I_{Au}.
    - The gold layer should not be too thick, so that it does not have the same roughness of the sample surface. In the same time, the thickness of the gold layer should be more than the skin depth of gold in the measured frequency range. Anyway, the proper gold thickness has been achieved. So, by having I_S/I_{Au} the effect of the sample roughness on the reflectivity spectra will be divided out. I would mention here that the sample and side silver mirror have been always kept under vacuum (10^{-6} mbar) inside the cryostat. Also the reflection unit together with the FTIR spectrometer have been always kept under vacuum (3 mbar). This is to avoid contamination and oxidation during the gold film growth and also to avoid strong artificial features in the reflectivity spectra below 5000 cm^{-1} due to water vapor and CO_2.
    - Also as mentioned before, the reflectivity of the blue bronze is too high along the chain direction. We therefore need a proper reference. The best technique to get a very good reference is the evaporation of gold on top of the sample surface.

The whole setup is shown in Fig. 3.15 (by taking a look at Fig. 3.14, one can understand Fig. 3.15 much better).

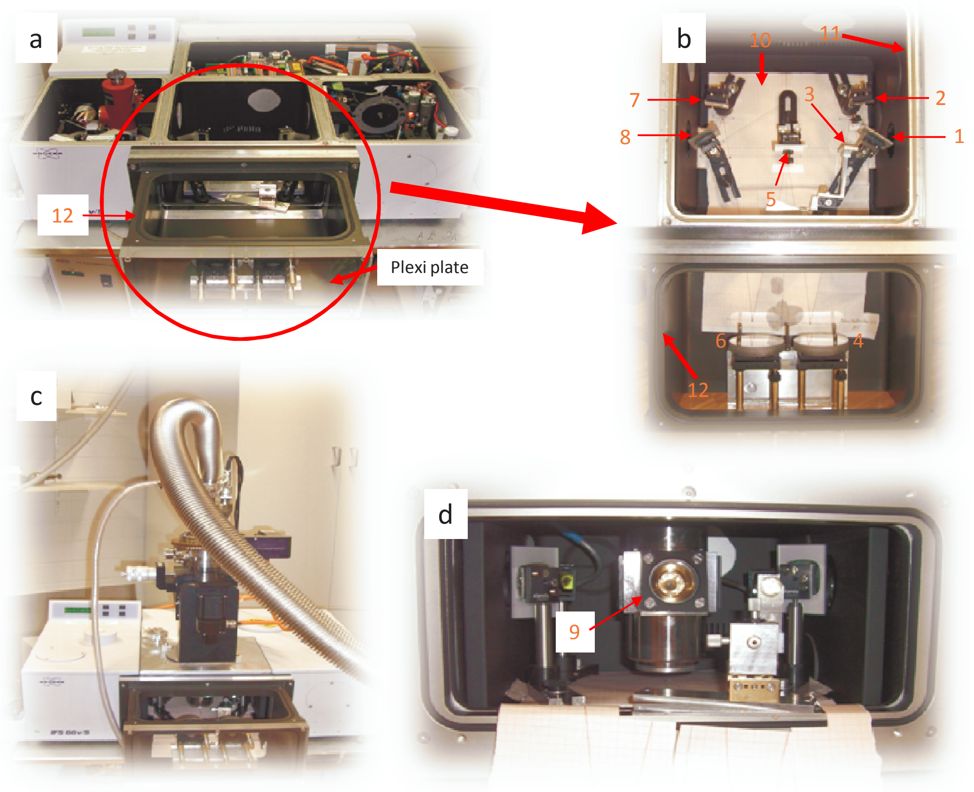

Figure 3.15: (a) The reflection unit mounted into the FTIR spectrometer. (b) The top view of the reflection unit. (c) The cold finger cryostat, inserted into the FTIR spectrometer. (d) The black box is unmounted to show the optical window and the sample inside the cold finger cryostat, which substitutes the free standing mirror shown in b.

3.2 Evaporation unit

Designing and building this system has been done to perform the low temperature dc transport measurements on our studied samples, because in contact regions indium films (150) covered by gold films of the same thickness had been crucial to achieve stable contacting at low temperature.

Introduction:

Thin film deposition technology is very important because of many applications. It can be used in optics, microprocessors, biotechnology, and in the tool manufacturing industry. [73] In our setup, a thermal evaporation technique has been used, which is one kind of the thin film deposition techniques. More or less all thin film deposition techniques use vacuum to eliminate contamination during the growth of the film. In our setup, a good vacuum (10^{-7} mbar) has been achieved.

Evaporation system:

The schematic layout of the system is shown in Fig. 3.16 and the parts shown in the figure are described in Table 3.5. The apparatus consists of a glass cylindrical vacuum bell jar (Part no.16) and an ultra high vacuum pump (Part no.5) which has a pressure gauge. The glass chamber is always covered by a metal cylindrical guard (Part no.17) to protect it form being damaged. The evaporating source is mounted within the glass chamber. The source consists of a thermal boat (Part no.13), connected to two copper electrodes (Part no.12) which themselves are connected to a current source (Part no.6). One has to put a small amount of the material (Part no.3), which one wants to evaporate in the thermal boat. This amount becomes very hot when the current source is turned on. The material to be evaporated should have a boiling point less than the melting point of the thermal boat. In this case the material will boil and start to evaporate before the thermal boat begins to melt. The pressure inside the chamber reaches 10^{-7} mbar, which is very good to reduce contamination during the growth of the film. Finally condensing on any cold surface forms a film. The rate of deposition (Å/Sec.) can be controlled by controlling the applied current. And by controlling time with respect to the deposition rate, the required thickness can be achieved.

Crystal monitor:

A quartz crystal (Part no.15) is mounted inside the vacuum chamber. The sample is mounted just close to it and at the same hight (see Part no. 1). The crystal oscillates at 5 to 6.1 MHz. When a material is being evaporated, the vapor does coat the sample and the crystal simultaneously. This makes the crystal oscillate slower and the frequency change versus time gives the achieved thickness of the coated material on the sample. The crystal has a life time, so it needs to be replaced every now and then. [74]

Cooling system:

The temperature inside the vacuum chamber increases while evaporating, so the crystal must be being cooled during the evaporation process by a closed cycle of pure water

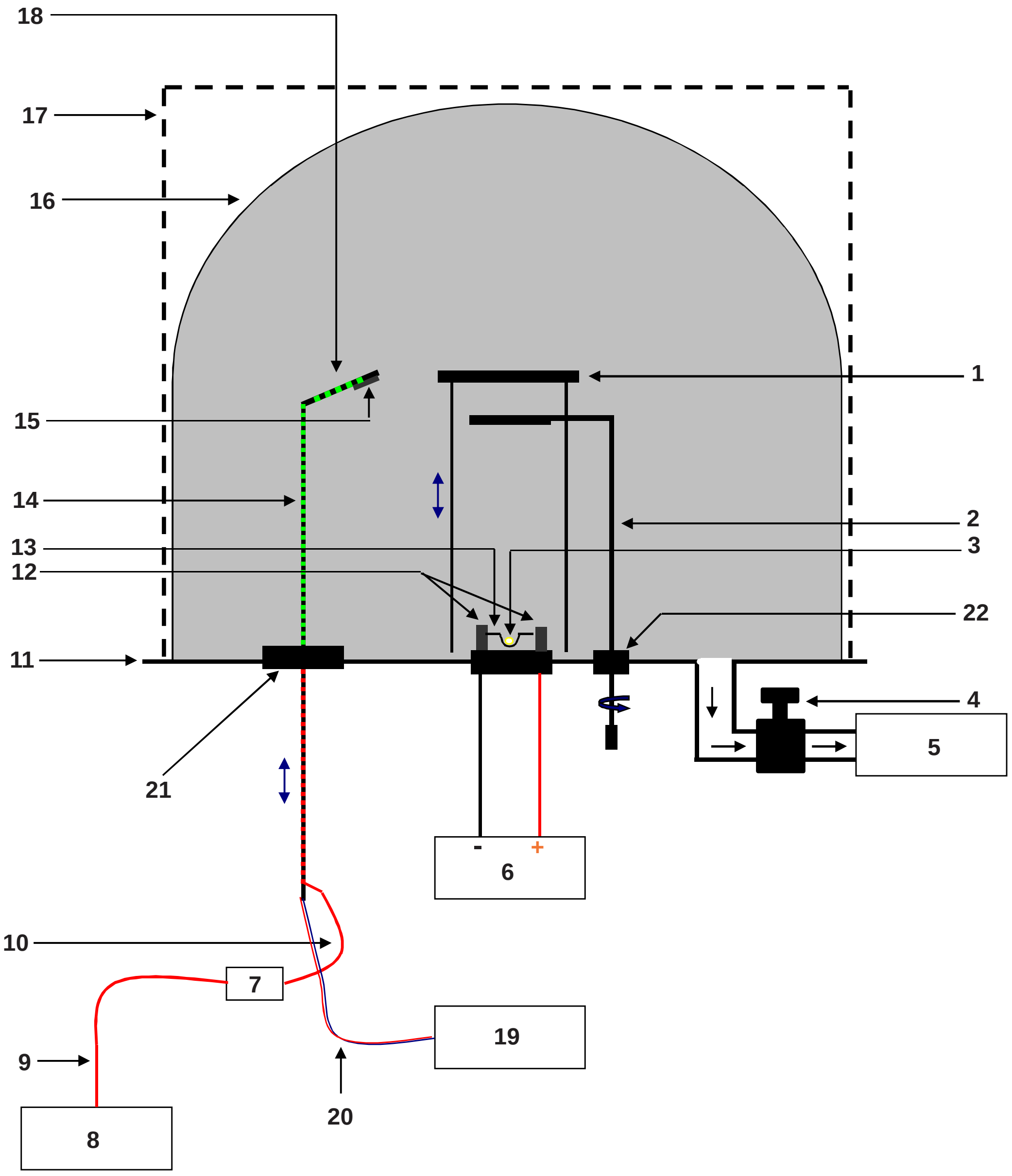

Figure 3.16: The schematic diagram of the evaporation chamber.

in order to avoid heating up the crystal (parts no.19 and no.20). The whole setup is shown in Fig. 3.17 (by taking a look at Fig. 3.16, one can see Fig. 3.17 much better).

Part number	Description
1	Mask holder
2	Mechanical shutter
3	Target
4	Valve
5	Ultra high vacuum pump
6	Current source (60 A)
7	Oscillator
8	Thickness meter
9	BNC cable
10	BNC cable
11	Flange
12	Copper electrodes
13	Thermal boat
14	In vacuum cable
15	Quartz crystal
16	Glass cylindrical vacuum chamber
17	Metal cylindrical guard for the glass chamber
18	Feedthrough
19	Water cooling system
20	Pipes
21	Electrical feedthrough
22	Feedthrough

Table 3.5: The details of Fig. 3.16 parts.

3.3 Sample preparation and the dc setup

Pure blue bronze ($K_{0.3}MoO_3$), Rb-doped blue bronze [$(K_{0.5}Rb_{0.5})_{0.3}MoO_3$], and W-doped blue bronze ($K_{0.3}Mo_{0.99}W_{0.01}O_3$) single crystals have been prepared by various methods, namely by the temperature gradient flux method and electrolytic reduction of the molten salts of A_2CO_3-MoO_3 for pure blue bronze $A_{0.3}MoO_3$ (A= K and Rb), K_2CO_3-Rb_2CO_3-MoO_3 for Rb-doped $K_{0.3}MoO_3$, and K_2CO_3-MoO_3-WO_3 for W-doped $K_{0.3}MoO_3$. Different concentrations of the dopants in the melt determine the doping levels in the obtained crystals. For Rb-doped samples, the doping ratio is almost the same as that in the melt, but for the W-doped compounds, the doping ratio is nearly 2 to 3 times bigger than that in the melt. [75] In our dc electrical transport measurements a standard four-probe configuration has been used. Since the samples are highly anisotropic, so Laue diffraction has been used to determine the orientations of the prepared samples (b axes). In the contact regions, indium films (150 Å thickness)

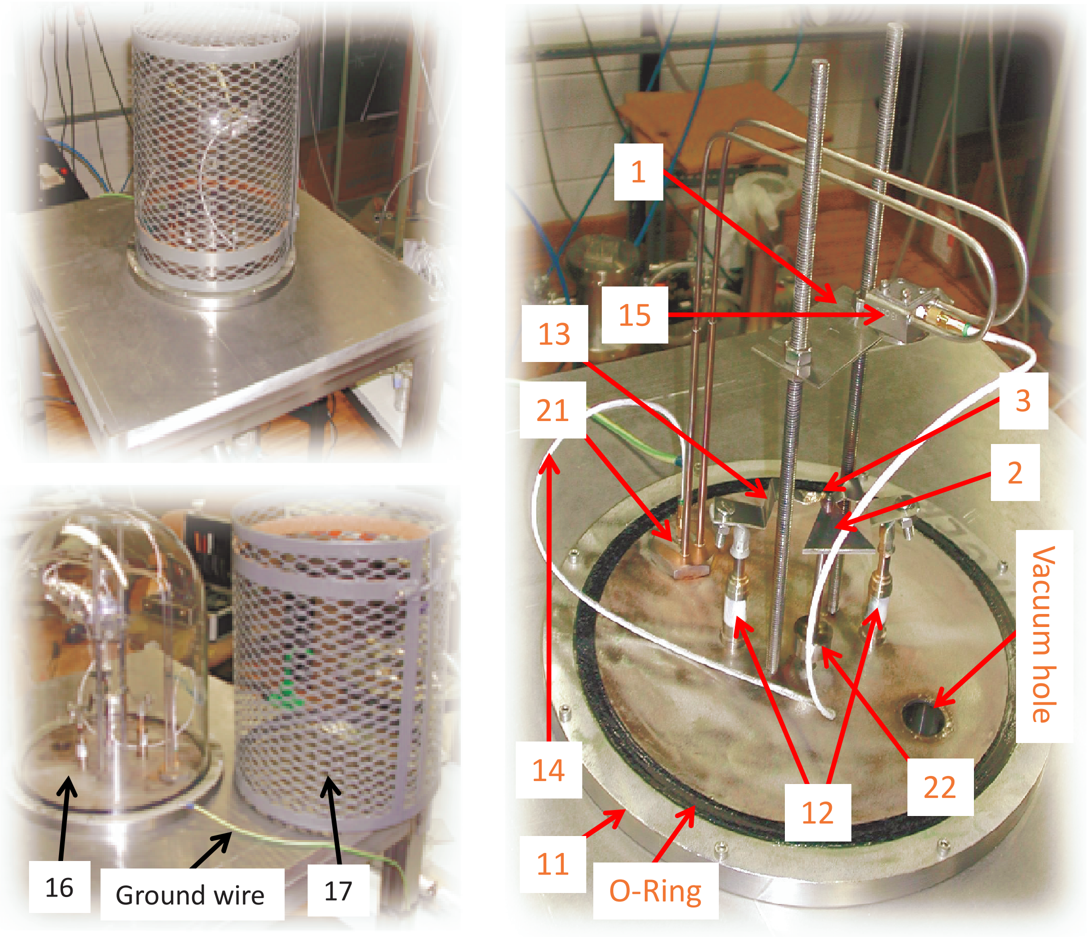

Figure 3.17: The evaporation chamber.

have been covered by gold films (also 150 Å thickness) to achieve a stable contacting at low temperatures. Proper masks have been built (using a manually controlled high accurate movable desk saw) which have allowed us to evaporate gold and indium only on the contact regions, as shown in Fig. 3.18(a). All dc transport measurements have been done along the chain direction. That means that the gold and indium layers on the contact regions, illustrated in Fig. 3.18(b) have been exactly perpendicular to the chain axis. To make that, we have checked the orientation of all samples as mentioned above before mounting the sample into their corresponding masks. This has been done carefully using the Laue camera. Also the stoichiometry of each sample has been checked carefully using the energy dispersive X-Ray technique. An insulating film of 100 μm thickness (Kapton) has been always glued onto the sample holder using a low temperature glue (ge low temperature varnish glue). Kapton is a polyimide film,

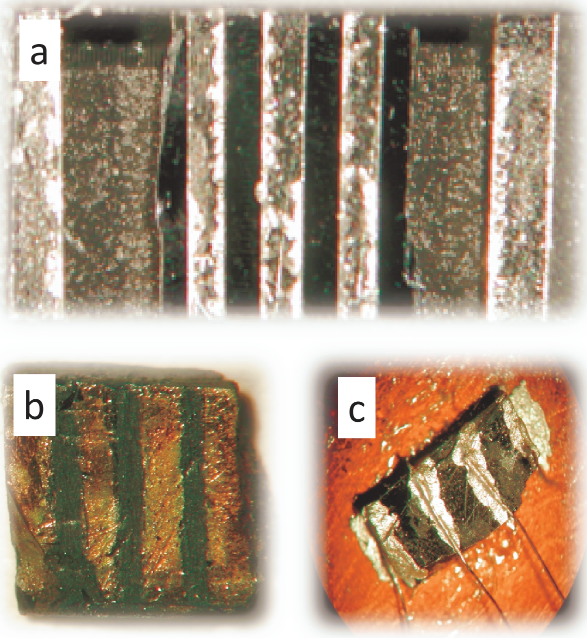

Figure 3.18: (a) The sample under the mask. (b) The sample covered by indium and gold layers at the contact regions. (c) The sample mounted into the sample holder.

which can remain stable in a wide range of temperatures (0 K to 673 K). Kapton isolates the sample from the conducting copper holder electrically, but still its thermal conductivity is sufficient to ensure enough thermal contact between the sample and the sample holder. The sample has been always glued onto the insulating layer using the same glue, mentioned above as shown in Fig. 3.18(c). The ge low temperature varnish glue is also stable at low temperatures and its thermal conductivity is also sufficient to ensure enough thermal contact between the sample and the sample holder. The sample itself is connected to four copper wires (300 μm thickness) using four platinum wires (50 μm thickness and 2 mm length). The platinum wires are soldered to four copper wires from one side and from the other side they are attached to the sample at the contact regions using a silver paste as shown in Fig. 3.18(c). The copper wires are connected to the four-probe dc setup from the other side (see Fig. 3.19). The current has been driven to pass through the sample using the platinum wires which are attached to the sides of the sample from one side and from the other side they are connected to a constant voltage source (Keithley 6517A) (see Figs. 3.18(c) and 3.19). The voltage drop across the sample has been measured using the platinum

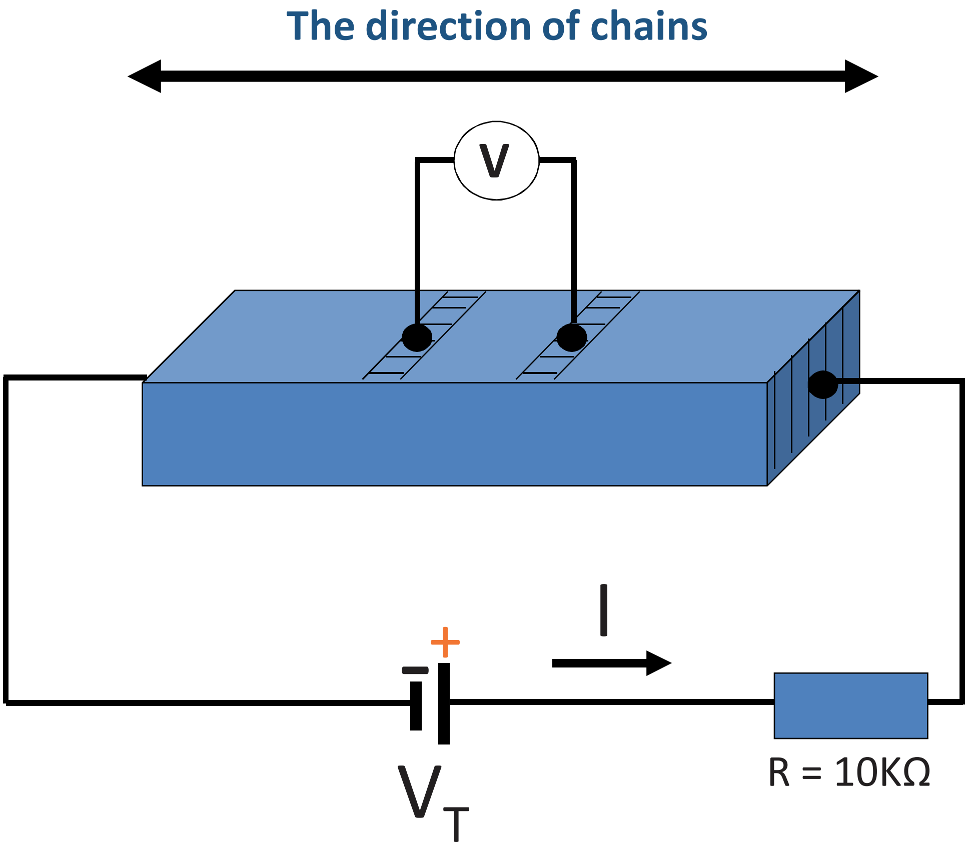

Figure 3.19: The schematic diagram of the dc setup.

wires, which are attached to the contact regions on the sample surface from one side and from the other side they are connected to a nanovoltmeter (Keithley 182) (see Figs. 3.18(c) and 3.19). To get the temperature dependence of the sample resistance R(T), a 10 kΩ resistor has been connected in series (see Fig. 3.19). The expected sample resistance at room temperature is 0.5 Ω, so it is ignorable as compared to the 10 kΩ resistor. Hence by applying 1 V, very low current of 0.1 mA will pass through the sample at room temperature. The goal is to drive a very low current in order to avoid moving the CDW at low temperatures ($T \leq T_P$). R is expected to be much lower than the 10 kΩ resistor at high temperatures ($T > T_P$), so the driven current will be more or less constant at high temperatures ($I \cong 0.1$ mA at $T > T_P$) by applying 1 V. While R is expected to increase with lowering the temperature below T_P because of the metal-to-insulator Peierls transition, so R is expected to be much higher than the 10 kΩ resistor at very low temperatures ($T \ll T_P$). Hence the driven current will not be constant any more, i.e., it will decrease with lowering the temperature as R increases (I $<$ 0.1 mA at T $\leq$ T_P). So the driven current has been also low enough not to slide the CDW at low temperatures (T $\leq$ T_P) by applying 1 V. Also the low driven current in both cases has been achieved in order not to heat up the sample and not to damage the contacts. The next two sections will be about the EDX and Laue diffraction techniques, respectively.

3.3.1 Energy dispersive X-ray spectroscopy

Energy-dispersive X-ray spectroscopy (EDS or EDX) is a technique, used to find out the contents of elements in a specimen. It is based on the analysis of X-rays, emitted from the matter upon being bombarded by a high energy beam of charged particles like electrons or protons. The process of the X-ray emission is illustrated in Fig. 3.20. [76].

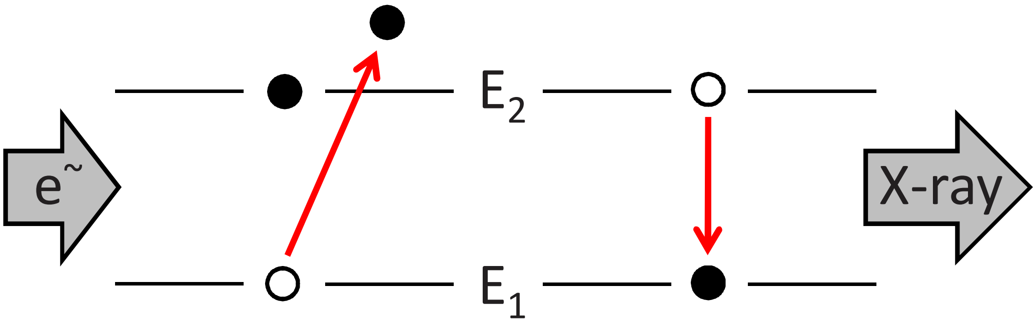

Figure 3.20: X-ray microanalysis is based on electronic transitions between inner atomic shells. An energetic electron from an electron column dislodges an orbital electron from a shell of low energy (E1). An electron from a shell of higher energy subsequently fills the vacancy, losing energy in the process. The lost energy appears as emitted radiation of energy E2 - E1. [76]

Each atom at rest contains ground state electrons, which are unexcited electrons. These electrons sit in different electron shells, which are bound to the nucleus. The incident beam do excite some electrons in some inner shells, kicking them out from their shells while creating holes where the electrons have been. Then some electrons from some outer higher energy shells fill the holes by traveling to the inner shells, where the hole are. Any traveling electron must give up an amount of energy equal to the energy difference between the inner and outer shell. The given up energy is released in the form of an X-ray, since the energy difference is large for inner shells. Each element in the specimen emits a unique pattern of X-rays and the energy of the emitted X-rays by the element gives a direct relationship to the concentration of that element. Then a series of electronic circuits do convert the emitted X-rays to a digital spectrum (see Fig. 3.21) [76]

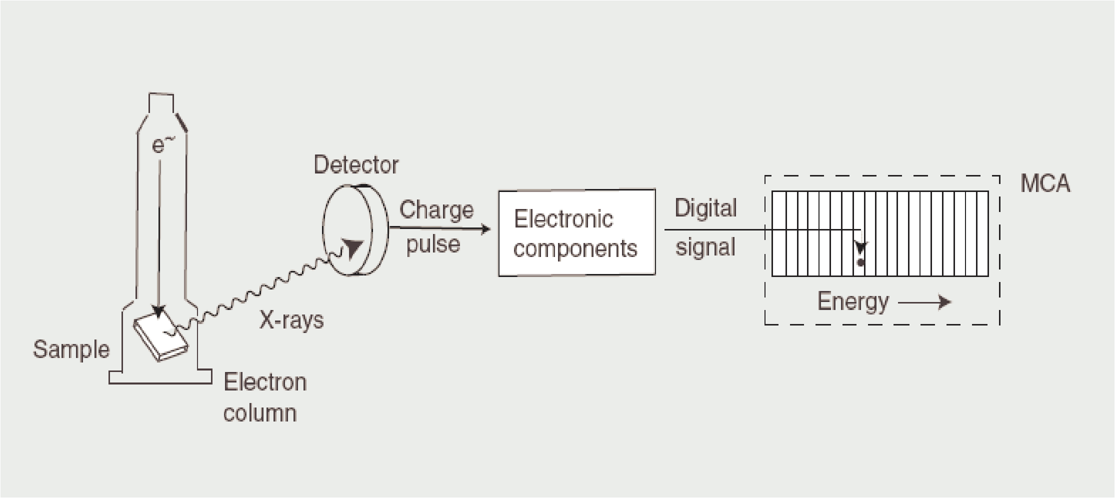

Figure 3.21: In energy dispersive microanalysis, each emitted X-ray produces a charge pulse in a semiconductor detector. This tiny and short-lived current is converted first into a voltage pulse, then into a digital signal reflecting the energy of the original X-ray. The digital signal, in turn, adds a single count to the appropriate channel of a multichannel analyzer (MCA). [76]

All emitted X-ray photons are detected by a semiconductor detector. Each emitted X-ray photon creates a charge pulse, when it hits the detector. Then the charge pulse is sent to some electronic circuits, which convert the charge pulse into a voltage pulse. The amplitude of the voltage pulse reflects the energy of the corresponding detected X-ray photon. Then the voltage pulse is converted by the same electronic circuits into a digital pulse, adding one count to the corresponding channel of a multichannel analyzer. Finally different accumulated counts from different channels create an X-ray spectrum (see Fig. 3.22. [76]).

In Fig. 3.22 the spectrum has some noise which leads to suspicious peaks or it makes the true peaks a little bit larger or smaller than expected. This noise or background is caused by some undesirable interactions. As a result of that, even a specimen of pure iron emits X-rays at other energies. So the procedure, which has to be done to extract the true peaks out of a noisy spectrum is as below: [76]

1. Remove the spurious peaks.
2. Identify the elements, which gives rise to the real peaks in the spectrum.

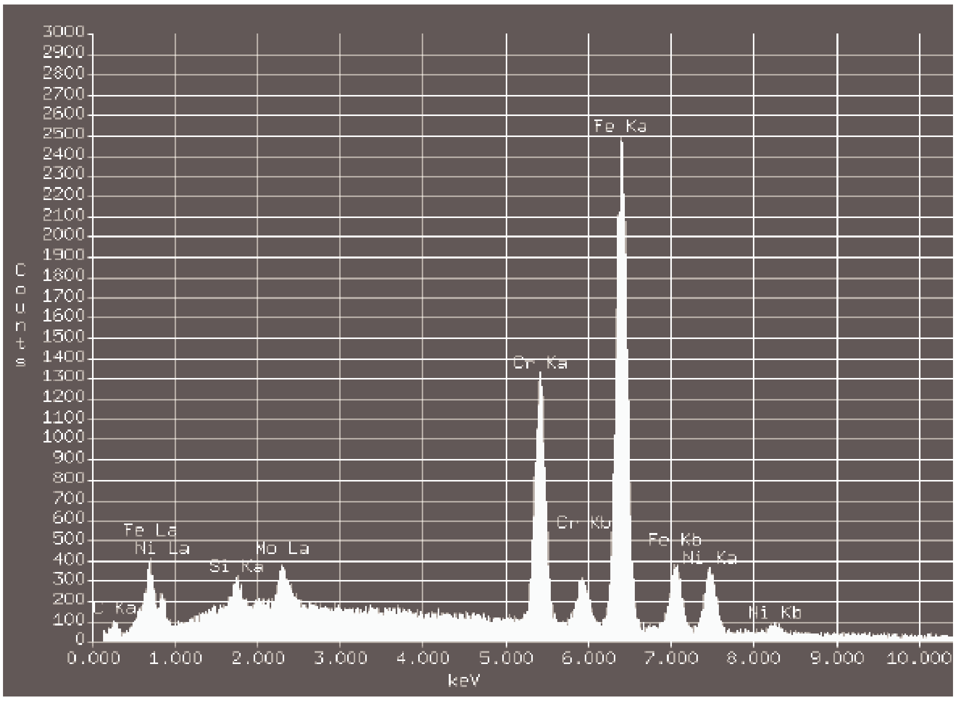

Figure 3.22: The dominant features of a typical X-ray spectrum include major spectral peaks superimposed on a broad background. A close look at the most intense peak (labeled FE Ka) reveals that the spectrum comprises a series of individual channels. [76]

3. Compute the concentrations of elements.

3.3.2 Laue Diffraction

Introduction:

The best method to determine how atoms in a crystal are arranged is the X-ray crystallography. In this method a beam of X-rays is involved, which hits the crystal and diffracts into many directions. X-rays can be considered as electromagnetic waves, so the best example to understand this technique is when a sea wave hits a lighthouse. This wave splits into many secondary waves, emanating from the lighthouse. So when an X-ray wave strikes an electron, the electron will produces many spherical secondary waves in many directions. This process called elastic scattering and the electrons are called scatters. Some of the secondary waves interfere destructively in most directions and therefore cancel each other and the rest interfere constructively in a few specific directions. The determination of these specific directions is due to Bragg's law: [77]

$$2dsin\theta = n\lambda \tag{3.9}$$

Where d is the distance between the diffracting planes, θ is the incident angle as illustrated in Fig. 3.23, n is any integer, and λ is the X-rays beam wavelength.

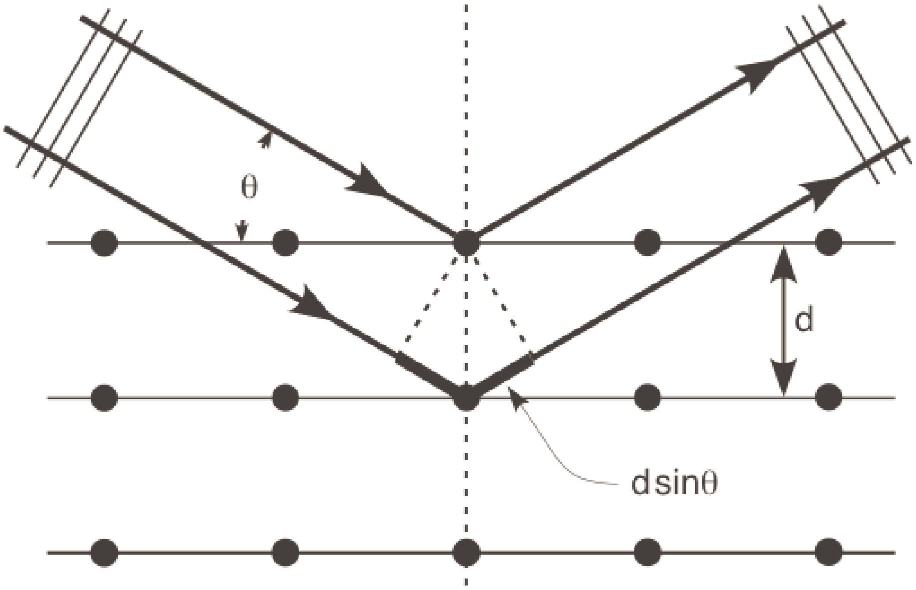

Figure 3.23: Diffraction of X-rays by a crystal. [77]

The resulting diffraction pattern has spots, which correspond to the constructively interfered secondary waves. These spots are called reflections. The arrangement of the detected reflections gives how the atoms are arranged in the crystal. The wavelength of X-rays is used to produced diffraction pattern, because it is the same order of magnitude as d. [77]

Transmission Laue camera:

The transmission Laue camera is illustrated in Fig. 3.24. A is a collimator, which is used to produce a very narrow beam of rays as nearly parallel as possible by having two pinholes in one line. B is the sample holder. C is the sample to be analyzed. F is the film holder or cassette. S is a small disk (about 0.5 mm thick), which is made of copper. This small disk does stop the beam, which means that a small fraction of the beam is transmitted through the disk toward the film. The transmitted beam through the disk marks the position of the beam on the disk. Once the beam is striking the sample, it gets diffracted by the sample atoms and then transmitted to the other side of the sample in many directions as shown in Fig. 3.24. The diffracted rays hit the film in many positions. These positions are the transmission Laue spots. [77] The Bragg angle, which corresponds to each Laue spot is given by the following relation: [77]

$$tan2\theta = \frac{r_1}{D} \tag{3.10}$$

Where D is the film to sample distance and r_1 is the distance between a spot and the center of the film. I would mention here that the film size is usually 10 × 13 cm and D is 5 cm. [77]

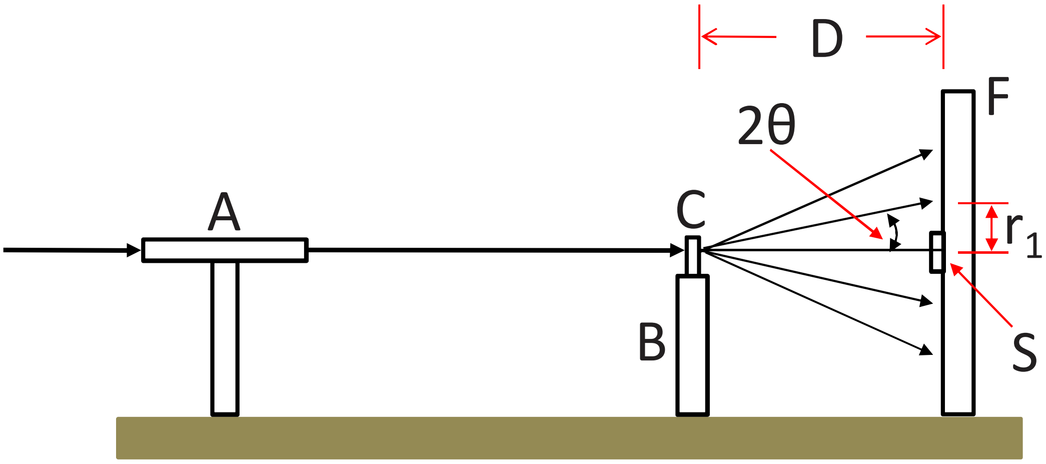

Figure 3.24: The schematic diagram of the transmission Laue camera. [77]

Back-reflection Laue camera:

Fig. 3.25 shows how the back-reflection Laue camera looks like. In this type the Bragg angle, which corresponds to each Laue spot is given by the following relation: [77]

$$tan(180^\circ - 2\theta) = \frac{r_2}{D} \tag{3.11}$$

Our Laue diffraction measurements have been done using the back-reflection Laue camera. I would also mention here that D in this type is usually 3 cm. [77]

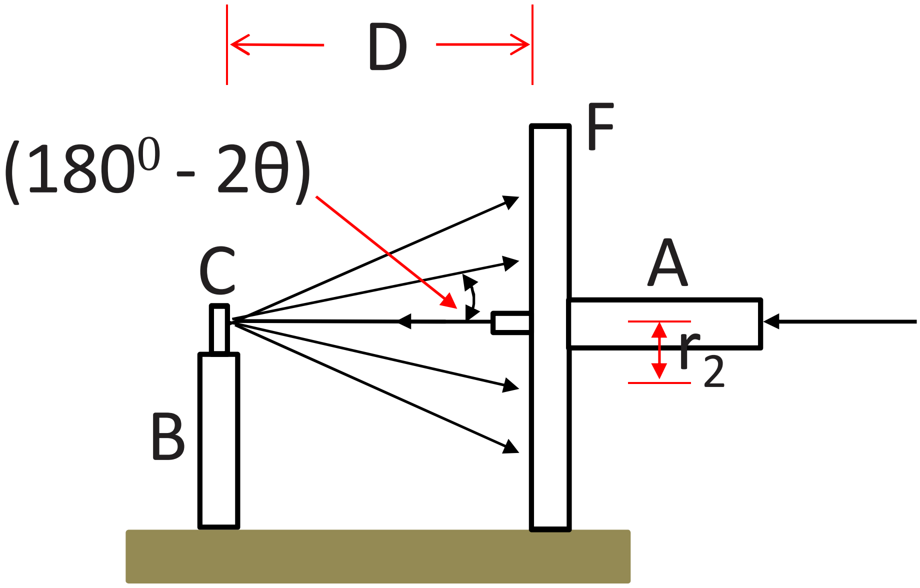

Figure 3.25: The schematic diagram of the back-reflection Laue camera. [77]

4 Results and discussion

EDX, Laue diffraction, dc transport, and IR reflectivity measurements have been performed on pure, Rb-doped, and W-doped blue bronze single crystals. The results, analysis, and discussion are described in this chapter.

4.1 EDX measurements

Figs. 4.1, 4.2, and 4.3 show respectively the areas from which the EDX spectra of the pure, Rb-doped, and W-doped blue bronze samples have been taken. They also show the EDX spectra of the pure, Rb-doped, and W-doped blue bronze samples respectively.

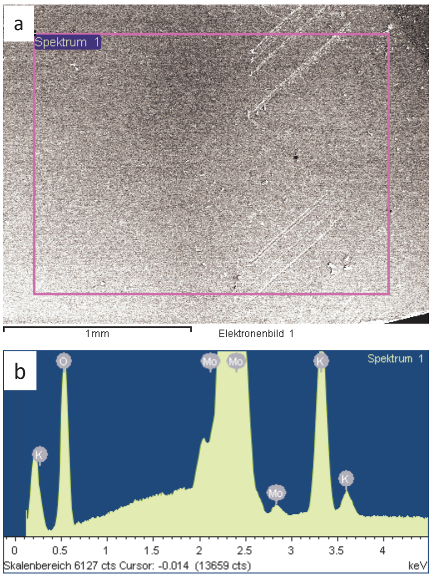

Figure 4.1: (a) The area, from which the EDX spectrum of the pure blue bronze sample has been taken. (b) The EDX spectrum of the pure blue bronze sample.

From the EDX spectra we have got the atomic percent M of each element in all studied samples and by applying Eq. 4.1 we have checked the number of atoms per formula unit N (stoichiometry) of all studied samples.

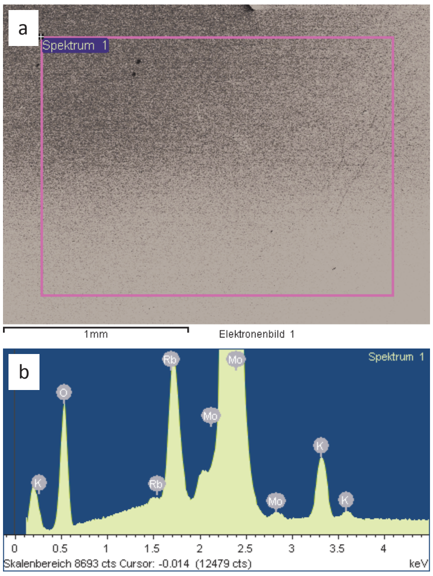

Figure 4.2: (a) The area, from which the EDX spectrum of the Rb-doped blue bronze sample has been taken. (b) The EDX spectrum of the Rb-doped blue bronze sample.

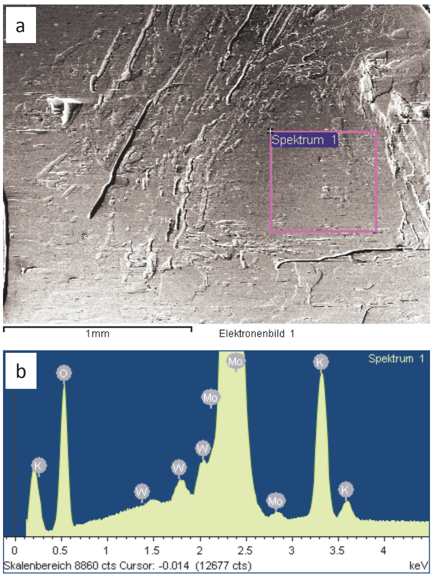

Figure 4.3: (a) The area, from which the EDX spectrum of the W-doped blue bronze sample has been taken. (b) The EDX spectrum of the W-doped blue bronze sample.

$$N = \frac{M}{100} \cdot 4.3 \tag{4.1}$$

The results are tabulated in Table 4.1.

Element	M	N
K of $K_{0.3}MoO_3$	6.05	0.26
Mo of $K_{0.3}MoO_3$	21.70	0.93
O of $K_{0.3}MoO_3$	72.24	3.10
K of $(K_{0.5}Rb_{0.5})_{0.3}MoO_3$	3.13	0.134
Rb of $(K_{0.5}Rb_{0.5})_{0.3}MoO_3$	3.39	0.145
Mo of $(K_{0.5}Rb_{0.5})_{0.3}MoO_3$	23.26	1.000
O of $(K_{0.5}Rb_{0.5})_{0.3}MoO_3$	70.21	3.019
K of $K_{0.3}Mo_{0.99}W_{0.01}O_3$	6.47	0.278
Mo of $K_{0.3}Mo_{0.99}W_{0.01}O_3$	22.44	0.964
W of $K_{0.3}Mo_{0.99}W_{0.01}O_3$	0.33	0.014
O of $K_{0.3}Mo_{0.99}W_{0.01}O_3$	70.76	3.042

Table 4.1: The EDX results.

4.2 Sample mask and Laue diffraction

We have used the Laue camera to determine the samples' orientations (b axis). The orientations (indicated by blue big arrows) of the pure, Rb-doped, and W-doped blue bronze samples are shown in Figs. 4.4, 4.5, and 4.6 respectively. Also the dimensions of the masks' openings are shown in the figures for all studied samples, noticing that the weight lines show the edges of the samples.

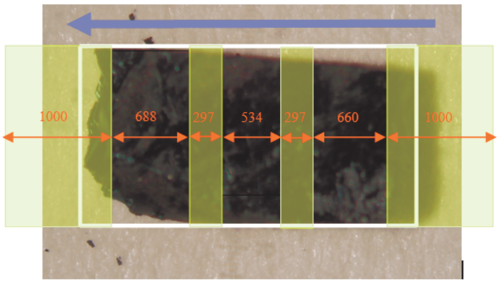

Figure 4.4: The orientation of the pure blue bronze sample, based on the Laue camera picture. The shown dimensions are in micrometers.

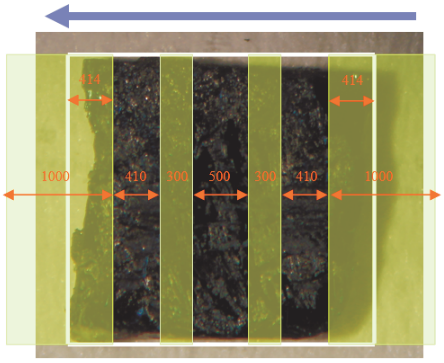

Figure 4.5: The orientation of the Rb-doped blue bronze sample, based on the Laue camera picture. The shown dimensions are in micrometers.

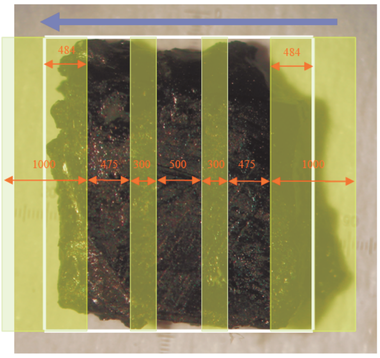

Figure 4.6: The orientation of the W-doped blue bronze sample, based on the Laue camera picture. The shown dimensions are in micrometers.

4.3 Dc transport measurements

In our dc electrical transport measurements a four-probe configuration has been used. Since the samples are highly anisotropic, Laue diffraction has been used to determine the prepared samples' orientations. In the contact regions, indium films (150 thickness) have been covered by gold films (also 150 thickness) to achieve a stable contacting at low temperatures as mention in the experiments chapter.

4.3.1 Resistivity measurements

Our measurements show that the Peierls transition of the pure blue bronze sample takes place sharply near 180K, resulting in a metal-insulator transition due to the CDW formation. Also our measurements show that doping with rubidium and tungsten decreases the transition temperature and smears out this metal-insulator transition. Fig. 4.7 shows the temperature dependence of the specific resistivity along the chain direction (b axis) of the pure, Rb-doped, and W-doped blue bronze samples.

To determine the Peierls transition temperature T_P, two methods are commonly used:

1. From the $\rho(T)$ curve: T_{P1} is defined at the resistivity anomaly (see the inset of Fig. 4.7). When the transition is smeared out, then it will be very difficult to determine the Peierls transition temperature (the W-doped and Rb-doped blue bronze samples in our case). So this method is accurate only in the case of the pure blue bronze sample, because the transition is very sharp (see Fig. 4.7).

2. From the D(T) curve, where $D(T) = -\partial \ln\sigma / \partial T^{-1}$ with σ the conductivity along the b direction [78]. T_{P2} is defined at the peak position of the curve, as shown in Fig. 4.8. The determined Peierls transition temperature by this method is much more accurate than the one, determined by the first method. Fig. 4.8 depicts the D(T) curves of the pure and doped blue bronze samples. Compared with rubidium doping, the tungsten doping greatly broadens the transition peak and reduces the transition temperature (see Fig. 4.8). The so-obtained Peierls transition temperature from the D(T) curve is slightly lower than that directly obtained from the $\rho(T)$ curve (see Table 4.2).

Also we have observed a pseudogap in the electronic density of states. Fig. 4.9 shows the temperature dependence of the specific resistivity of the pure blue bronze sample, which shows that this gap opens up at around 225 K. One can easily see in the figure that there is a linear temperature dependence above 225 K which is known

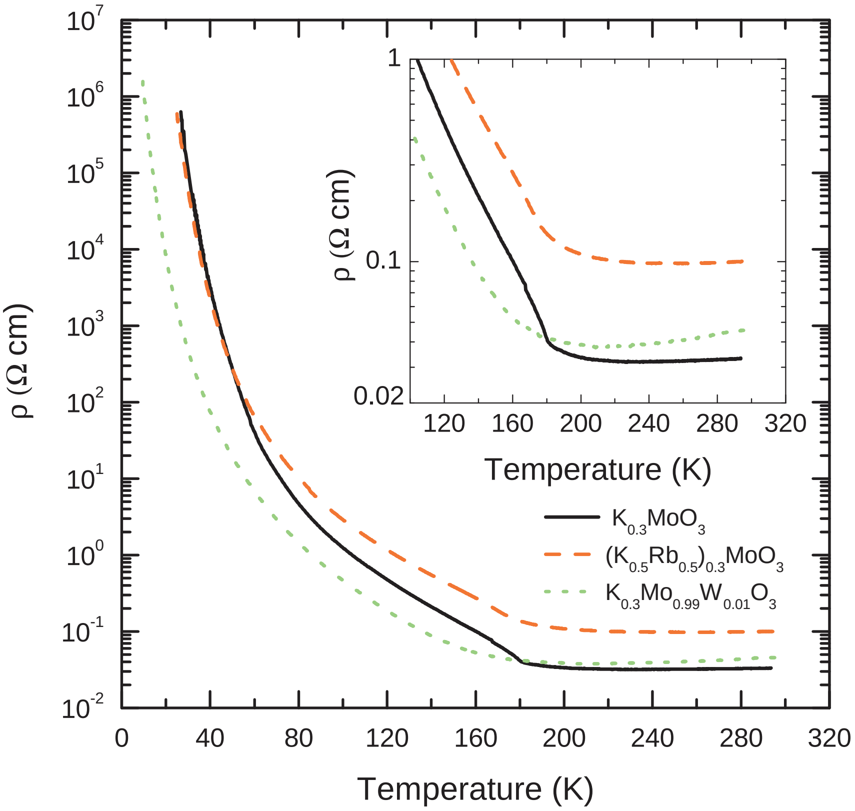

Figure 4.7: The temperature dependence of the specific resistivity of all studied samples.

Sample	T_{P1} (K)	T_{P2} (K)
$K_{0.3}MoO_3$	180	179
$(K_{0.5}Rb_{0.5})_{0.3}MoO_3$	X	170
$K_{0.3}Mo_{0.99}W_{0.01}O_3$	X	140

Table 4.2: The determined Peierls transition temperature using two methods; from the R(T) curve (T_{P1}) and from the D(T) curve (T_{P2}).

for conventional metals at high temperatures. [49] While the pseudogap opens up at around 266 K in the Rb-doped blue bronze sample and at around 230 K in the W-doped blue bronze sample. The pseudogap is due to the pretransitional fluctuations of the CDW ground state. [49] So the fluctuations of the CDW ground state of the pure and W-doped blue bronze samples start at more or less the same temperature, while the fluctuations of the CDW ground state of the Rb-doped blue bronze sample starts at a higher temperature (266 K). Figs. 4.10 and 4.11 show the pseudogap opening for

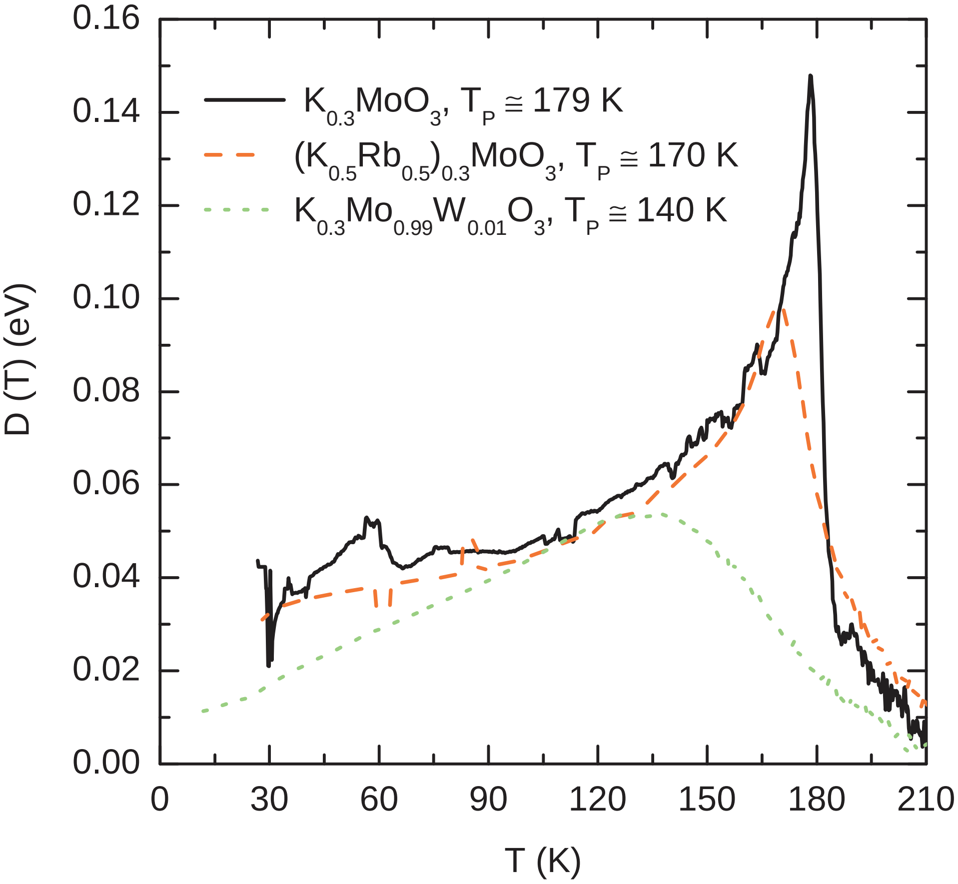

Figure 4.8: The derivative D = $-\partial \ln\sigma / \partial T^{-1}$ versus temperature.

the W-doped and Rb-doped blue bronze samples, respectively.

Fig. 4.7 shows the temperature dependence of the specific resistivity for all studied samples. All samples have qualitatively the same behavior, but there are characteristic differences in the Peierls transition temperature T_P and the room temperature resistivity. All systems show low resistivities, high conductivities (see Table 4.3), at room temperature. A decrease of resistivity with lowering the temperature above ${T_P}^{MF}$ is observed in all samples, which is expected for a Q1D metal as mentioned above. At T_P the slop of ρ(T) changes abruptly and the resistivity below T_P increases rapidly due to the opening of a BCS-like energy gap at the Fermi level. Based on the BCS relation [$2\Delta(T) = 3.5\kappa_T {T_P}^{MF}$], $\Delta(0)$ of all studied samples has been obtained (see Table 4.3). [49]

In the case of real Peierls transition temperature T_P, a constant (4-11) should be used instead of 3.5. Accordingly, a constant of 4 has been used in the BCS relation. [49]

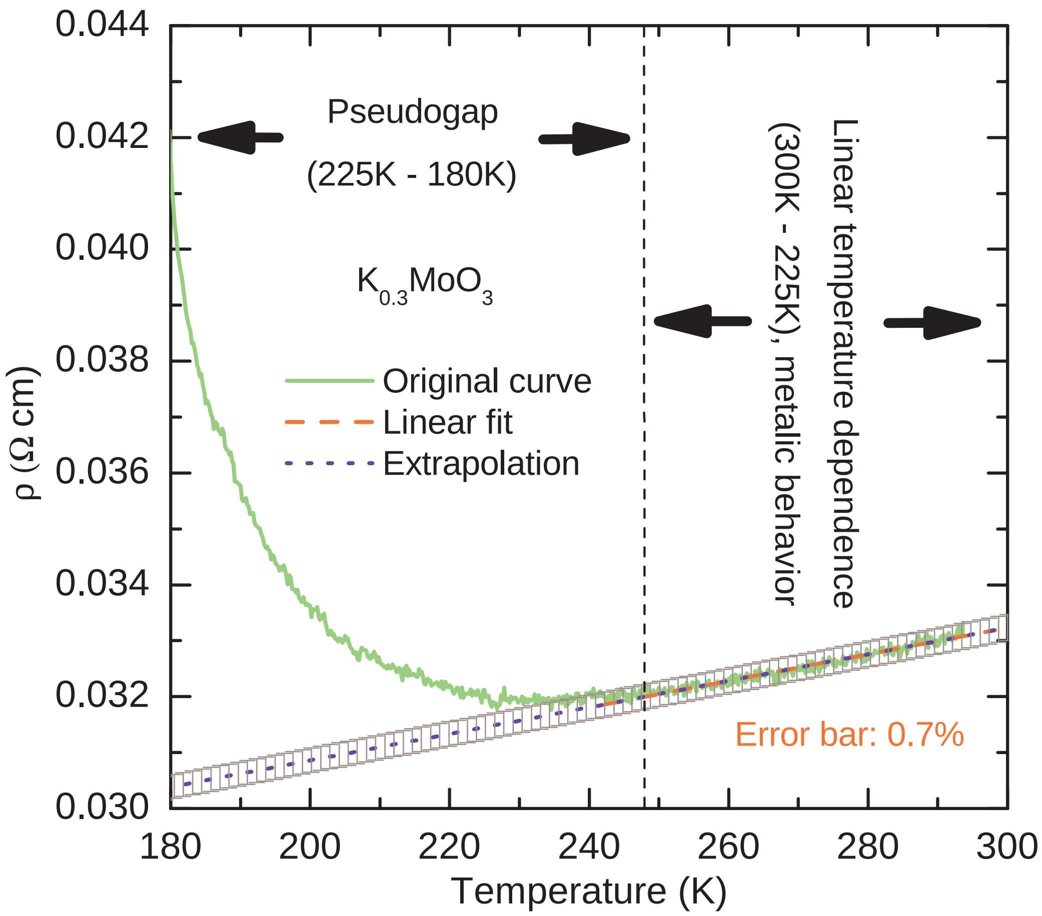

Figure 4.9: Temperature dependence of the specific resistivity of the pure blue bronze sample above the Peierls transition. The dashed red line indicates a linear temperature dependence above 225 K, which is known from conventional metals at high temperatures.

4.3.2 The temperature dependence of the Peierls energy band gap

Bruetting et al. [49] has developed a model, which allows for the determination of the temperature dependence of the energy band gap below and above the Peierls transition temperature T_P directly from the dc-conductivity (resistivity) data in organic and inorganic CDW conductors. This model has been applied to $K_{0.3}MoO_3$. The calculated temperature dependence of the energy band gap shows the typical behavior of a Q1D conductor with a Peierls transition to a CDW ground state. Below T_P the Peierls energy band gap follows a scaled mean-field dependence, while there remains a pseu-

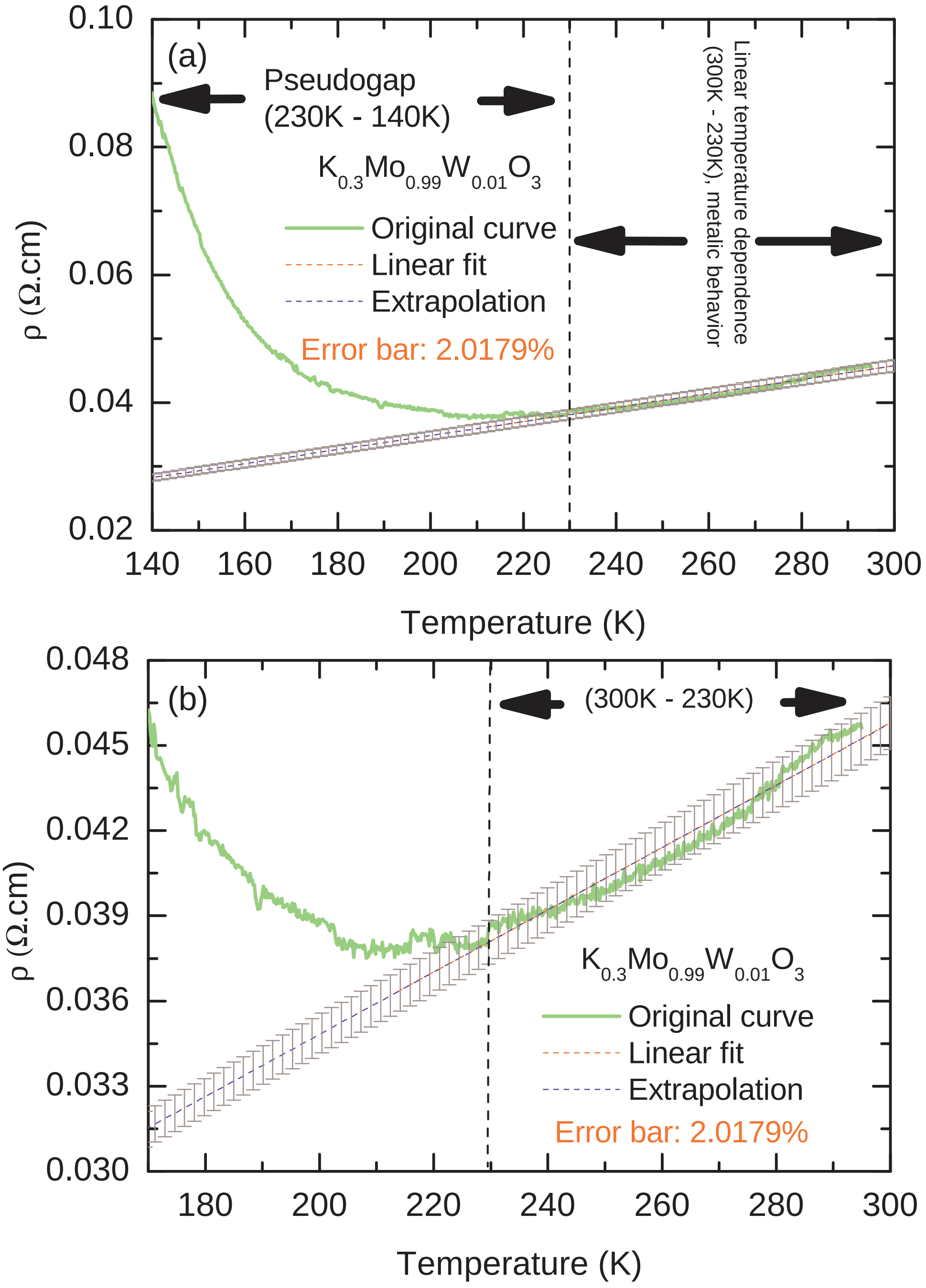

Figure 4.10: Temperature dependence of the specific resistivity of the W-doped blue bronze sample above the Peierls transition. The dashed red line indicates a linear temperature dependence above 230 K, which is known from conventional metals at high temperatures.

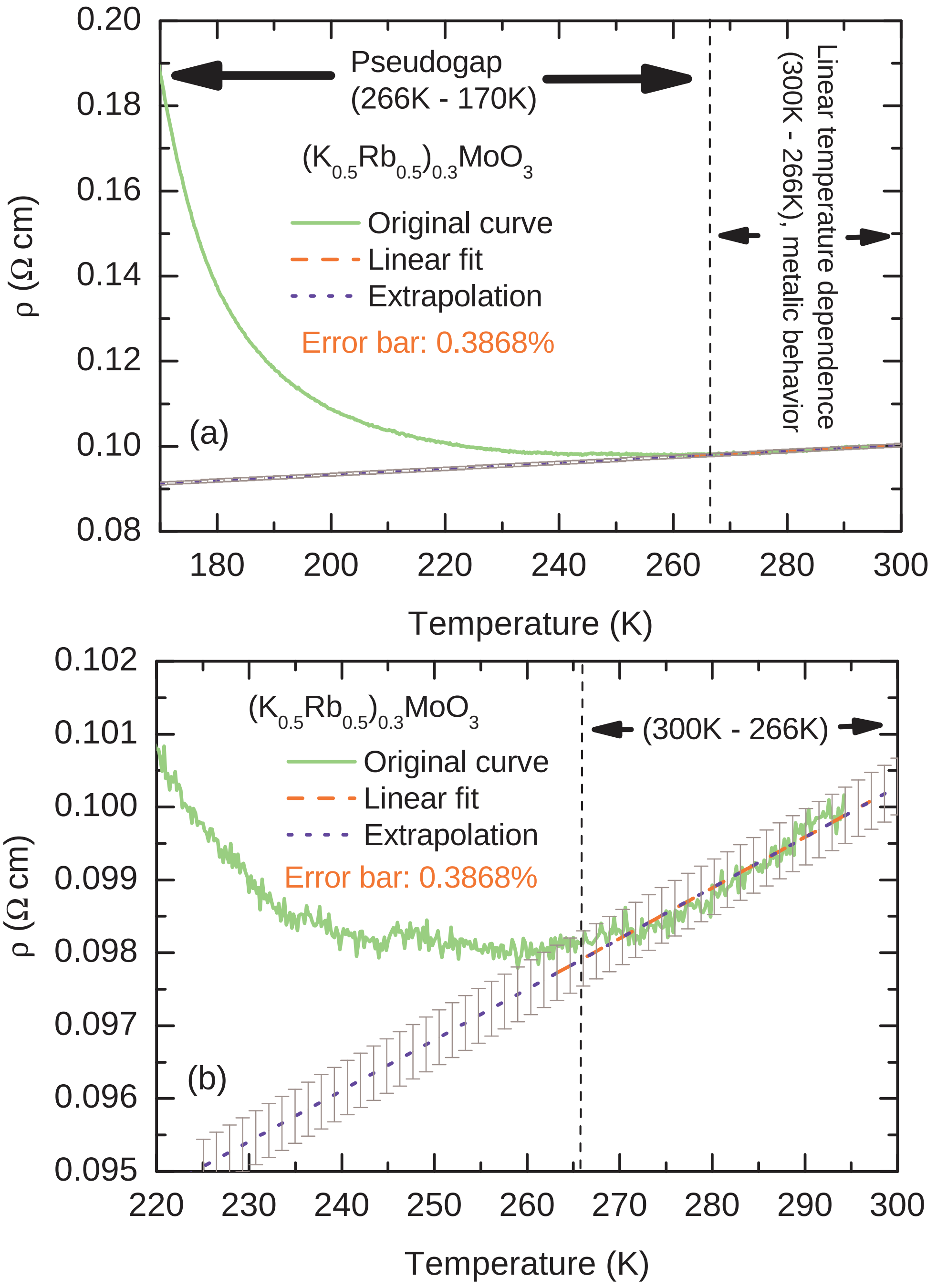

Figure 4.11: Temperature dependence of the specific resistivity of the Rb-doped blue bronze sample above the Peierls transition. The dashed red line indicates a linear temperature dependence above 266 K, which is known from conventional metals at high temperatures.

Parameter	**Pure sample**	**Rb-doped**	**W-doped**
$\mathrm{T}_P{}^{MF}$ (K)	225	266	230
$\Delta(0)$ (meV)	38.77	45.84	39.63
$\sigma(300$ K) $(\Omega^{-1}cm^{-1})$	30.01	9.98	21.92

Table 4.3: Parameters, characterizing the three studied samples. The mean-field transition temperature for each samples has been determined from our data, as mentioned above. The low temperature activation energy $\Delta(0)$ for each sample has been calculated using the BCS relation. The room temperature conductivity $\sigma(300$ K) for each sample has been obtained from our data. $\Delta(0)$ of our pure blue bronze sample is consistent with previous data in Ref. [49].

dogap due to CDW fluctuations above T_P up to the mean-field transition temperature $\mathrm{T}_P{}^{MF}$. We have integrated the model and applied it to our studied samples to get Δ(T) from our own dc-conductivity data by using the following equation: [49]

$$\sigma(T) = C \cdot \frac{ln(1 + e^{-\Delta(T)/\kappa_B T})}{\Delta(T)} \tag{4.2}$$

where κ_B is Boltzman constant and C is given by the following equation for a vanishing gap ($\Delta \equiv 0$): [49]

$$C = 4\sigma\kappa_B T \tag{4.3}$$

Fig. 4.12 shows the calculated Δ(T) of all studied samples. It is obvious from the figure that the Peierls energy band gap below T_P follows a scaled mean-field dependence. We have plotted the data up to 65 K, because Δ(T) starts to go down below 65 K in the Rb- and W-doped blue bronze samples. While Δ(T) starts to be unreasonable in the pure blue bronze sample. If we suppose that Δ(T) get saturated below 65 K, then the calculated Δ(65 K) of the pure blue bronze sample (see Fig. 4.12) is close to the calculated one using the BCS relation (see Table 4.3).

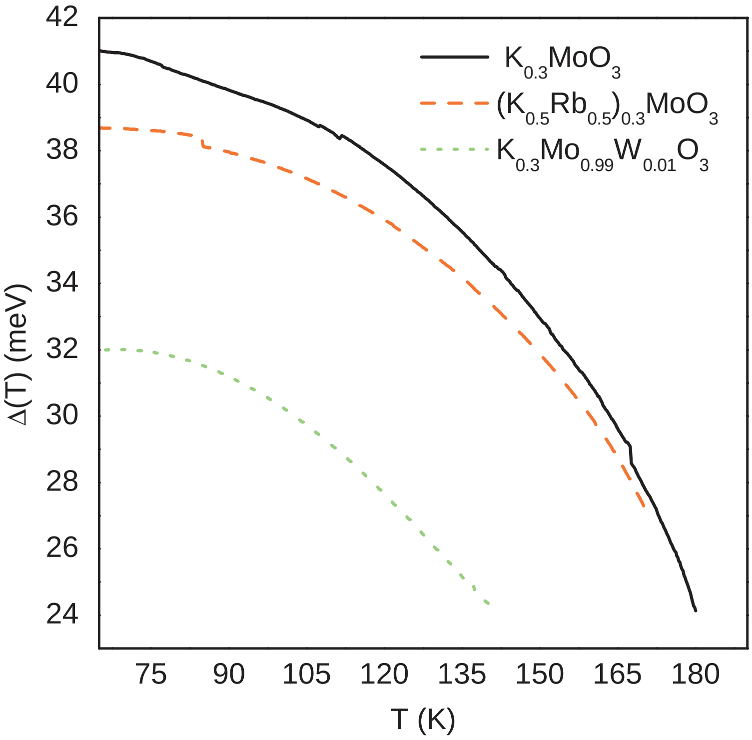

Figure 4.12: The temperature dependence of the energy gap of all studied samples, determined from our conductivity data.

4.3.3 Current-Voltage (I-V) response measurements

The nonlinear current-voltage response due to the CDW sliding has been observed in all studied samples. I would mention here that for these measurements, the current has been applied in this sequence:

1. Path 1 (N-0, see Fig. 4.13), which starts from a maximum negative value (-ve I_{max}) and then decreases every 2 seconds until it reaches zero.
2. Path 2 (0-P, see Fig. 4.13), which starts from zero and then increases every 2 seconds until it reaches a maximum positive value (+ve I_{max}).
3. Then there is a break of 10 seconds before the third pulse takes place (path P-0, see Fig. 4.13) and so on until the fourth path takes place (path 0-N, see Fig. 4.13).

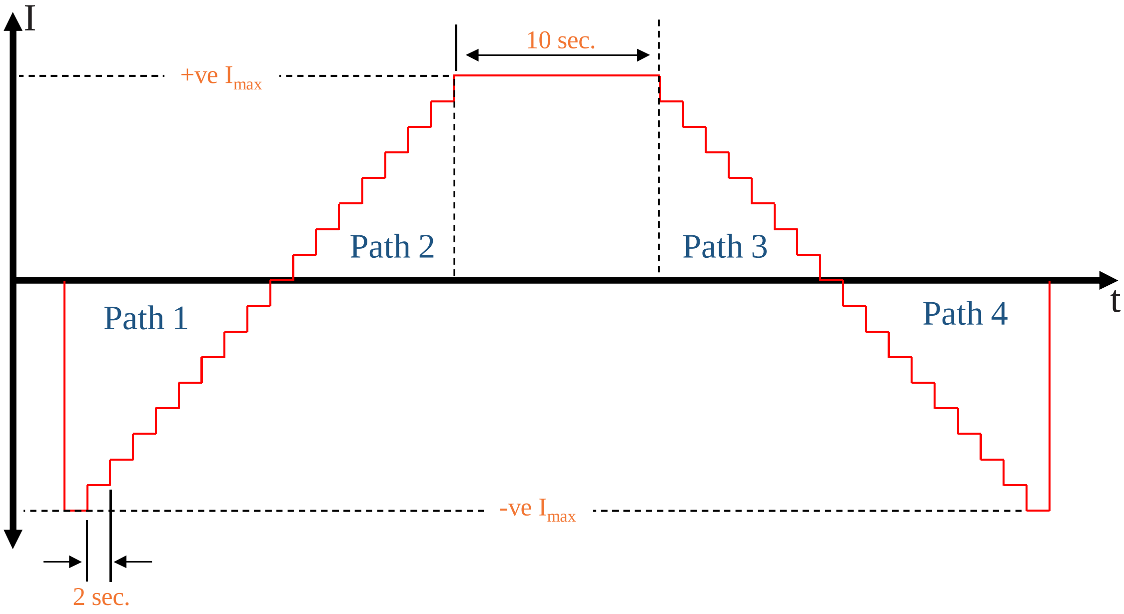

Figure 4.13: The applied current pulses.

The resultant I-V response is illustrated in Fig. 4.14, as an example (see also Figs. .1, .2, .3, .4, and .5 in the appendix). Fig. 4.15 shows the I-V characteristics curve of the pure blue bronze sample at four different temperatures. Fig. 4.15(a) shows that the current always increases with increasing the voltage linearly signaling the Ohmic behavior and thus the CDW is not yet formed. The current starts to increase nonlinearly exactly at T_P (180 K) after exceeding a threshold voltage V_T, signaling the CDW sliding [see Fig. 4.15(b)]. The I-V curves at 100 K and 40 K have been added in the figure to show that the nonlinearity increases when the temperature is lowered, signaling an increase in the CDW sliding [see Figs. 4.15(c) and 4.15(d)]. Furthermore, Fig. 4.15(d) shows that there is a second threshold voltage $V_T{}^*$ at which the I-V curve bends back, signaling a huge increase in the CDW sliding. Finally I would mention here that it is clear from Figs. 4.15(b), 4.15(c), and 4.15(d) that V_T is temperature dependent. Also we have observed that $V_T{}^*$ is temperature dependent. The nonlinearity starts at 170 K for the Rb-doped blue bronze sample while it starts at 140 K for the W-doped blue bronze sample as shown in Figs. 4.16 and 4.17, respectively.

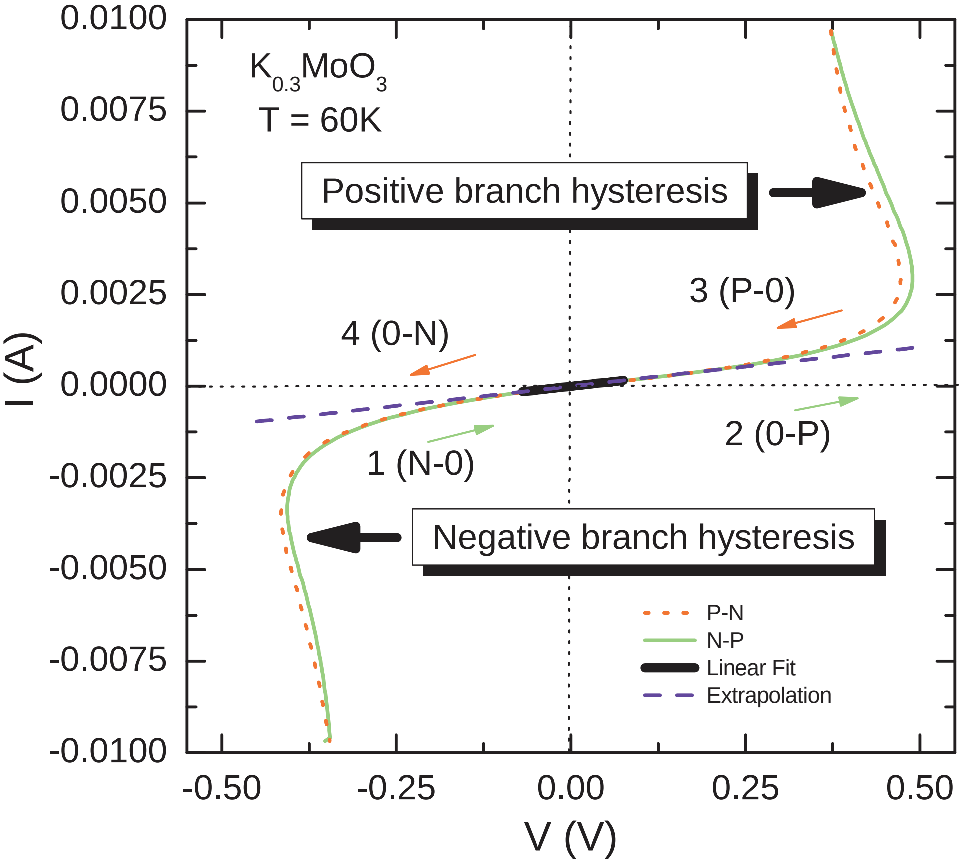

Figure 4.14: The I-V characteristics curves of the pure blue bronze at 60 K for the N-P and P-N paths. Path N-P means paths N-0 and 0-P, while path P-N means path P-0 and 0-N.

In order to determine $E_T(T)$ and $E_T{}^*(T)$ of all studied samples, the following procedure has been done:

- We selected a range of voltages where the I(V) curve is for sure linear, did fit it linearly, and then extrapolated the linear fit over the whole voltage range as shown in Fig. 4.14.
- Then we subtracted the total I(V) curve from the extrapolated linear fit and the resulted ΔI(V) is plotted in Fig. 4.18. Before the deviation of the I(V) curve from the extrapolated linear fit starts, ΔI(V) is zero (Ohmic regime). Once the deviation starts, ΔI begins to increase as shown in Fig. 4.18 nonlinearly with increasing the voltage. This nonlinear increase of ΔI signals the CDW sliding. As the criterium for determining the value of the first threshold voltage (V_T) at which the nonlinear increase of ΔI starts, we did choose $\Delta I = 10^{-5}$ A and use

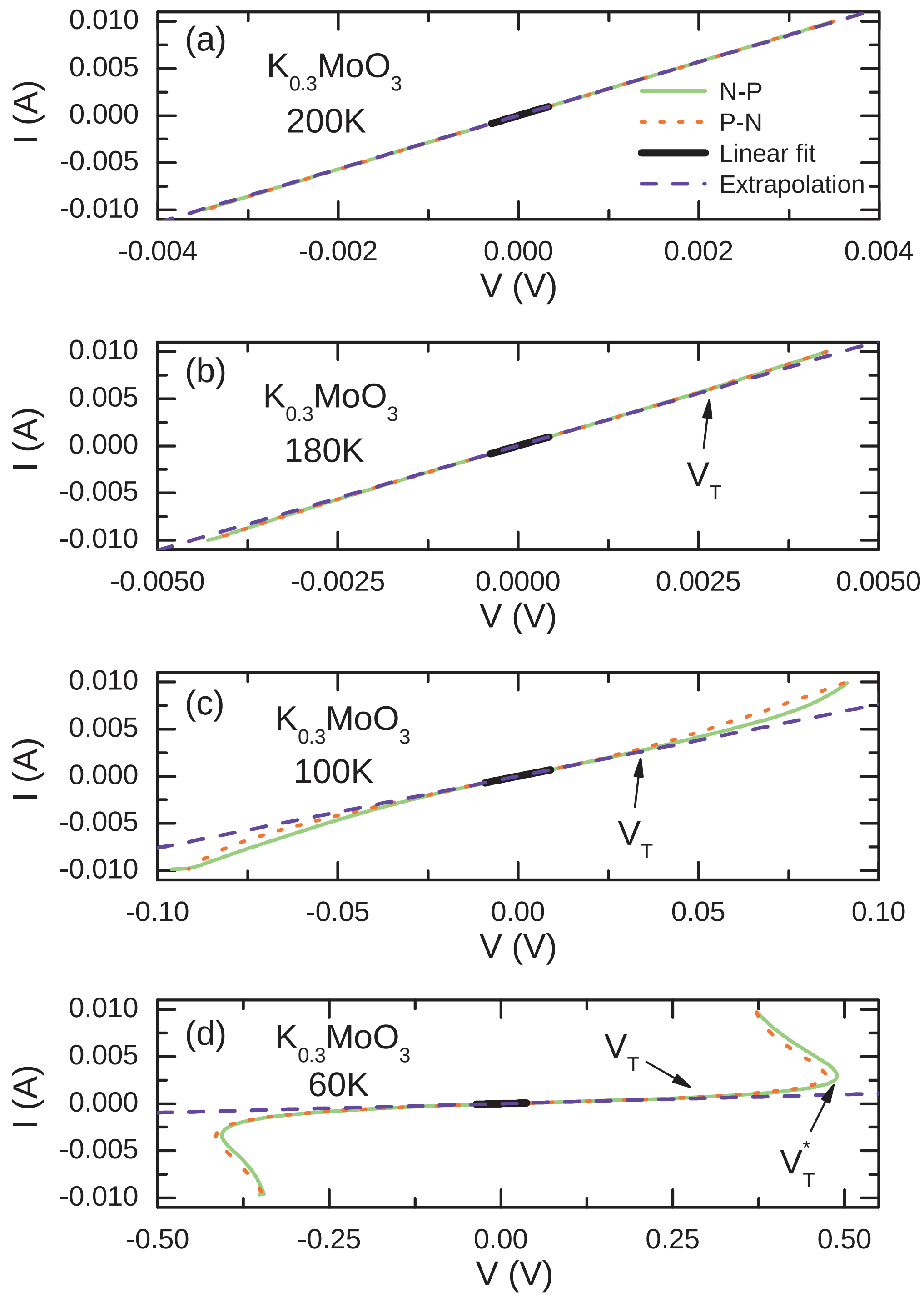

Figure 4.15: The I-V characteristics curve of the pure blue bronze sample at four different temperatures.

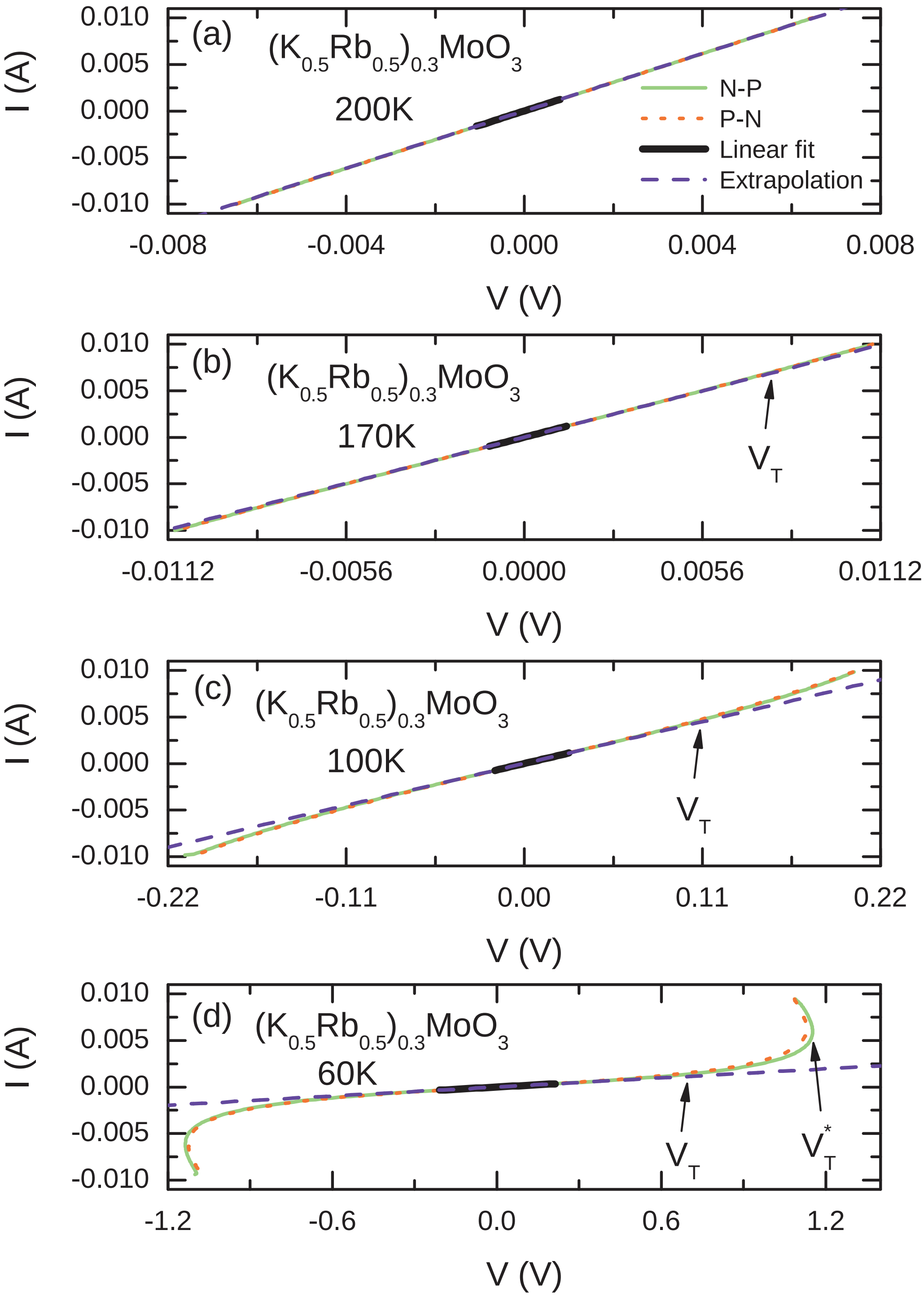

Figure 4.16: The I-V characteristics curve of the Rb-doped blue bronze sample at four different temperatures.

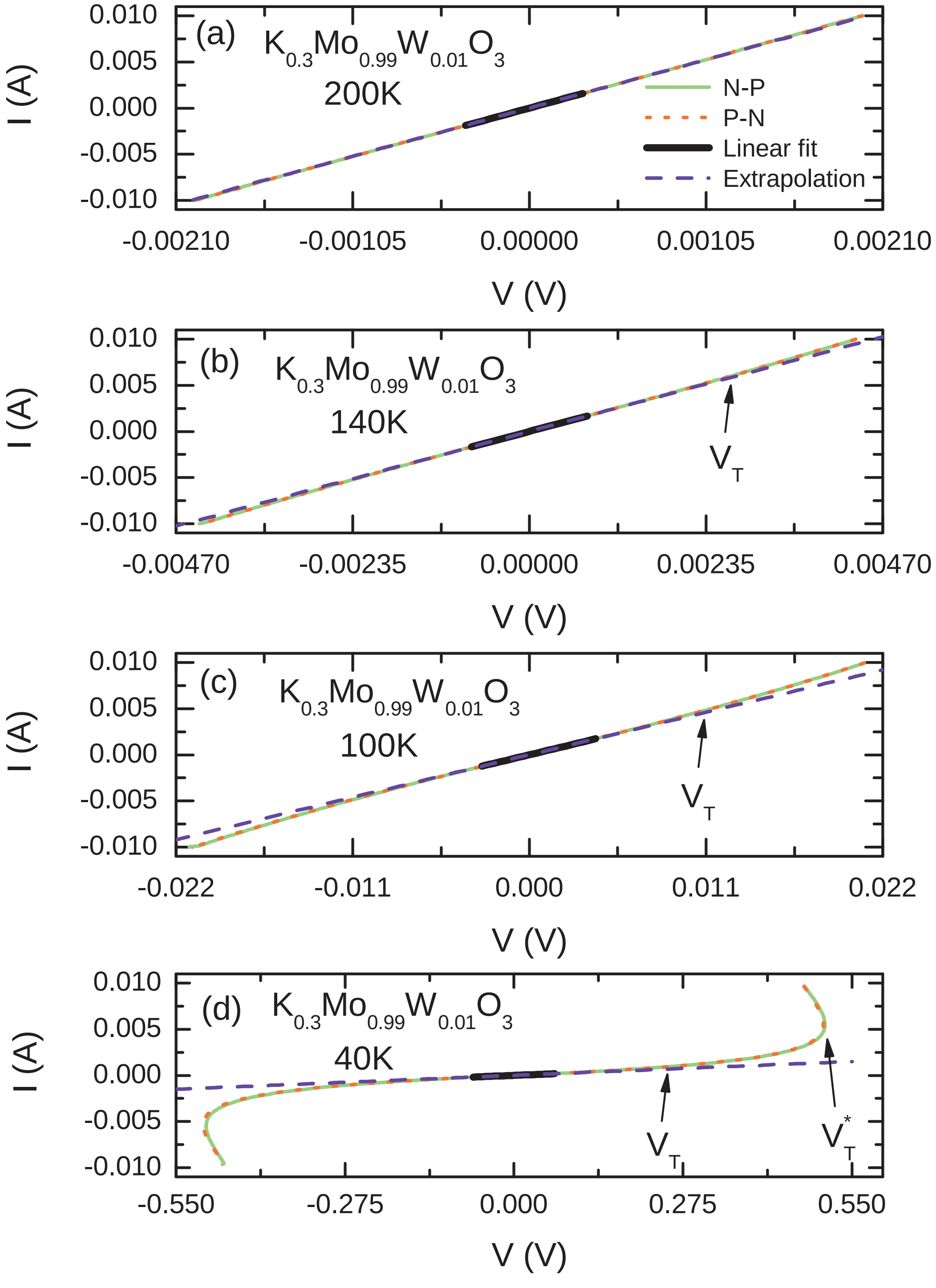

Figure 4.17: The I-V characteristics curve of the W-doped blue bronze sample at four different temperatures.

> it for all studied samples at all temperatures. So the corresponding voltage is V_T and thus $E_T = V_T$ / l (see Fig. 4.20). Above V_T the I(V) curve bends back as shown in Fig. 4.14, resulting in a huge increase in ΔI. This signals a second threshold voltage $V_T{}^*$ and thus $E_T{}^* = V_T{}^*$ / l (see again Fig. 4.20). We have determined $V_T{}^*$ by taking the derivative of the I(V) curve and thus the peak position of the resulting curve is $V_T{}^*$ as shown in Fig. 4.19.

ΔI(V) is path-dependent, which makes E_T and $E_T{}^*$ become path-dependent as well. Fig. 4.20 shows the temperature dependence of the first threshold field of all studied samples for the four paths separately. It is clear from the figure that the threshold field increases monotonically with cooling down and this has been observed in all studied samples.

Also it is obvious from the figure that E_T(T) of all studied samples seems to be path dependent. So we have plotted the average value of E_T versus temperature as shown in Fig. 4.21, where:

$$AveragedE_T = (E_T(N-0) + E_T(0-P) + E_T(P-0) + E_T(0-N))/4 \tag{4.4}$$

It is obvious from Fig. 4.21 that the averaged E_T of all studied samples still increases monotonically with cooling down. Also the absolute values of the threshold field are the highest in the Rb-doped blue bronze sample and the lowest in the W-doped blue bronze sample over the whole temperature range.

Fig. 4.22 shows the temperature dependence of the first threshold field of all studied samples for the four paths together. It is obvious from the figure that E_T(T) of the pure and Rb-doped blue bronze samples are path-dependent at some temperatures as shown in Figs. 4.22(a) and 4.22(b). While E_T(T) of the W-doped blue bronze sample is path-independent at all temperatures except at 20 K, where there might be some path dependence as shown in Fig. 4.22(c).

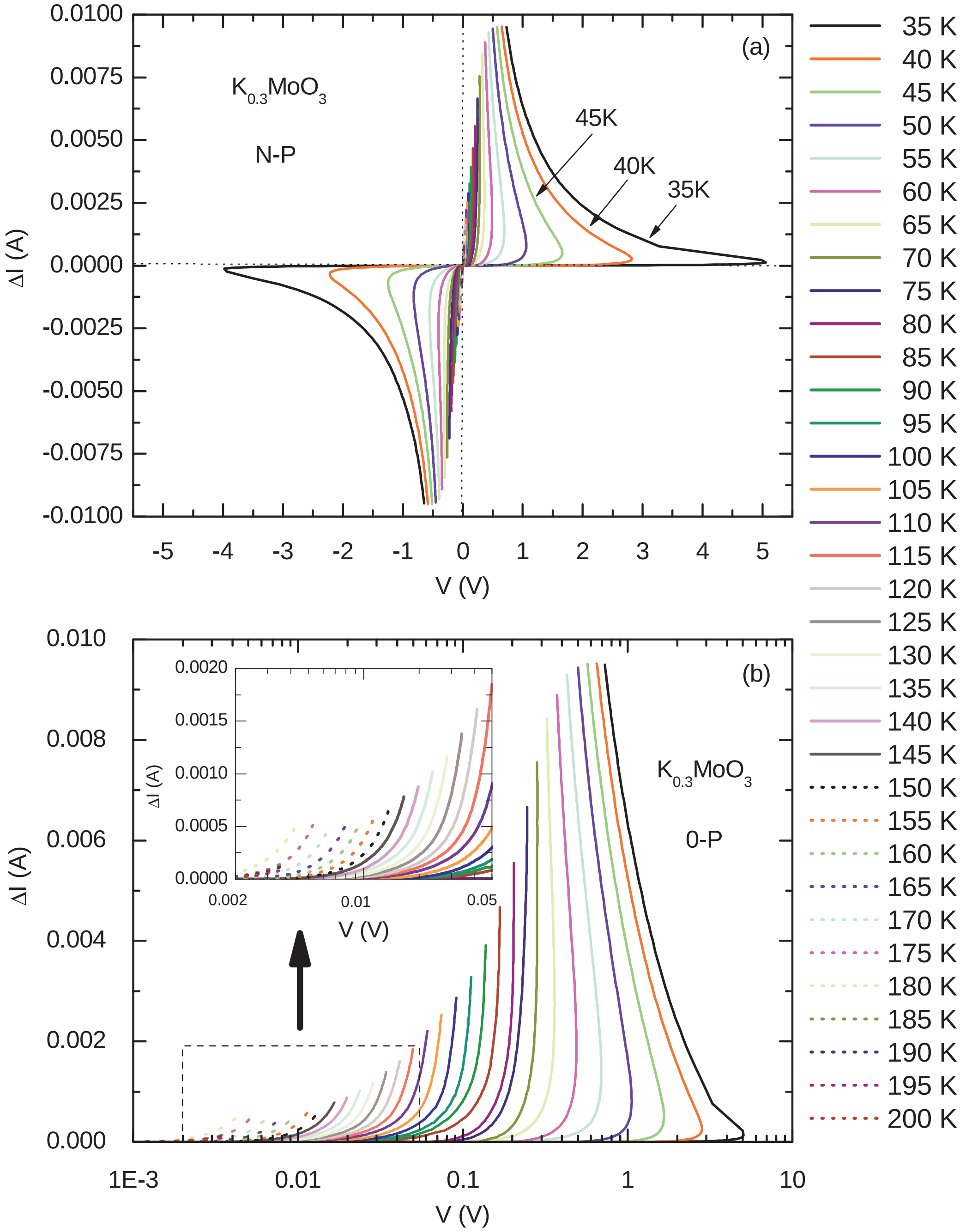

Figure 4.18: ΔI versus voltage of $K_{0.3}MoO_3$ at different temperatures; (a) ΔI(V) for the N-P path, which includes the N-0 and 0-P paths. (b) ΔI(V) for the 0-P path.

Fig. 4.23 shows the temperature dependence of the second threshold field of all studied samples for the four paths together. It is clear from the figure that $E_T{}^*$

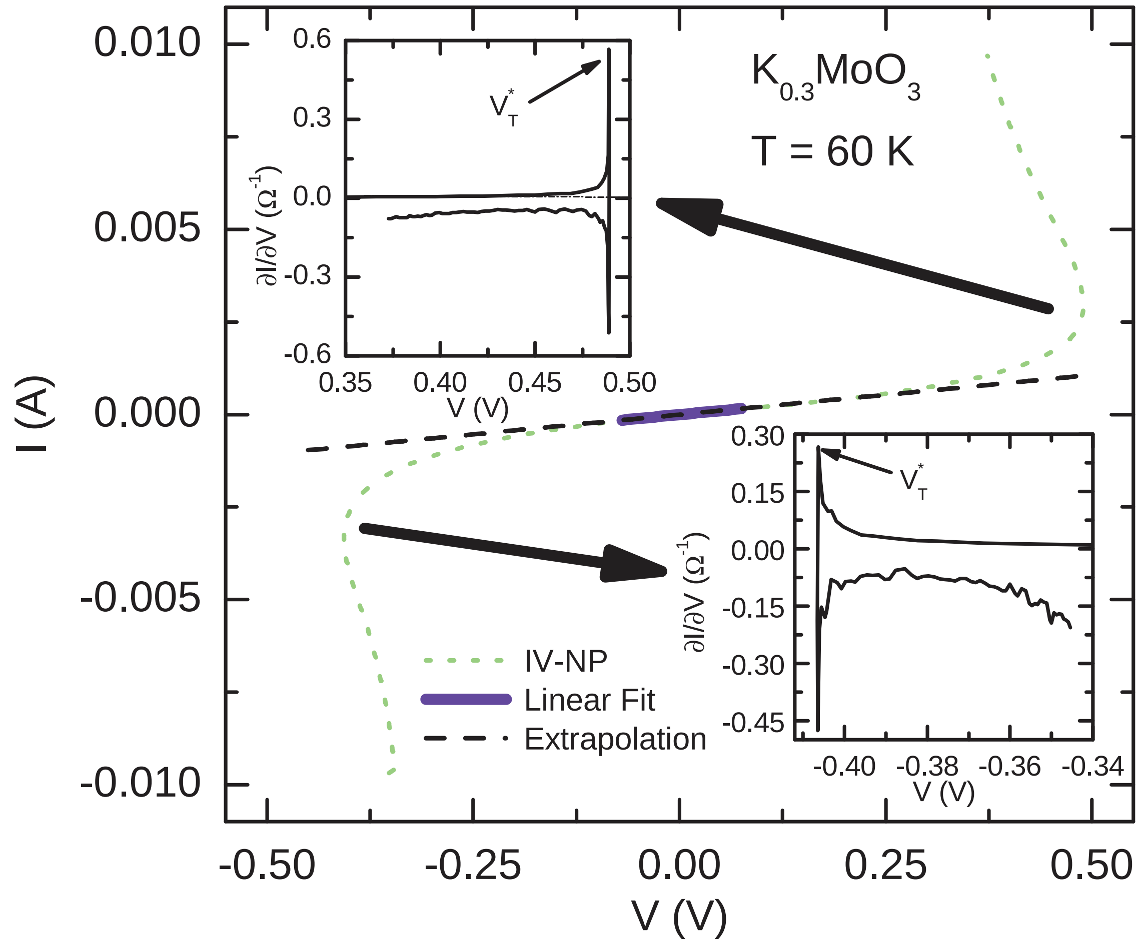

Figure 4.19: The I-V characteristics curve of $K_{0.3}MoO_3$ at 60 K for the N-P path. The inset on the left-top corner shows the derivative of the I-V curve in the positive branch (0-P path); the voltage at the peak position of the resulting curve is $V_T{}^*$ for the 0-P path, while the inset on the right-button corner shows the derivative of the I-V curve in the negative branch (N-0 path); the voltage at the peak position of the resulting curve is $V_T{}^*$ for the N-0 path.

increases monotonically with cooling down and this has been observed in all studied samples. Also the following is obvious from the figure:

- $E_T{}^*$ of the pure blue bronze sample is path-dependent at all temperatures except 65 K, as shown in Fig. 4.23(a).
- $E_T{}^*$ of the Rb-doped blue bronze sample is path-dependent only at 35 K, as

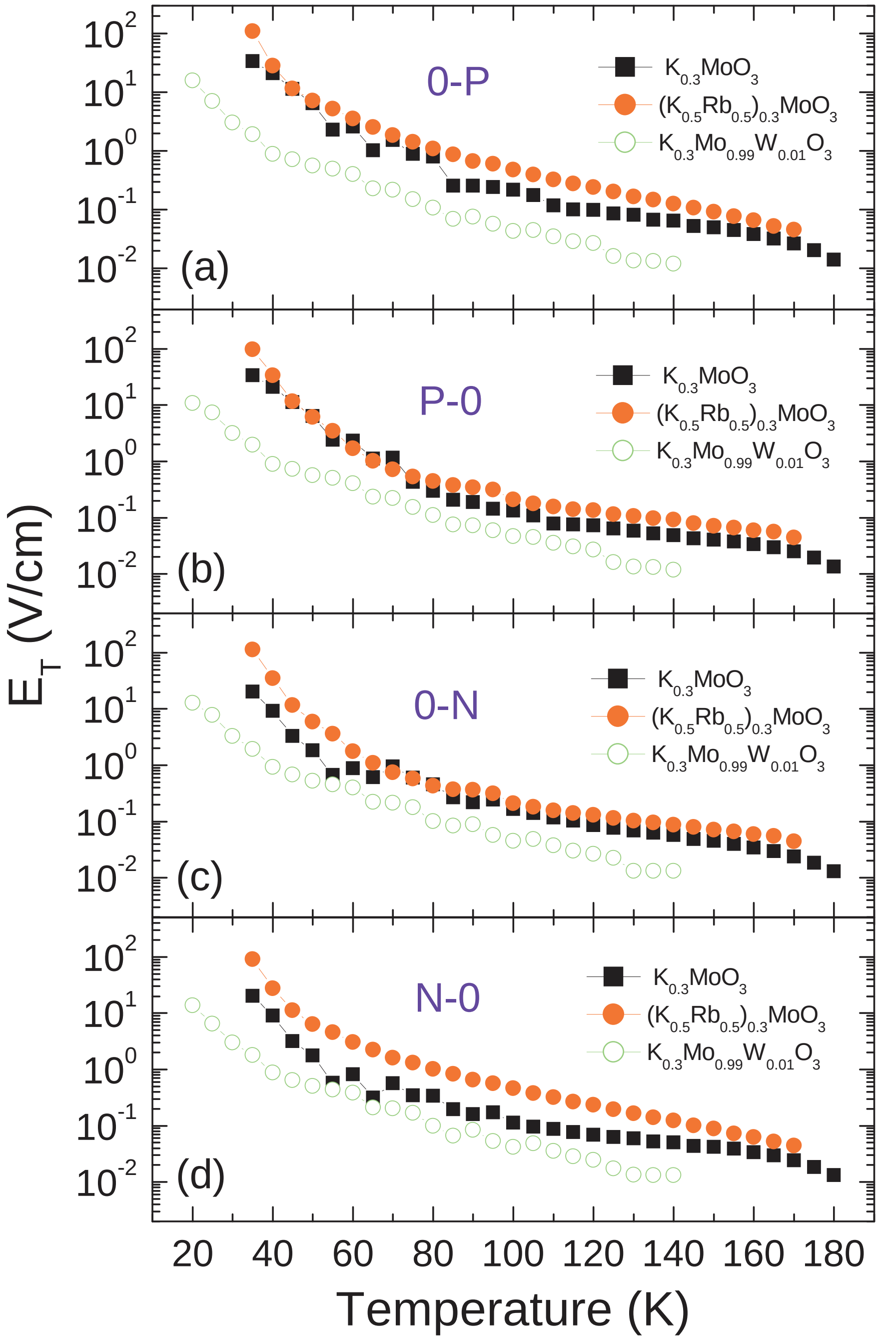

Figure 4.20: The temperature dependence of the first threshold field for the four paths separately of all studied samples.

shown in Fig. 4.23(b).

- $E_T{}^*$ of the W-doped blue bronze sample is path-independent at all temperatures except at 20 K, where there might be some path dependence as shown in

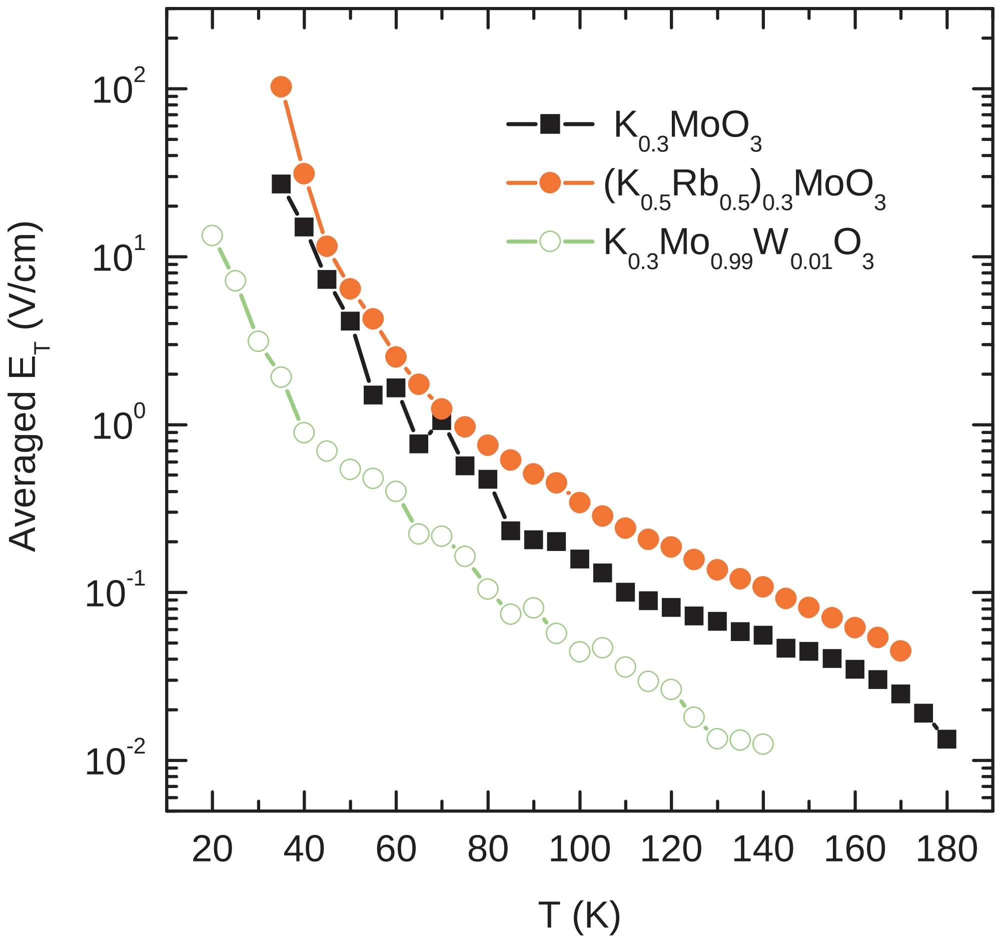

Figure 4.21: The average value of the first threshold field versus temperature of all studied samples.

Fig. 4.23(c).

- $E_T{}^*$ of the pure and Rb-doped blue bronze samples takes place at 65 K. While it takes place at 45 K for the W-doped blue bronze sample as shown Figs. 4.23(a), 4.23(b), 4.23(c).

Also it is obvious from Fig. 4.23 that $E_T{}^*(T)$ of all studied samples seems to be path-dependent. So we have plotted the average value of $E_T{}^*$ versus temperature as shown in Fig. 4.24, where:

$$AveragedE_T^* = (E_T^*(N-0) + E_T^*(0-P) + E_T^*(P-0) + E_T^*(0-N))/4 \qquad (4.5)$$

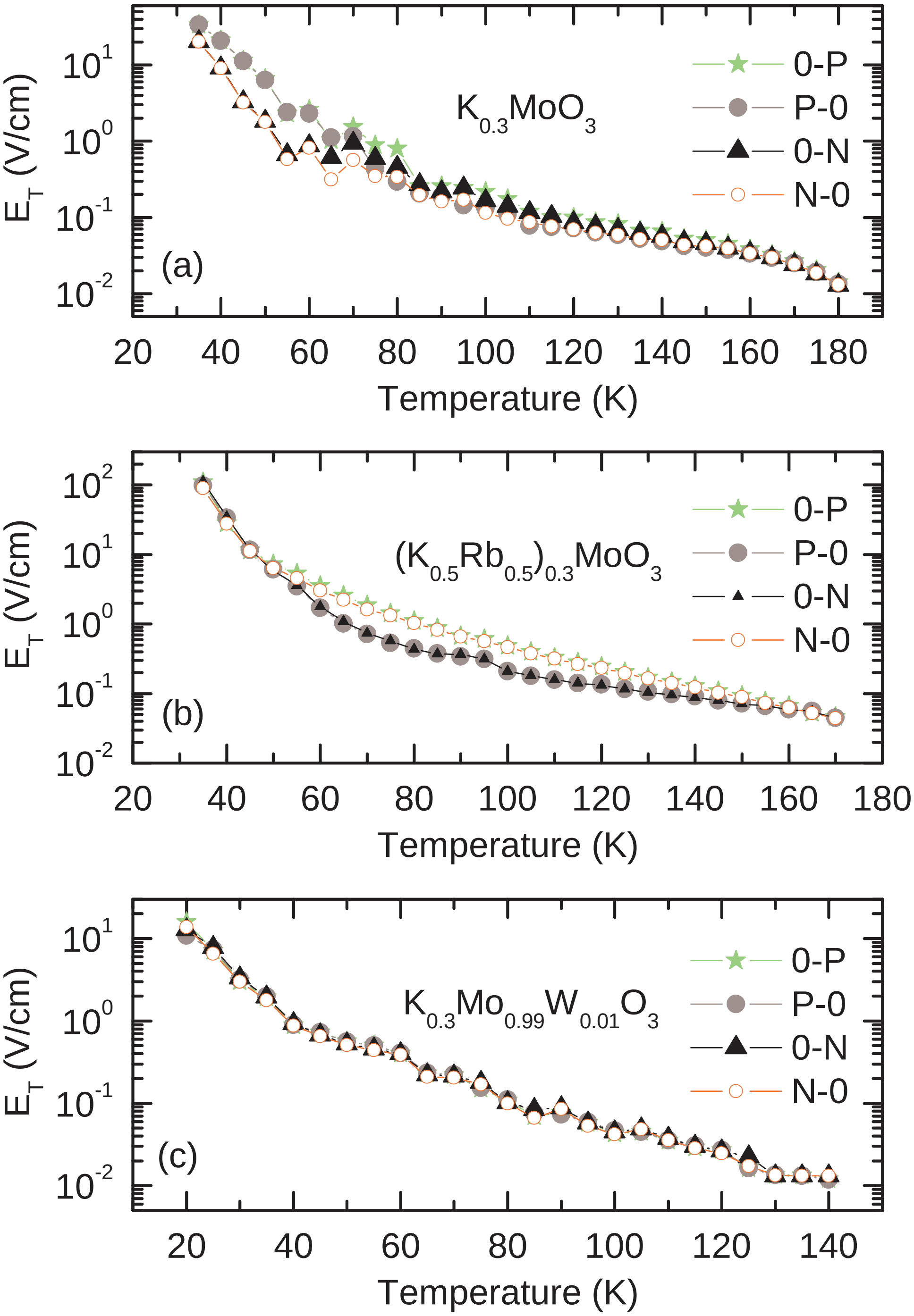

Figure 4.22: The temperature dependence of the first threshold field for the four paths together of all studied samples.

It is obvious from Fig. 4.24 that the averaged $E_T{}^*$ of all studied samples still increases monotonically with cooling down. Also the absolute values of the threshold field are

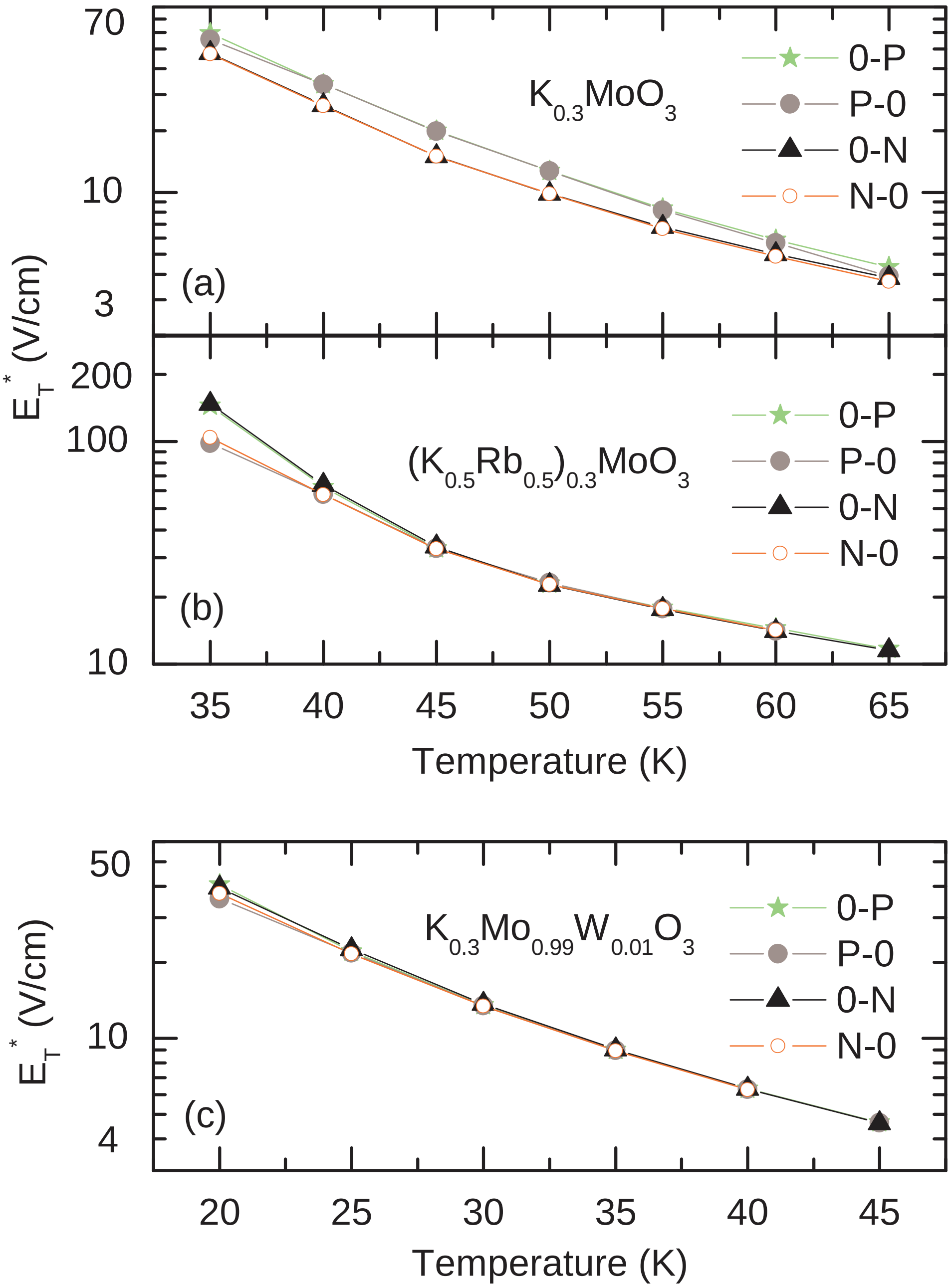

Figure 4.23: The temperature dependence of the second threshold field for the four paths together of all studied samples.

the highest in the Rb-doped blue bronze sample and the lowest in the W-doped blue bronze sample over the whole temperature range.

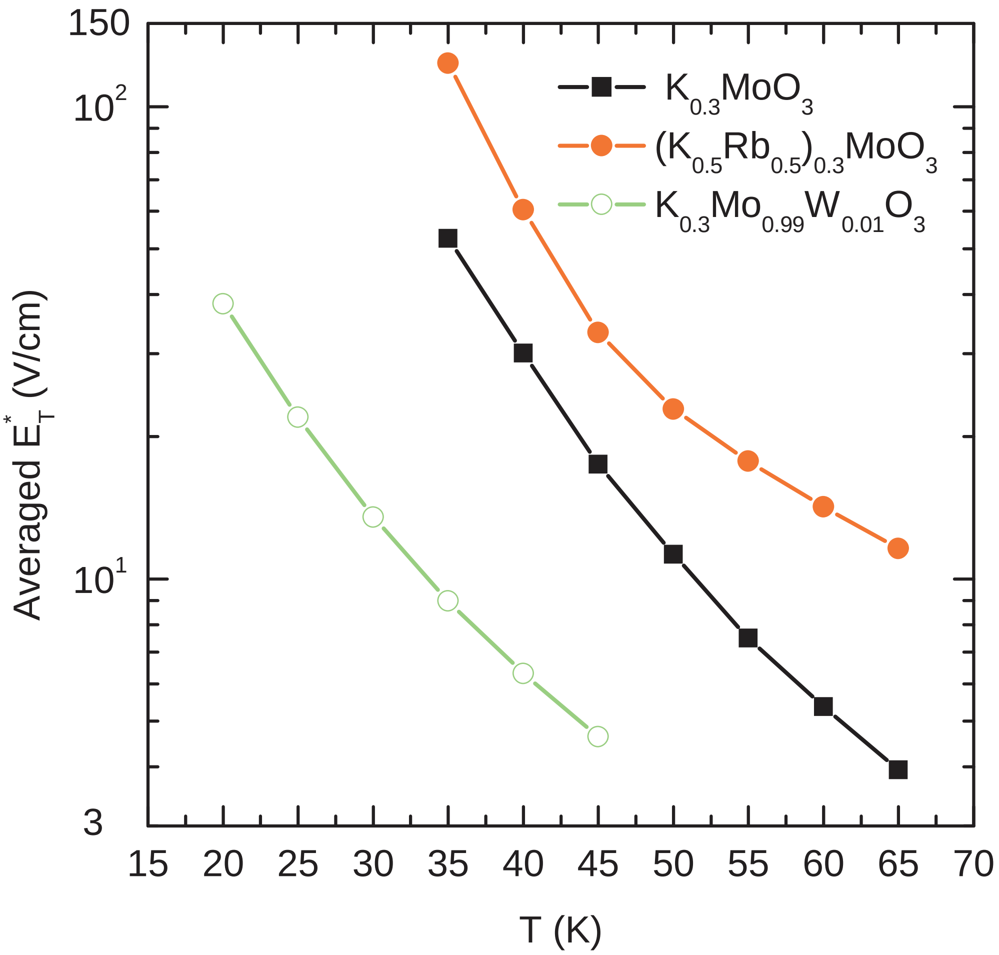

Figure 4.24: The average value of the second threshold field versus temperature of all studied samples.

4.3.4 Hysteresis in the I-V curves

According to Fig. 4.14, there is some hysteresis (two gaps between the green and red curves). This hysteresis is temperature-dependent, the reason why we have extracted the temperature dependence. For a quantification of the temperature dependence of the hysteresis, we have integrated the areas under the two curves at each temperature and then subtracting the two areas from each other to get the value of the hysteresis in Watt as a power value. Fig. 4.25 depicts the temperature dependence of the hysteresis for all studied samples for the positive and negative branches. The positive and negative branches are illustrated in Fig. 4.14. The positive branch includes the hysteresis between paths 0-P and P-0. While the negative branch includes the hysteresis between paths N-0 and 0-N.

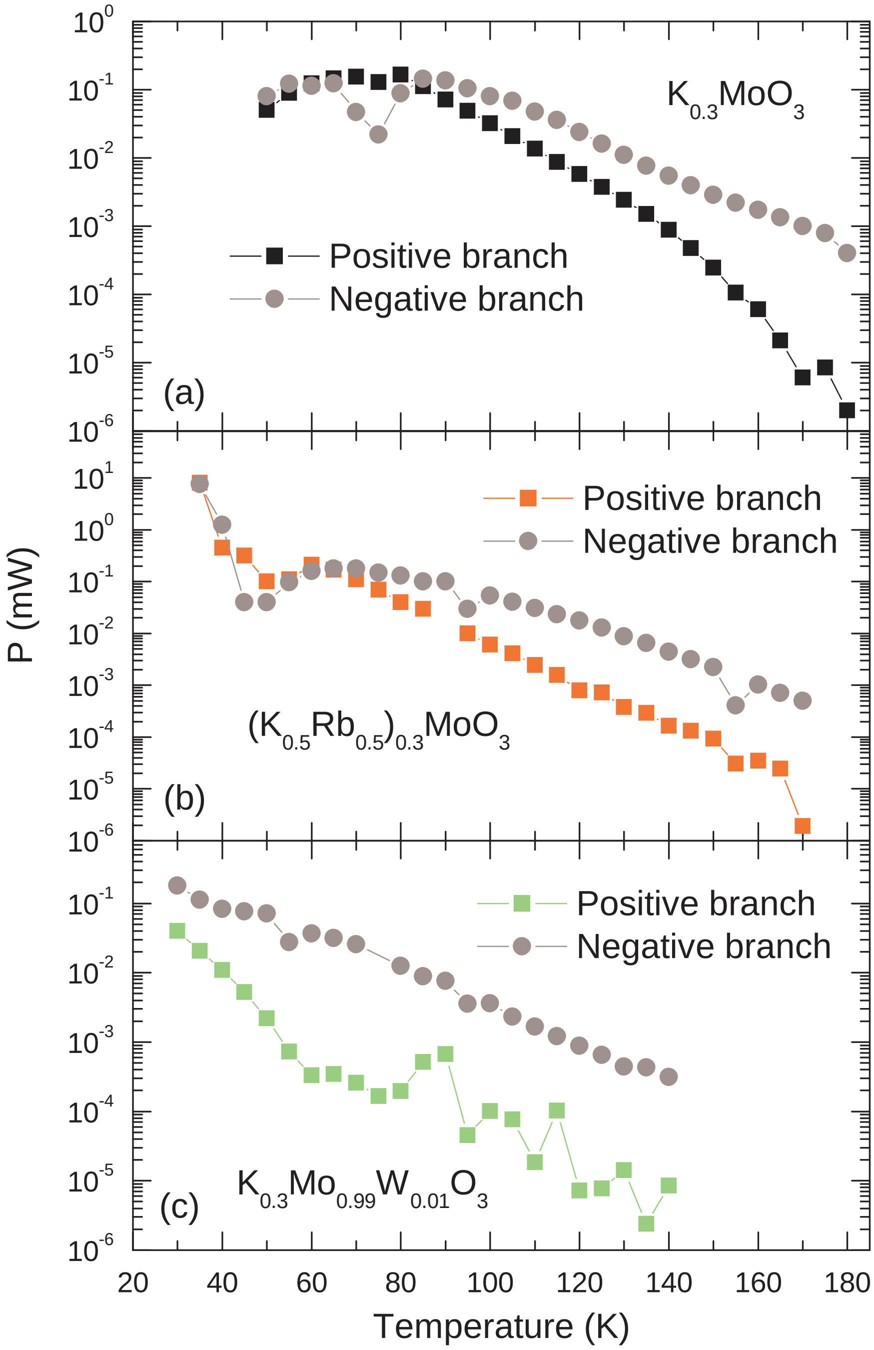

Figure 4.25: The temperature dependence of the hysteresis in the I-V curves of all studied samples.

4.3.5 Hysteresis in the temperature dependence of the resistivity

We have observed some hysteresis in the resistivity while cooling down and warming up in the pure and Rb-doped blue bronze samples. No hysteresis has been observed in the W-doped blue bronze sample, as shown in Fig. 4.26.

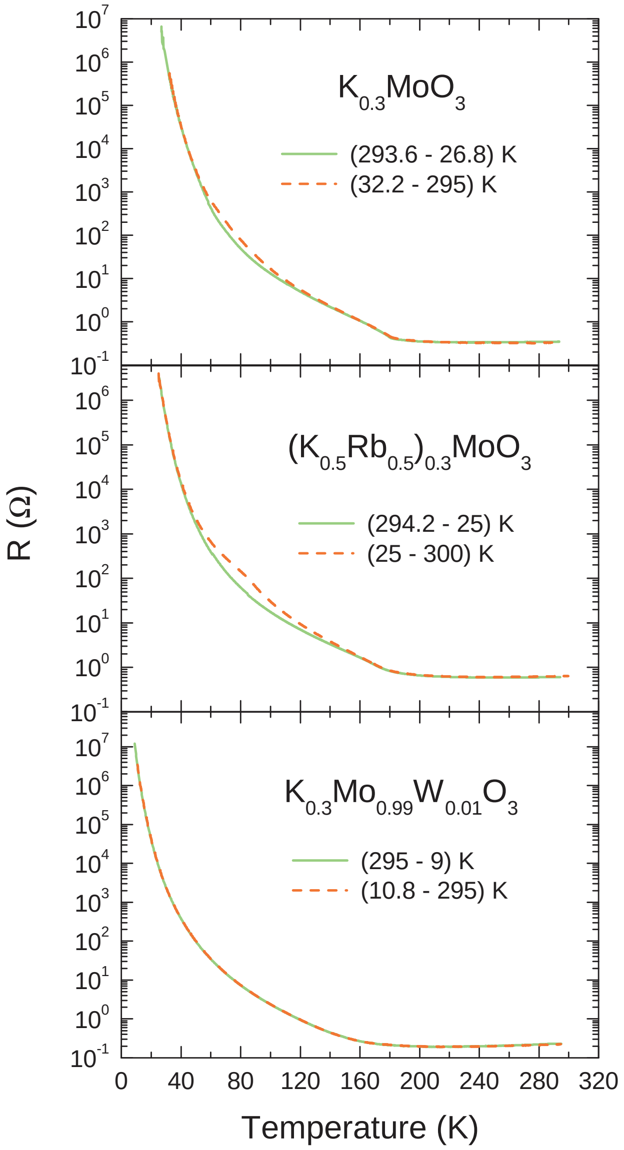

Figure 4.26: The temperature dependence of the resistivity while cooling down and warming up in all studied samples.

4.3.6 Field-dependent dc conductivity

To illustrate the contribution of the CDW cliding to the dc conductivity σ, we have plotted in Figs. 4.27, 4.28, and 4.29 σ as a function of electric field for the pure, Rb-doped, and W-doped blue bronze samples respectively. The conductivity remains constant until the electric field exceeds E_T and then the conductivity starts to increase due to the CDW sliding. A huge increase of the conductivity appears when the electric field exceeds $E_T{}^*$. It is important to mention here that the contribution of the CDW sliding appears when $T \leq T_P$. It starts to increase when $T \leq 180$ K for the pure blue bronze sample, when $T \leq 170$ K for the Rb-doped blue bronze sample and finally when $T \leq 140$ K for the W-doped blue bronze sample (see the insents of Figs. 4.27, 4.28, and 4.29). We have shown the electric field-dependent conductivity only for the 0-P path. The electric field-dependent conductivities of the other paths have shown the same behavior.

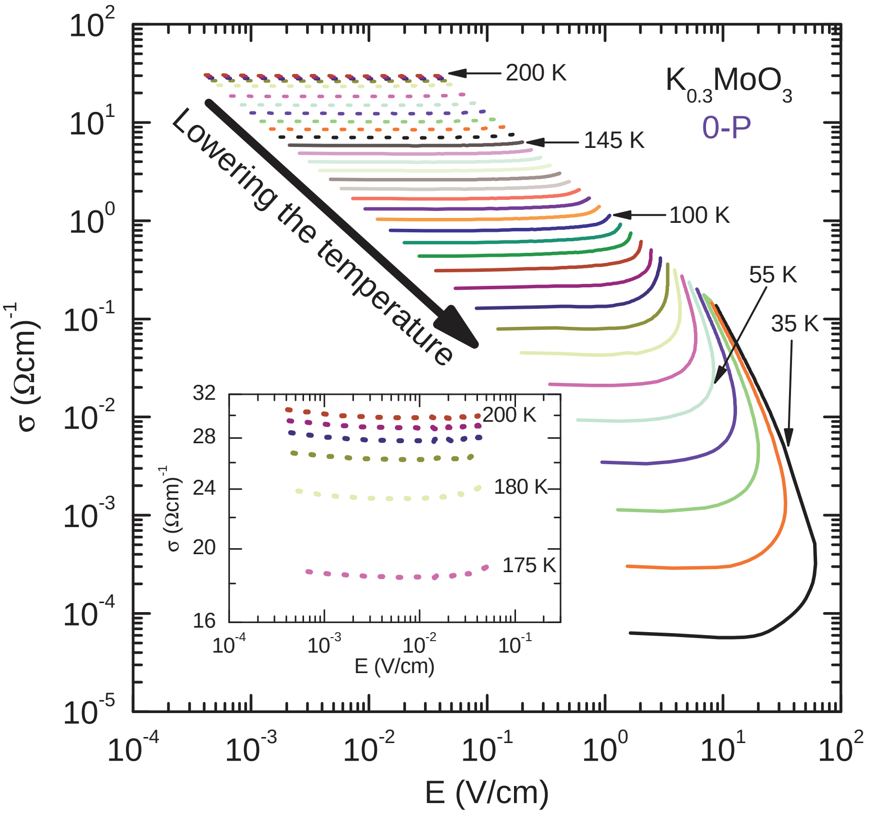

Figure 4.27: The electric field-dependent conductivity at different temperatures of $K_{0.3}MoO_3$ for the 0-P path.

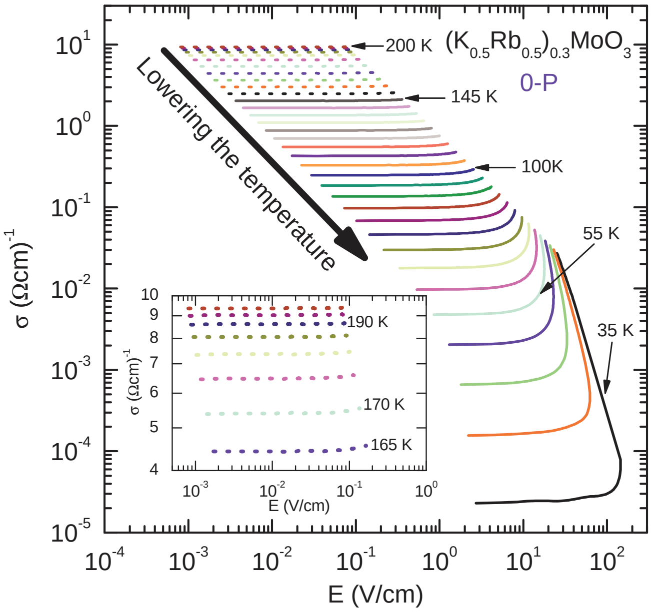

Figure 4.28: The electric field-dependent conductivity at different temperatures of $(K_{0.5}Rb_{0.5})_{0.3}MoO_3$ for the 0-P path.

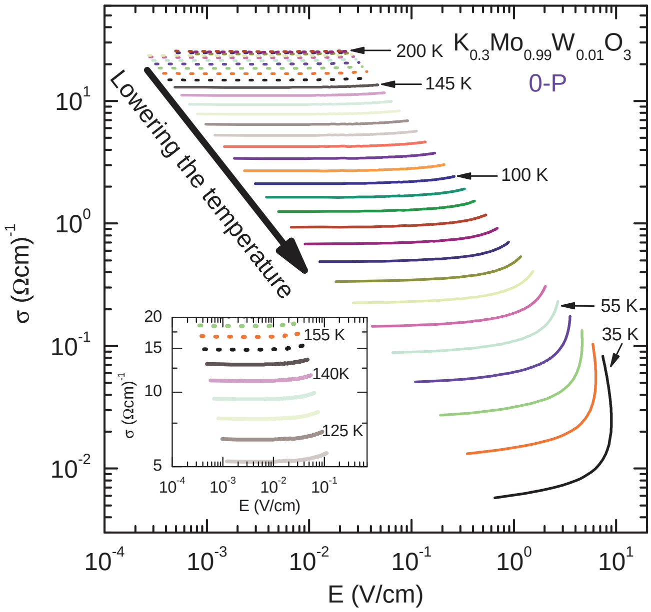

Figure 4.29: The electric field-dependent conductivity at different temperatures of $K_{0.3}Mo_{0.99}W_{0.01}O_3$ for the 0-P path.

4.3.7 Determination of CDW and normal carriers contributions as a function of temperature

To illustrate the CDW and normal carriers contributions as a function of temperature, we have extracted first the total current as a function of temperature from Fig. 4.30.

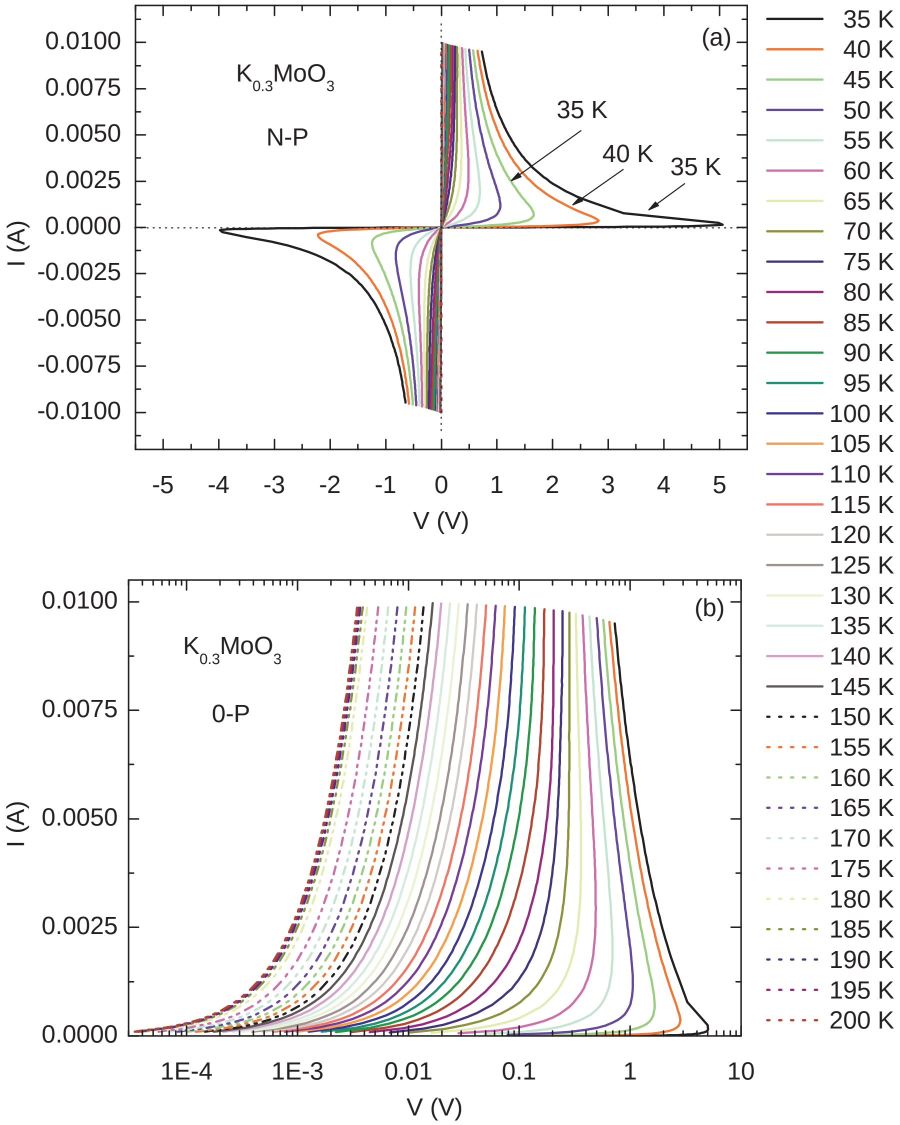

Figure 4.30: (a) The I-V curves of the pure blue bronze sample at all temperatures for the N-0 and 0-P paths. (b) The I-V curves of the pure blue bronze sample at all temperatures for the 0-P path only.

Fig. 4.30(a) plots the I-V curves of the pure blue bronze sample at all temperatures for the N-0 and 0-P paths, while Fig. 4.30(b) illustrates the 0-P path only. Since we have applied the same voltage range to all samples as mentioned before, so the maximum current (I_T) which corresponds to the maximum applied voltage has been extracted for all paths and at all temperatures, noticing that the second threshold field is already taking place. Fig. 4.31(a) illustrates $I_T(T)$ of the pure blue bronze sample for all paths together. It is clear from the figure that I_T decreases with lowering the temperature.

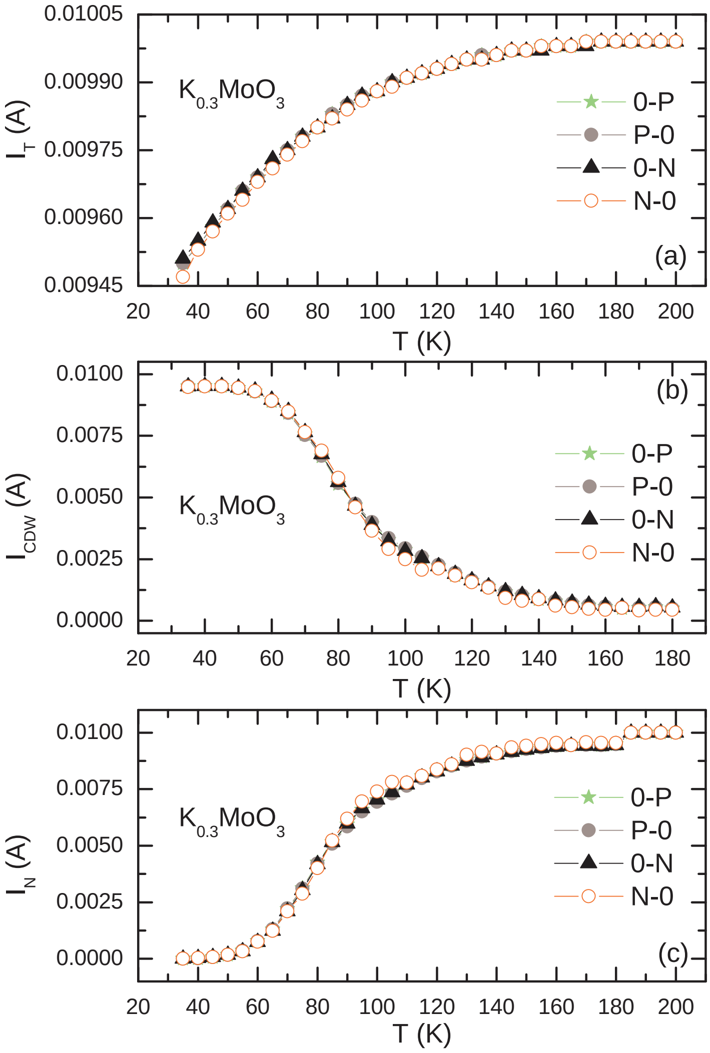

Figure 4.31: The temperature dependence of I_T, I_{CDW}, and I_N of the pure blue bronze sample for all paths together.

The same procedure has been applied to extract the temperature dependence of the CDW current [$I_{CDW}(T)$] of the pure blue bronze sample from Fig. 4.18, where $\Delta(I)$ represents the CDW current. Fig. 4.31(b) illustrates $I_{CDW}(T)$ of the pure blue bronze sample for all paths together. It is obvious from the figure that I_{CDW} increases with lowering the temperature. To illustrate the temperature dependence of the normal carriers current I_N(T), we have subtracted I_T(T) from I_{CDW}(T). Fig. 4.31(c) plots I_N(T) of the pure blue bronze sample for all paths together. It is clear from the figure that I_N decreases with lowering the temperature. Fig. 4.32 plots I_T(T), I_N(T), and I_T(T) of $K_{0.3}MoO_3$ for all paths separately.

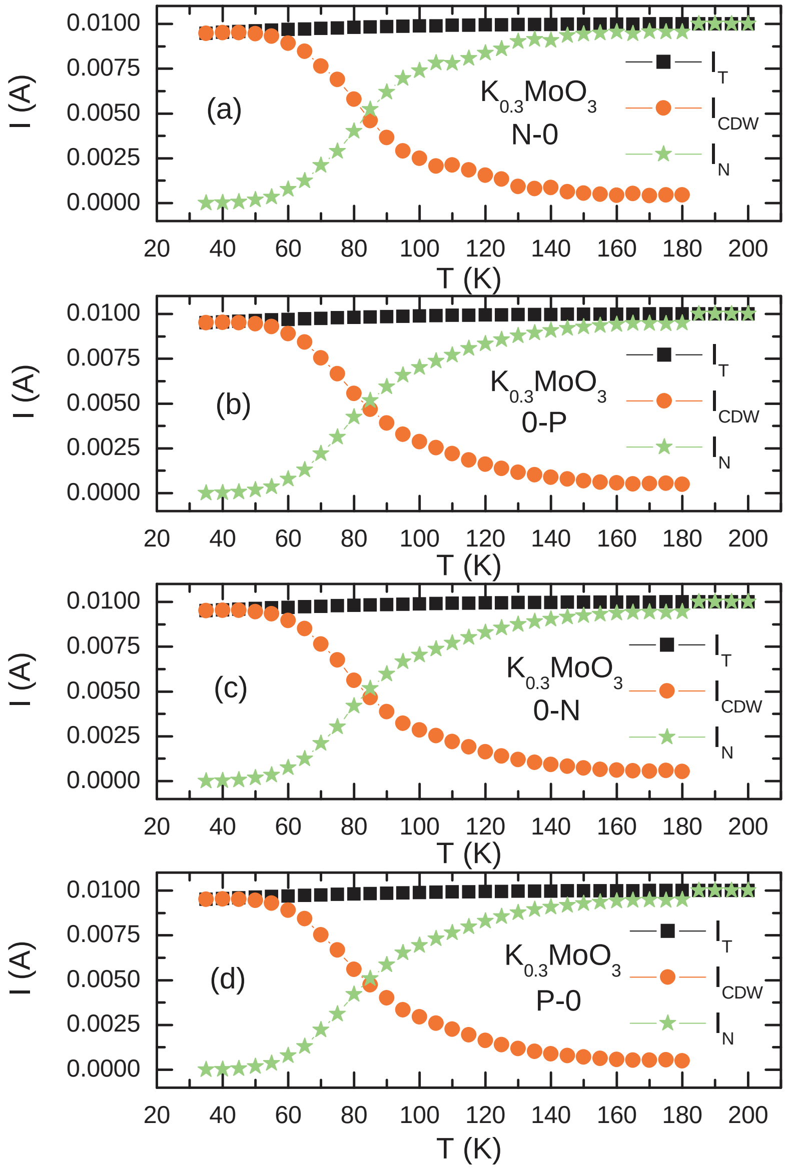

Figure 4.32: The temperature dependence of I_T, I_{CDW}, and I_N of the pure blue bronze sample for all paths separately.

The same procedure has been applied again to extract I_T(T), I_N(T), and I_T(T) of the Rb-doped blue bronze sample. Fig. 4.33(a) illustrates I$_T$(T) of the Rb-doped blue bronze sample for all paths together. It is clear from the figure that I$_T$ decreases with lowering the temperature. Fig. 4.33(b) illustrates I$_{CDW}$(T) of the Rb-doped blue bronze sample for all paths together. It is obvious from the figure that I$_{CDW}$ increases with lowering the temperature. Fig. 4.33(c) plots I$_N$(T) of the Rb-doped blue bronze sample for all paths together. It is clear from the figure that I$_N$ decreases with lowering the temperature.

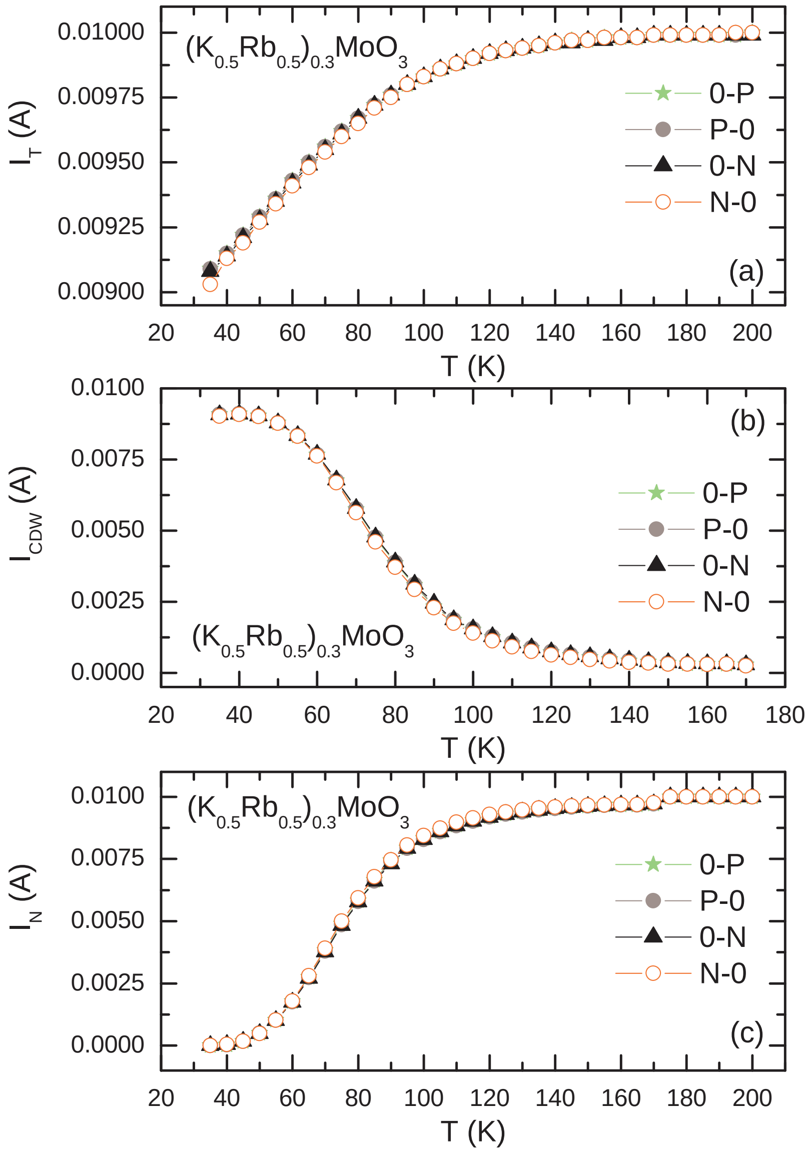

Figure 4.33: The temperature dependence of I$_T$, I$_{CDW}$, and I$_N$ of the Rb-doped blue bronze sample for all paths together.

Fig. 4.34 plots $I_T(T)$, $I_N(T)$, and $I_T(T)$ of the Rb-doped blue bronze sample for all paths separately.

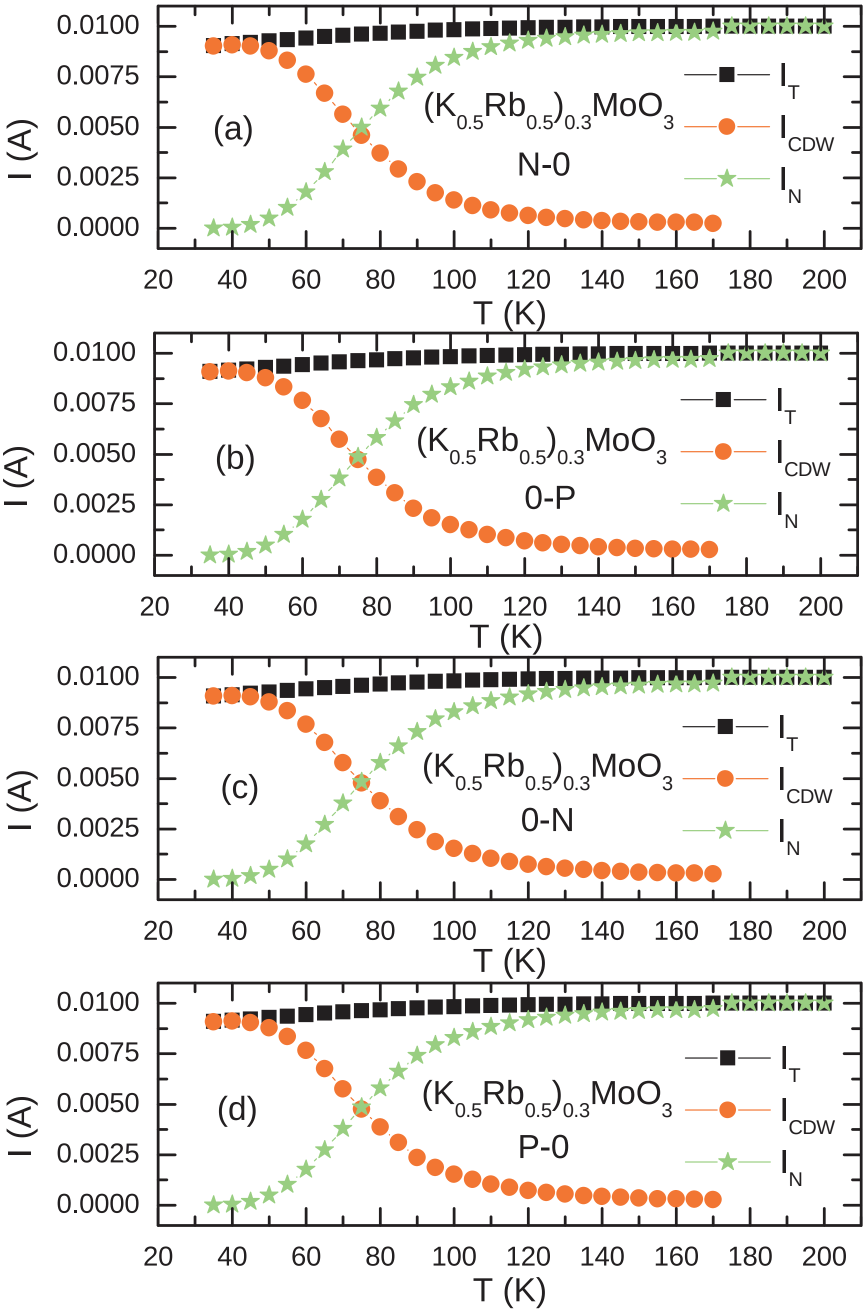

Figure 4.34: The temperature dependence of I_T, I_{CDW}, and I_N of the Rb-doped blue bronze sample for all paths separately.

The same procedure has been applied once again to extract $I_T(T)$, $I_N(T)$, and $I_T(T)$ of the W-doped blue bronze sample. Fig. 4.35(a) illustrates $I_T(T)$ of the W-doped blue bronze sample for all paths together. It is clear from the figure that I_T decreases with lowering the temperature. Fig. 4.35(b) illustrates $I_{CDW}(T)$ of the W-doped blue bronze sample for all paths together. It is obvious from the figure that I_{CDW} increases with lowering the temperature. Fig. 4.35(c) plots $I_N(T)$ of the W-doped blue bronze sample for all paths together. It is clear from the figure that I_N decreases with lowering the temperature.

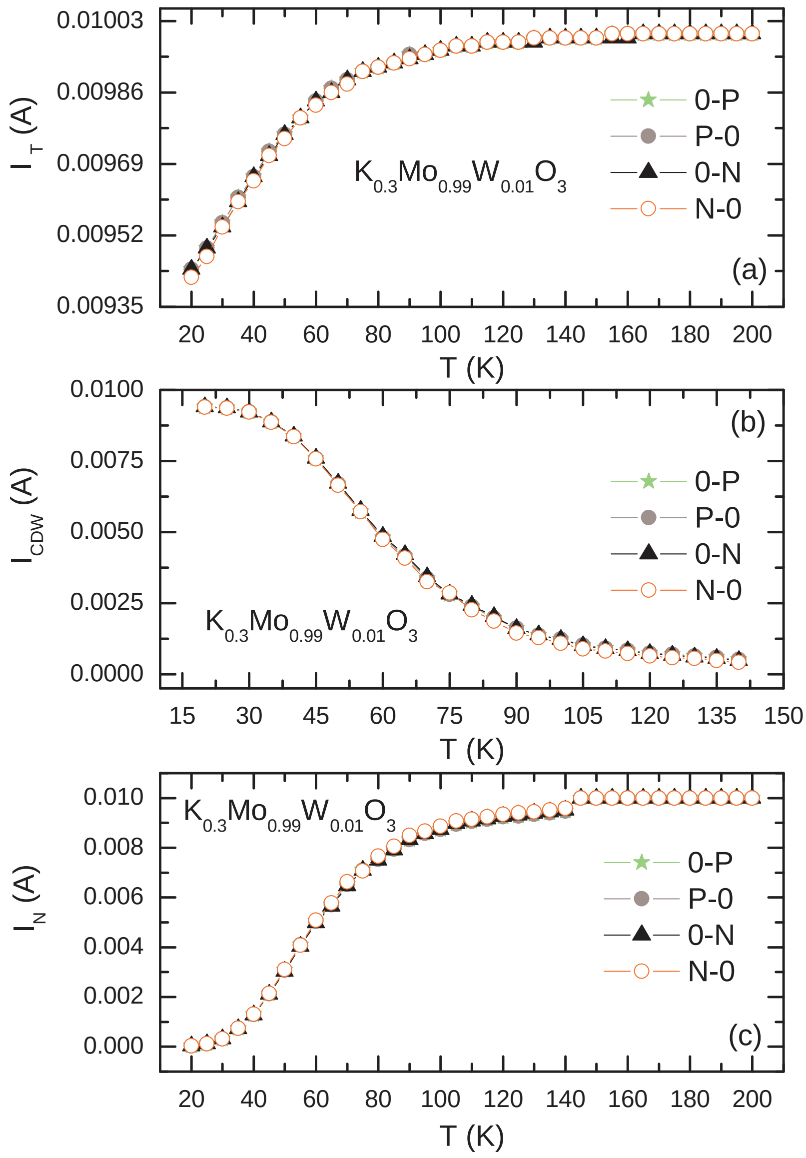

Figure 4.35: The temperature dependence of I_T, I_{CDW}, and I_N of the W-doped blue bronze sample for all paths together.

Fig. 4.36 plots $I_T(T)$, $I_N(T)$, and $I_T(T)$ of the W-doped blue bronze sample for all paths separately.

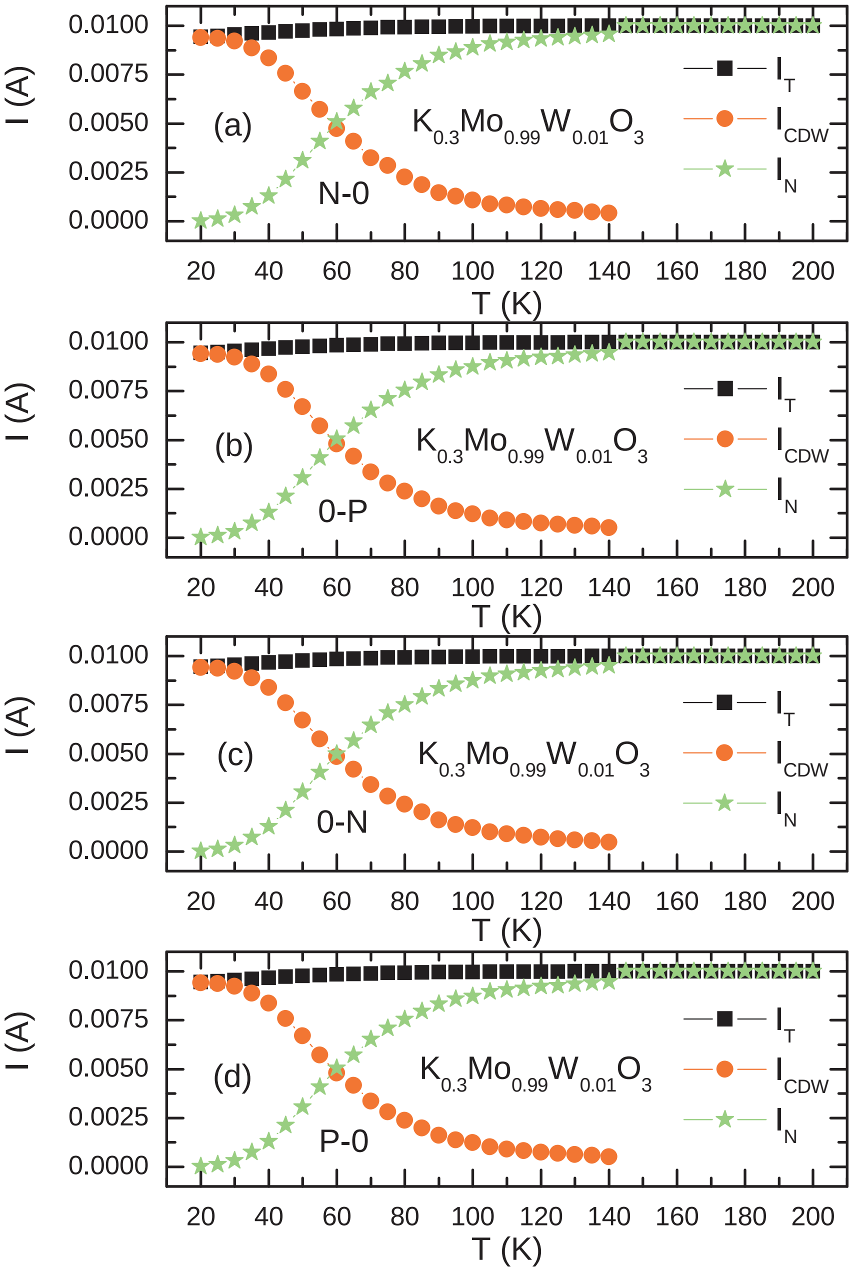

Figure 4.36: The temperature dependence of I_T, I_{CDW}, and I_N of the W-doped blue bronze sample for all paths separately.

Fig. 4.37 illustrates I_{CDW}(T) of all studied samples for all paths separately. It is obvious from the figure that the absolute values of I_{CDW} of the pure blue bronze sample are the highest, while the absolute values of I_{CDW} of the W-doped blue bronze sample are the lowest over some temperature range.

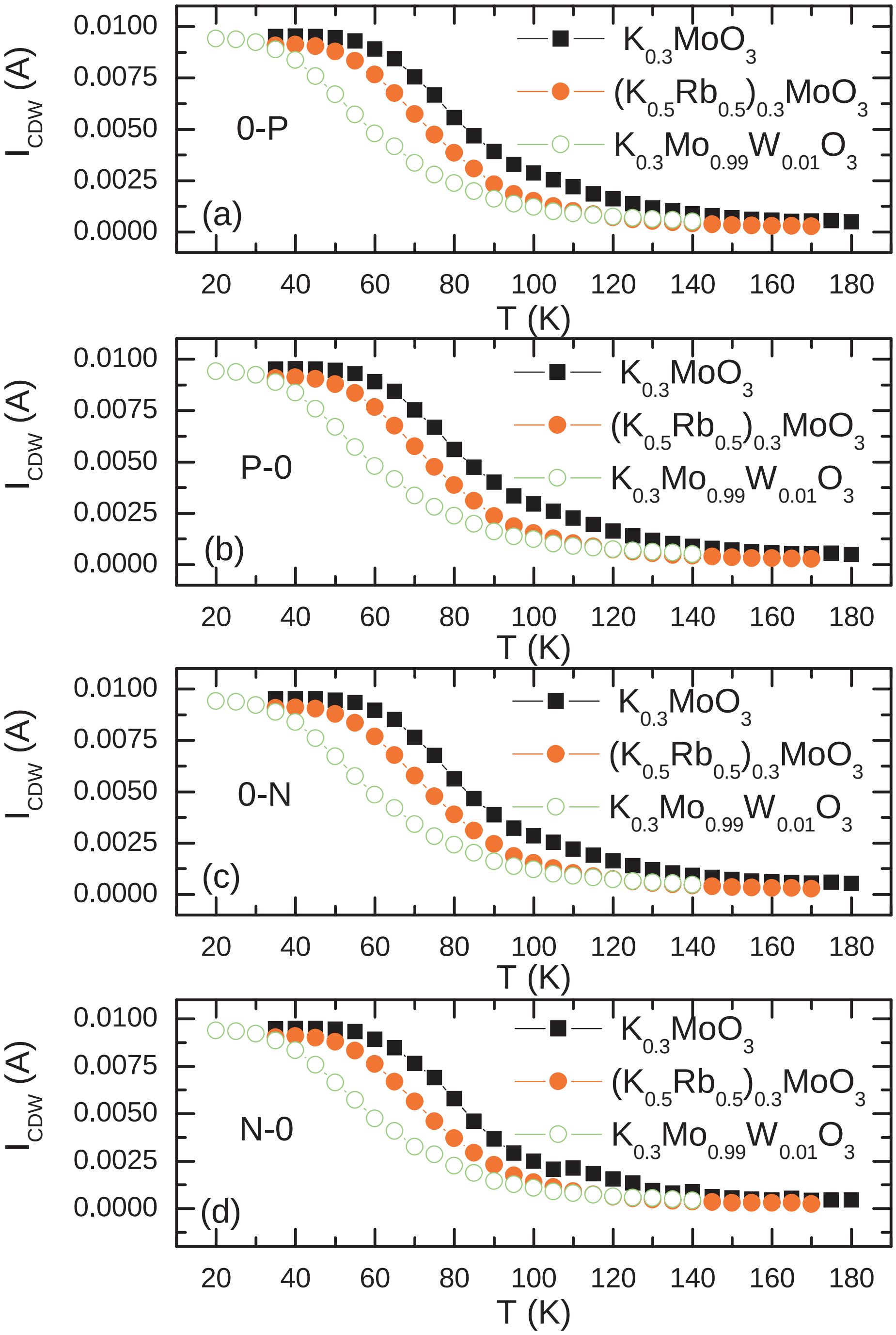

Figure 4.37: The temperature dependence of I_{CDW} of all studied samples for all paths separately.

Fig. 4.38 illustrates $I_N(T)$ of all studied samples for all paths separately. It is obvious from the figure that the absolute values of I_N of the pure blue bronze sample are the lowest, while the absolute values of I_N of the W-doped blue bronze sample are the highest over some temperature range.

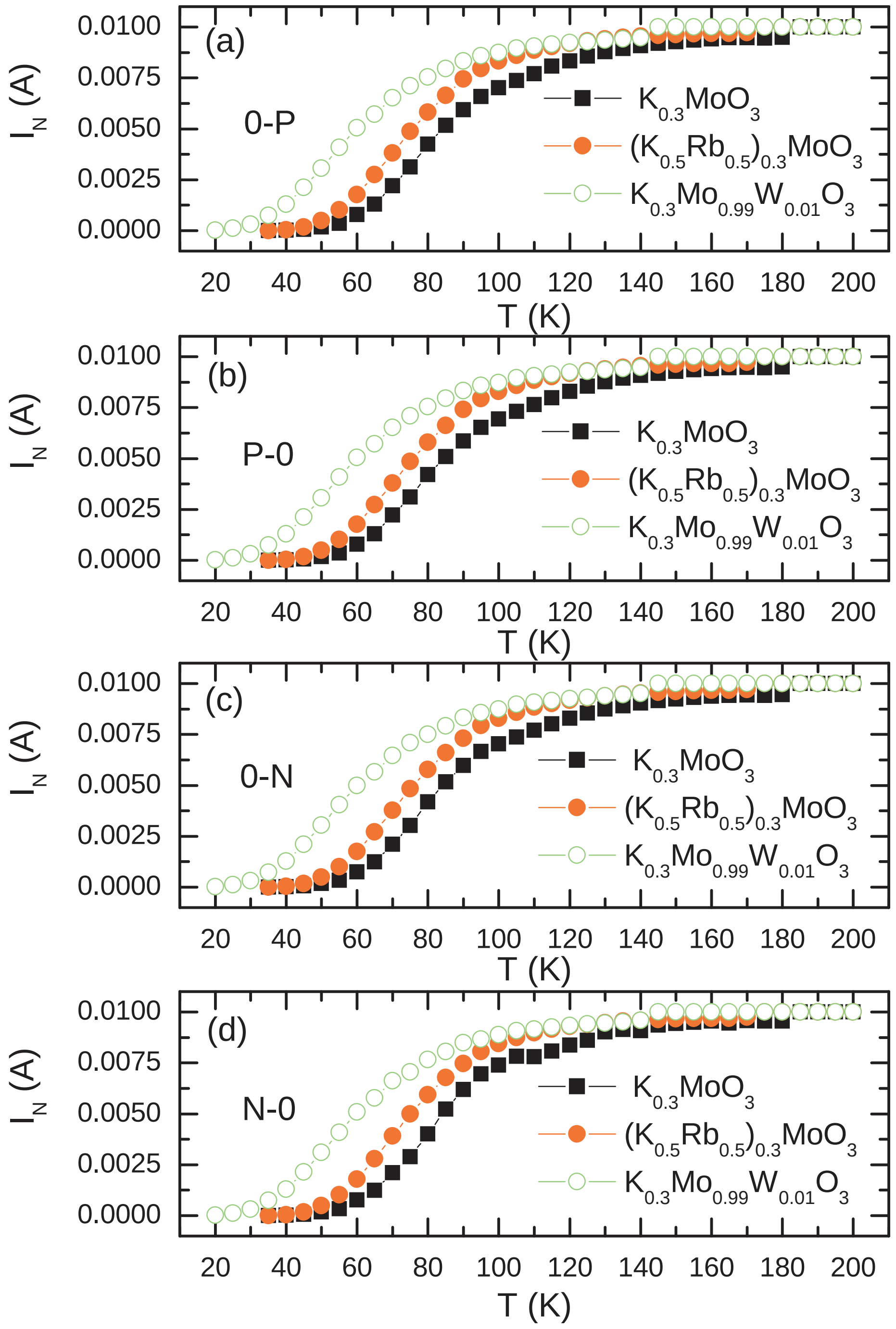

Figure 4.38: The temperature dependence of I_N of all studied samples for all paths separately.

Fig. 4.39 illustrates $I_T(T)$ of all studied samples for all paths separately. It is obvious from the figure that the absolute values of I_T of the Rb-doped blue bronze sample are the lowest, while the absolute values of I_T of the W-doped blue bronze sample are the highest over some temperature range.

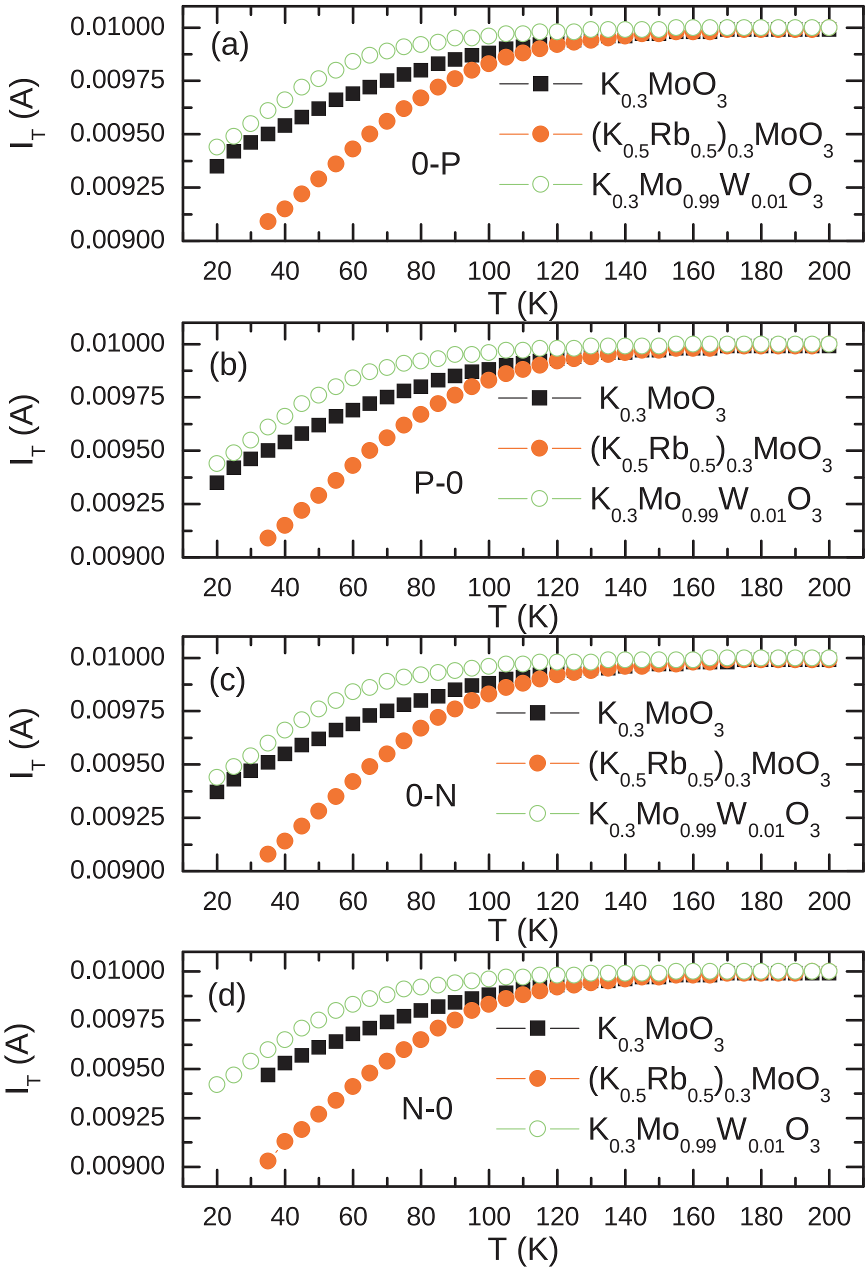

Figure 4.39: The temperature dependence of I_T of all studied samples for all paths separately.

4.3.8 Liquid N_2 dc transport measurements

All dc measurements and some of the analysis mentioned above have been performed twice; once using the liquid N_2 dc setup and once again using the liquid He dc setup. The results of both setups have been more or less similar in the liquid N_2 temperature range as shown in Fig. 4.40, as an example.

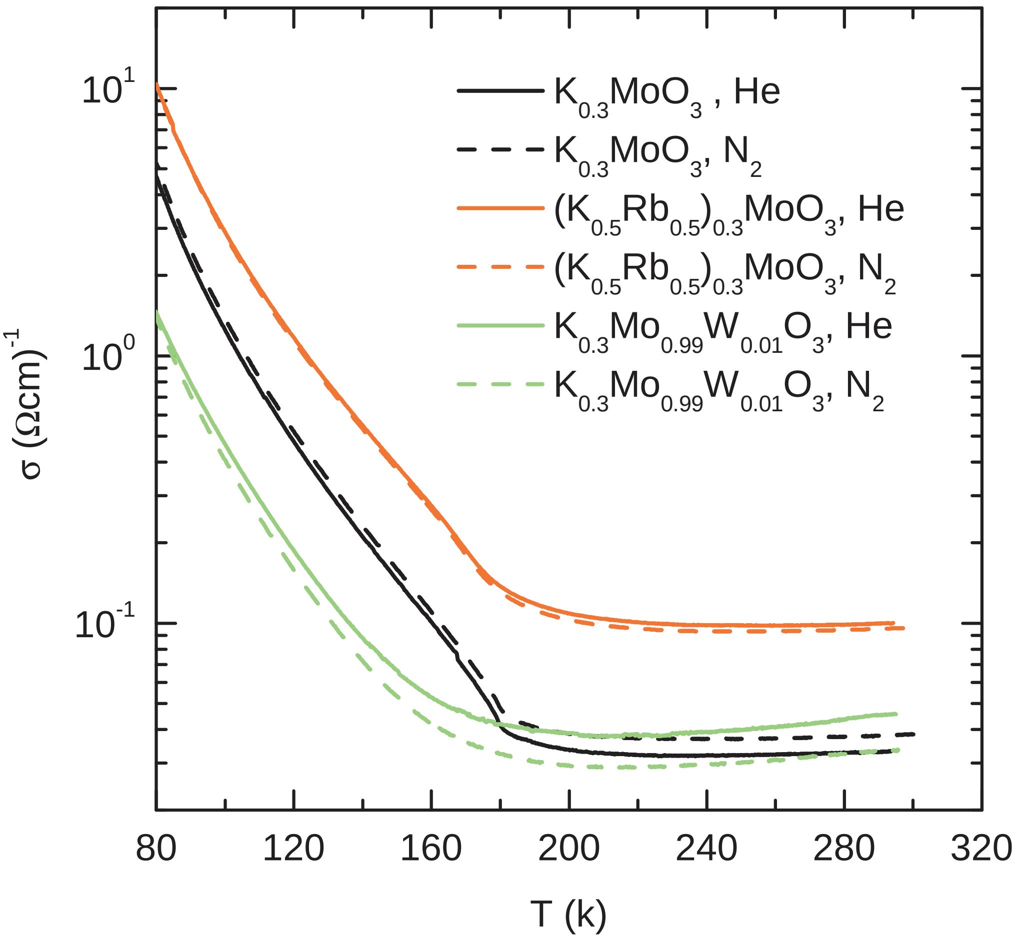

Figure 4.40: The temperature dependence of the specific resistivity using liquid N_2 and liquid He.

4.4 Infrared measurements

4.4.1 Room temperature infrared measurements

The reflectivity along the chain direction and perpendicular to it of a large single crystal of $K_{0.3}MoO_3$ has been measured in the MIR range (625 cm^{-1} - 8000 cm^{-1}) using linearly polarized light. These measurements have been performed at room temperature using the free standing technique explained in chapter 3. The reflectivity spectra along b and perpendicular to it measured using the free standing technique have been always considered as the reference MIR optical reflectivity spectra of the pure blue bronze.

The optical reflectivity of the same sample has been again measured at room temperature in the same frequency range using the reflection unit along with the cold finger cryostat, explained in the experiments chapter. These measurements have been done also using linearly polarized light, in order to measure the optical reflectivity along the chain axis and perpendicular to it. The reflectivity spectra measured using both techniques are shown in Fig. 4.41, which are the proof that the reflection unit is aligned properly. The reflectivity spectra, measured using the reflection unit are a bit lower than that measured using the free standing technique because of the better reference (gold layer on top of the sample surface; see Sec. 3.1.2).

One notes from Fig. 4.41 that the room temperature spectrum along the chain direction (b axis) is metal-like (the reflectance is large and featureless due to the metallic character) with a plasma edge above 1 eV. This means that the pure blue bronze resembles a metal at 300 K for the polarization (P) $\parallel$ b. While the room temperature spectrum perpendicular to the chain direction is semiconductor-like (the reflectance is not large and many sharp lines are observed for photon energies less than about 0.12 eV) with an absorption edge near 0.5 eV. This means that the pure blue bronze resembles a semiconductor at 300 K for the polarization (P) $\perp$ b. This is in good agreement with previous data (see Optical studies of blue bronzes in the theory chapter).

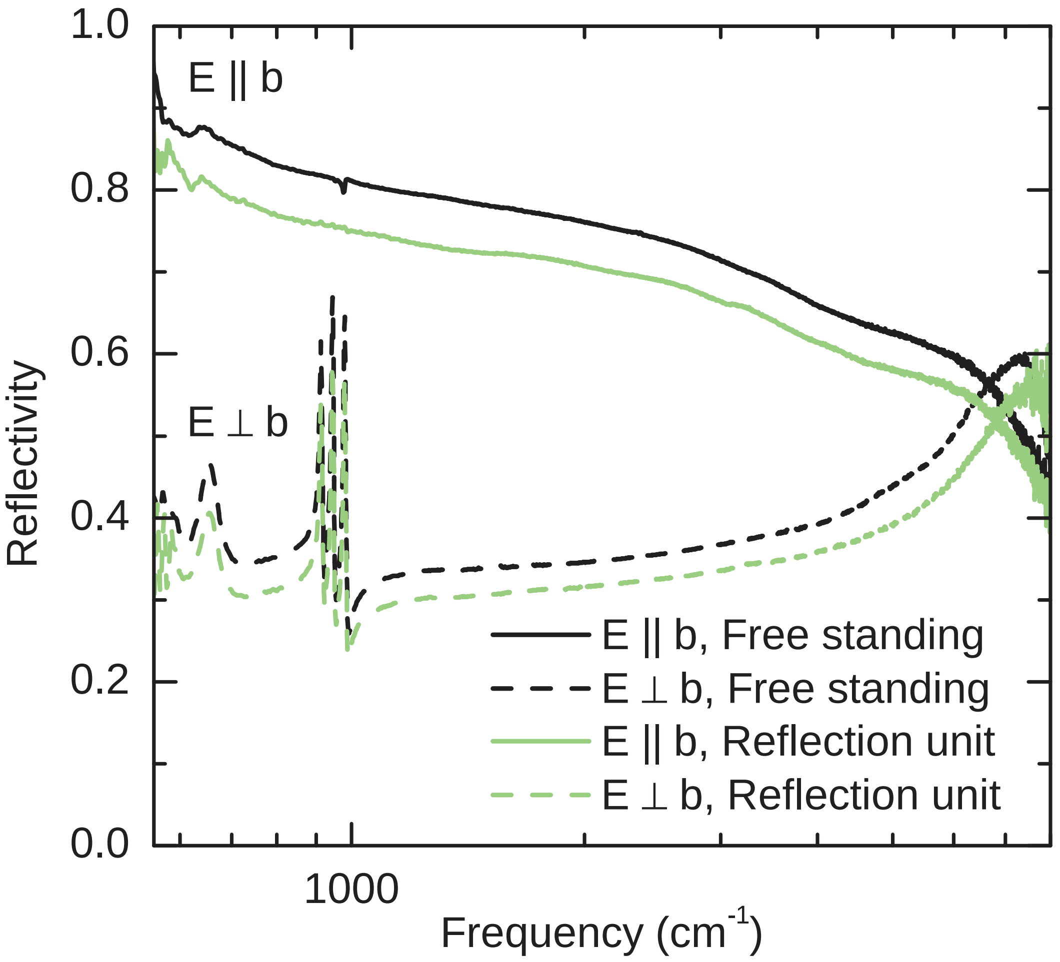

Figure 4.41: The optical reflectivity spectra parallel and perpendicular to the chain axis of a large single crystal of $K_{0.3}MoO_3$. The measurements have been done using the free standing technique and again using the reflection unit along with the cold finger cryostat explained in the experiments chapter at room temperature in the Mid-IR range.

4.4.2 Low temperature infrared measurements

The reflectivity along the chain direction and perpendicular to it of the same pure blue bronze sample mentioned in the last section has been also measured in the MIR range (625 cm^{-1} - 8000 cm^{-1}) using linearly polarized light in the temperature range (100 K-300 K). These measurements have been done using the reflection unit along with the cold finger cryostat explained in the experiments chapter. The low temperature reflectivity spectra are shown in Fig. 4.42.

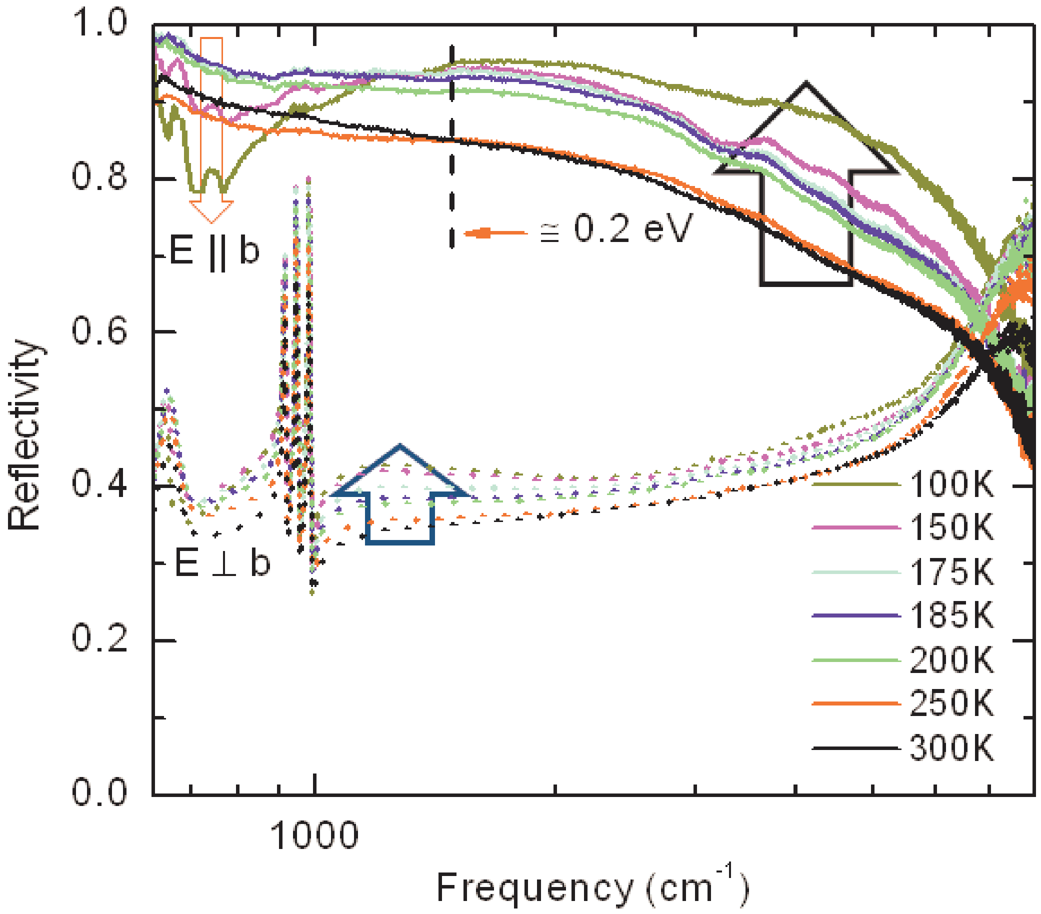

Figure 4.42: The optical reflectivity spectra parallel and perpendicular to the chain axis of a large single crystal of $K_{0.3}MoO_3$. The measurements have been done using the reflection unit along with the cold finger cryostat, explained in the experiments chapter at different temperatures in the Mid-IR range.

One sees from Fig. 4.42 the following:

- Above the Peierls transition temperature ($T_P = 180$ K) the spectral weight of the metallic spectrum (for P || b) increases with decreasing temperature, which is normal for a metal (the more the spectral weight ⟶ the more the free carriers ⟶ the more the reflectance ⟶ the less the resistance). The temperature dependence of the spectral weight is indicated by a black arrow, shown in Fig. 4.42.
- At the Peierls transition temperature the metallic spectrum along the chain axis exhibits an extreme decrease of the reflectivity below about 0.2 eV, indicating

the Peierls energy gap opening due to the charge density wave formation. This means that the metal-like reflectivity turns into a semiconductor-like spectrum. The decrease of the reflectivity is temperature-dependent and indicated by a red arrow, shown in Fig. 4.42.

- At low temperatures the spectral weight of the semiconductor spectrum (for P $\perp$ b) also increases with decreasing temperature, but hardly changes qualitatively. The temperature dependence of the spectral weight is indicated by a blue transparent arrow, shown in Fig. 4.42.

In order to see the opening of the Peierls energy band gap more clear, we did fit the optical reflectivity spectra at 300 K and 100 K measured using the reflection unit along with the cold finger cryostat (see Fig. 4.43). Then we determined the frequency dependence of the optical conductivity from the fit curves, as shown in Fig. 4.44. The gap opening due the CDW formation is clear below the Peierls transition temperature at 100 K, while a Drude behavior is obvious at room temperature.

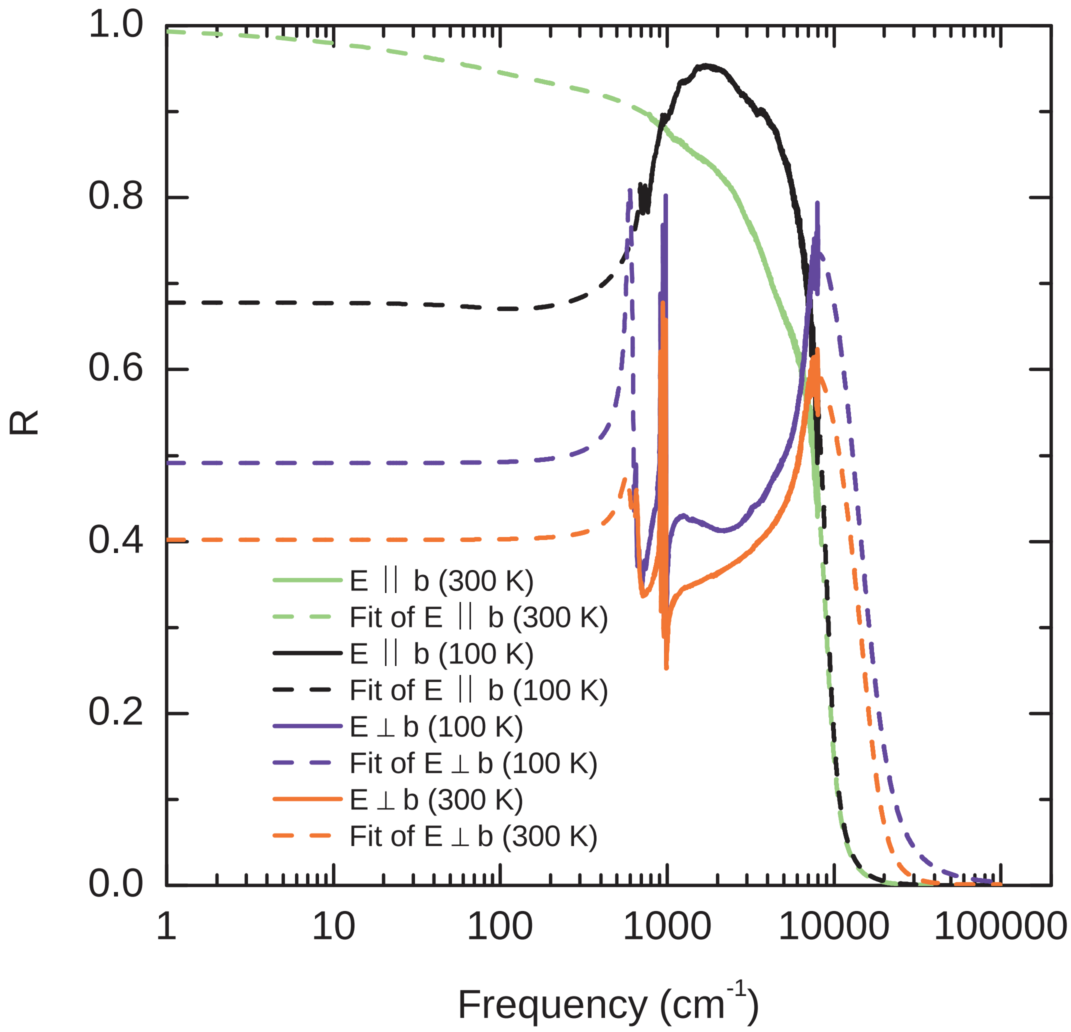

Figure 4.43: The fit curves of the optical reflectivity spectra parallel and perpendicular to the chain axis of a large single crystal of $K_{0.3}MoO_3$ at 300 K and 100 K. The figure also shows the measured reflectivity spectra in the Mid-IR range using the reflection unit along with the cold finger cryostat.

4.5 Discussion

Depending on what had been observed in our dc transport measurements, the related effects which are relevant for the CDW transport are discussed and presented in this section.

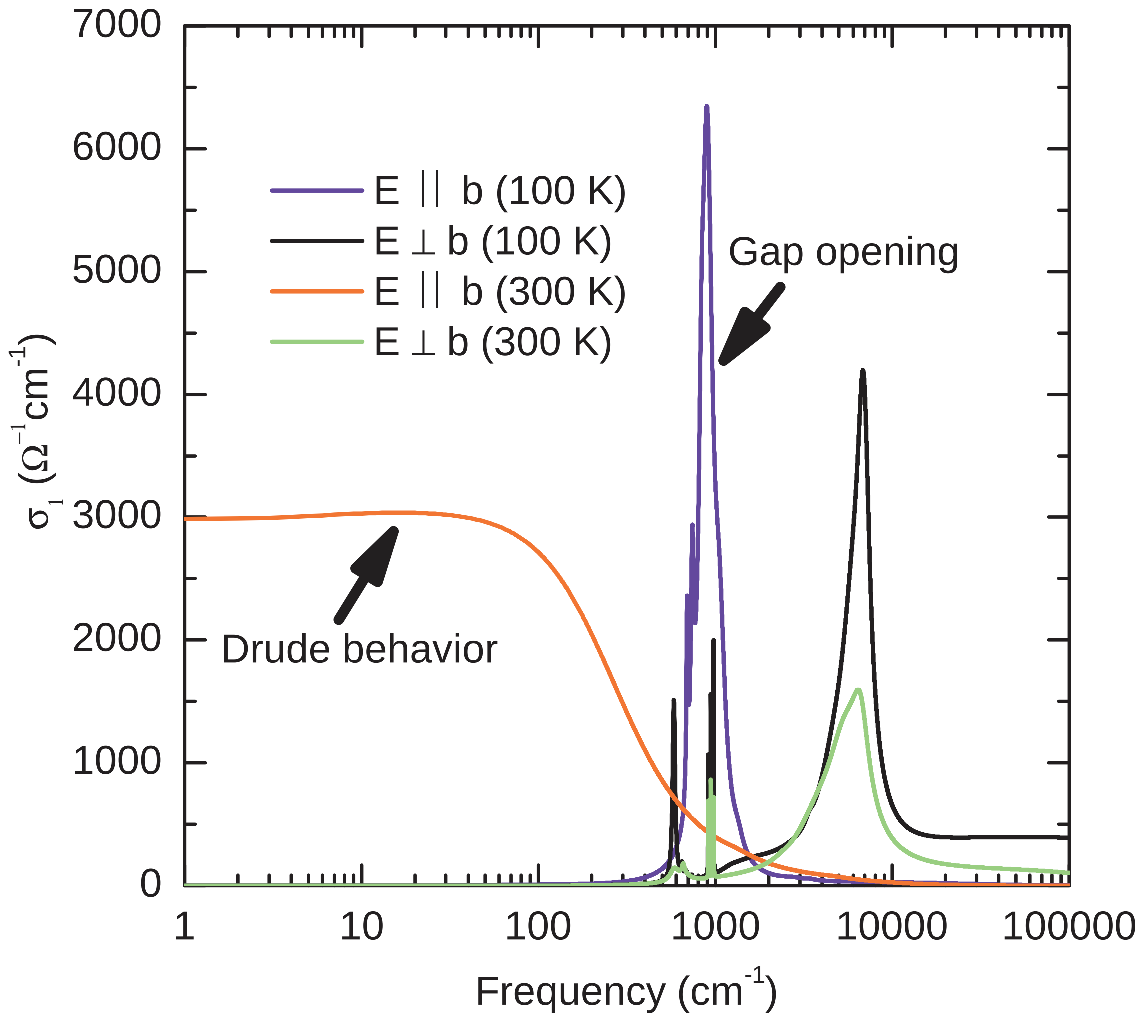

Figure 4.44: The optical conductivity spectra parallel and perpendicular to the chain axis of a large single crystal of $K_{0.3}MoO_3$ at 300 K and 100 K. The figure shows the opening of the Peierls energy band gap below the Peierls transition temperature.

4.5.1 The incommensurate-commensurate (I-C) transition of the CDW

If the wavelength of the CDW (λ_c) is commensurate with the lattice period, then the interaction between the CDW and the underlying lattice is strong. Thus the CDW is pinned to the lattice and the pinning strength due to this type of interaction is considered to be very strong. In this case very high external electric fields are required to depin the CDW. [2] As we know from Sec. 2.4.3, the CDW incommensurability is temperature dependence; the temperature dependence of the CDW incommensurability (δ) has been taken from the neutron scattering data shown in Fig. 4.45, within the resolution of the experiment, the CDW becomes less and less discommensurate with decreasing temperature (with some sort of saturation around 100 K). [55] Consequently the pinning strength due to the interaction of the CDW with the underlying lattice increases with lowering the temperature, since the CDW becomes more commensurate with the lattice period when the temperature is lowered. Within this picture the first and second threshold fields should increase with lowering the temperature, which is in good agreement with our data. Our results, regarding the temperature dependence of the second threshold field are in good agreement with some previous results taken by Zawilski et al. [79] While in the case of the temperature dependence of the first threshold field, some authors have found that E_T increases from 60 K to ~150 K [80]; others have found a plateau above 100 K or a small decrease above 100 K [55, 81]; others [82] have found a maximum near 100 K in both $K_{0.3}MoO_3$ and $Rb_{0.3}MoO_3$. [6]

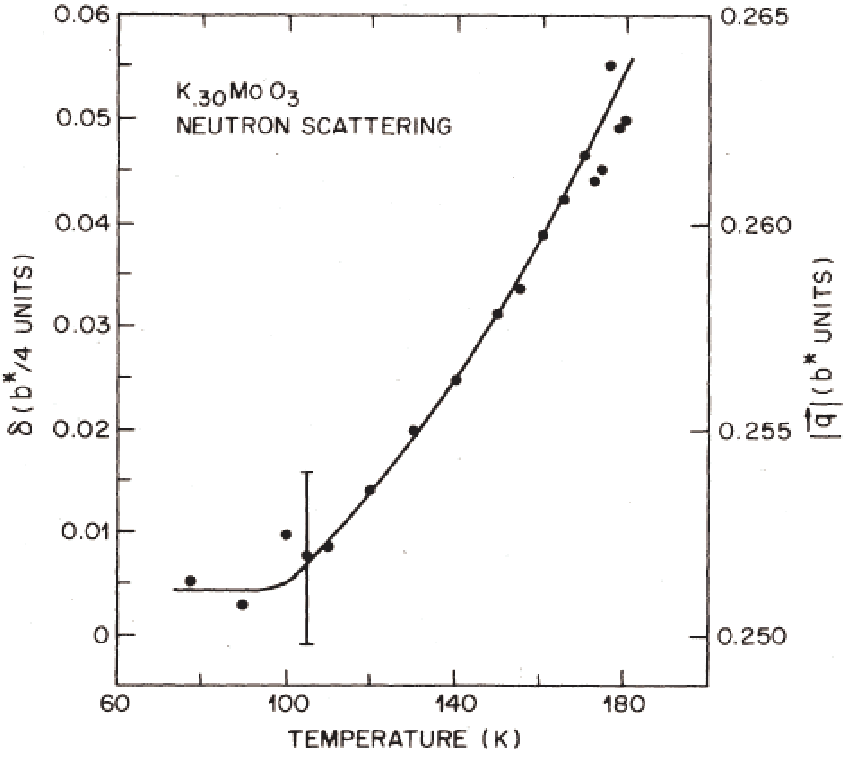

Figure 4.45: The temperature dependence of the CDW incommensurability of $K_{0.3}MoO_3$ taken from neutron scattering data. [55]

4.5.2 The interaction of the CDW with impurities and other lattice defects

If the CDW's wavelength (λ_c) is incommensurate with the lattice period, then the main pinning centers are the impurities and other lattice defects. [2] The effect of impurities on the CDW phenomena has been the subject of great interest. The dynamics of the CDW have been studied in the frame of the Fukuyama-Lee-Rice model, in which the CDW is considered to be deformable (not rigid) to minimize its interaction with impurities. [83] This model is explained briefly in the next section.

4.5.3 The deformable CDW and CDW domains

The CDW is described by a modulation of the charge density, as shown in Eq. 4.6. $\overline{\rho}$ is the uniform density, ρ_0 is the amplitude of the CDW, and Q = 2K$_F$ is the wave vector. The phase ϕ describes the position of the CDW with respect to the underlying lattice. [83]

$$\rho(x) = \overline{\rho} + \rho_0 cos(Qx + \phi) \tag{4.6}$$

It had been first pointed out by Froehlich that if the CDW wave vector is incommensurate with the lattice vector, then the energy of the CDW state does not depend on its position with respect to the underlying lattice, i.e, independent of ϕ. In that case the CDW can slide easily through the lattice without any resistance. [83] Nevertheless after that Lee, Rice, and Anderson et al. [84] have figured out that there is an interaction between the impurity potential and the CDW phase even in the incommensurate state. This interaction is a kind of strong, so that they have concluded that the CDW is pinned by the impurity potential. So the resistance against the CDW sliding is no longer zero in the incommensurate state. [83] Fukuyama and Lee in Ref. [83] have studied the impurities effect on the CDW dynamics; they have neglected the CDW amplitude fluctuations, so the only variable in their study has been the CDW phase, i.e., they have studied the effect of impurities on the CDW phase. They have been able in their study to treat two cases of the impurities effect; the weak-impurity-scattering limit and the strong one. [83] Although Sokoloff in Ref. [85] had claimed that weak impurities do not pin the CDW, the results of Fukuyama and Lee have shown that even in the weak-impurity-scattering limit the CDW is pinned since the linear conductivity is concerned. [83]

The model of Fukuyama and Lee:

They have shown that the interaction between the CDW and randomly distributed impurities involves two competitive energies:

1. The elastic energy $E_{Elastic}$, which indicates how much the CDW is able to be stretched or compressed by the pinning centers created by the impurities.
2. The impurity energy $E_{Impurity}$.

Based on that they have then introduced the dimensionless parameter shown in Eq. 4.7, which is called the impurity strength parameter. [83]

$$\epsilon = \frac{E_{Impurity}}{E_{Elastic}} \tag{4.7}$$

So ϵ has been the criterion for Fukuyama and Lee to treat two extreme cases of the impurity scattering separately: [83]

1- Strong pinning case ($\epsilon \gg 1$):

The strong-impurity-scattering limit is achieved by having a strong impurity potential, meaning that the impurity energy is bigger than the elastic energy. In this case the impurity potential dominates, then it is expected that the CDW distorts by adjusting its phase at each impurity site. This means that the impurity potential is strong enough to fix the CDW phase at the pinning centers created by the impurities, thus the CDW is distorted and pinned by the pinning centers. [83]

2- Weak pinning case ($\epsilon \ll 1$):

The weak-impurity-scattering limit is achieved by having a weak impurity potential, meaning that the elastic energy is bigger than the impurity energy. In this case the elastic energy dominates and the impurity potential is not strong enough to fix the CDW phase at the pining centers, but the phase will be just slowly varying at each impurity site. Nevertheless, it has been shown by Fukuyama and Lee that even in this case the CDW can distort to take advantage of fluctuations in the impurity distribution by breaking the system into domains. [83]

So as a summary; Fukuyama and Lee have focused in their study on the phase fluctuations and shown the following: when the material is characterized by a weak impurity pinning, then the system is not rigid and can be thought to break into domains. Each domain has a length (L) along the chain axis (the so-called Fukuyama-Lee-Rice domain length). [83] Now this is the question: are our studied Rb- and W-doped blue bronze crystals characterized by a weak impurity pinning?. To see the answer please go through the argument below.

The pinning strength of our studied samples:

The threshold fields of V- and W-doped blue bronze crystals have been measured at 77 K by Ravy et al. [86]. The threshold field of the V-doped crystal is about 20 V/cm, while for the W-doped crystal is about 0.25 V/cm. The two crystals have about the same impurity concentration. Nevertheless the big difference between the values of the threshold fields of the V- and W-doped crystals having about the same impurity concentration suggests that the V dopant has to be considered as a strong pinning. While the W dopant is a weak pinning. [86] Our studied W-doped crystal has a lower impurity concentration. The threshold fields of our studied pure, Rb-, and W-doped crystals are on the same order of magnitude, so we would say that our studied crystals are characterized by a weak impurity pinning.

So we are able now to apply the model of Fukuyama and Lee, mentioned above in a simple model as used by Sirbu et al. [87] to describe the observed nonlinear transport in our studied samples. We do treat the sample as a collection of domains. Each domain is characterized by its own conductivity and threshold field, so that the sample can be considered as a collection of parallel and series conduction paths. At low applied external electric fields (smaller than E_T) excited quasiparticles thermally across the gap dominate the conductivity of a single domain, leading to the strongly temperature dependent ohmic behavior. All CDW domains are pinned and will not start moving until the applied external electric field exceeds a certain critical field (E_T). Then some domains become depinned and slide through the sample, leading to an additional CDW contribution to the conductivity (the typical nonlinear CDW conduction). The CDW still can not move as a whole, because of the domain structure. The sample is now in the incoherent moving regime. Finally for applied external electric fields exceeding a second critical field ($E_T{}^*$), the CDW may move as a whole resulting in a huge increase of the conductivity. The sample is now in the coherent moving regime and the conductivity becomes mostly dominated by the CDW transport. [87] Within this picture the nature of the second threshold field, observed in our studied samples is understood.

4.5.4 The single-particle current

Normal charge carriers do excite thermally across the Peierls energy band gap (like in semiconductors), resulting in a current flow (normal current). Just below the Peierls transition temperature, the normal current is large because of the high density of the normal charges which are thermally excited across the gap. The excitation of the normal charges across the gap is temperature dependent; it decreases with lowering the temperature, resulting in a decrease of the normal current with lowering the temperature. [2] When the CDW is not sliding ($E < E_T$), then the conductivity is ohmic and dominated by the normal current. But when the CDW is sliding, then the conductivity increases nonlinearly due to the additional CDW current. The normal carriers are supposed to screen the pinning centers caused by the impurities and lattice defects, reducing the pinning strength. [87] Within this picture; the first and second threshold fields should increase when the temperature is lowered, evidencing a strengthening of the CDW pinning. This is due to the reduction of the normal carriers concentration at lower temperatures, leading to a less effective screening of the pinning centers. This is in good agreement with our data. Also within this picture; the normal current I_N decreases with lowering the temperature, because of the temperature dependence of the normal current. This is also in good agreement with our data. The normal electrons are supposed to damp the CDW itself, because they do screen the the accumulated charges associated with the CDW distortion. This has been theoretically predicted by Sneddon in Ref. [88]. [89]. Within this picture the CDW current I_{CDW} increases with lowering the temperature, since the CDW damping by the normal electrons decreases with lowering the temperature because of the temperature dependence of the normal current as mentioned above. This is also in good agreement with our data.

4.5.5 The observed hysteresis

The observed path dependence in E_T(T) and $E_T{}^*$(T) is due to some error bar in the analysis and measurements. So there are only two kinds of hysteresis, observed in our studied samples:

1. The observed hysteresis in the I-V curves: this kind of hysteresis is for us puzzling, but we would attribute that to the CDW metastability. The temperature dependence of the hysteresis, illustrated in Fig. 4.25 is for us puzzling. But we would correlate that to the temperature dependence of the normal carriers concentration, as mentioned above; the free carriers are supposed to screen the pinning centers cause by impurities and other lattice defects, reducing the pinning strength. [87] Within this picture the pinning strength due to the pinning

centers caused by impurities and other lattice defects increases when the temperature is lowered, leading to a strengthening of the CDW pinning by those pinning centers. The metastability of the CDW is due to the pinning centers, caused by impurities and other lattice defects (see Refs. [63] and [90]). So the metastability effect increases with lowering the temperature. Also I would mention here that the anticlockwise loop of paths 0-P and P-0 (see Fig. 4.14) seems to be due to the thermal effect, but the temperature has been always stable over the whole voltage range at all temperature for all studied sample. Fig. 4.46 shows the stability of temperature of path N-P in the pure blue bronze sample, while measuring the I-V response (see also Figs. .6, .7, .8, .9, and .10 in the appendix).

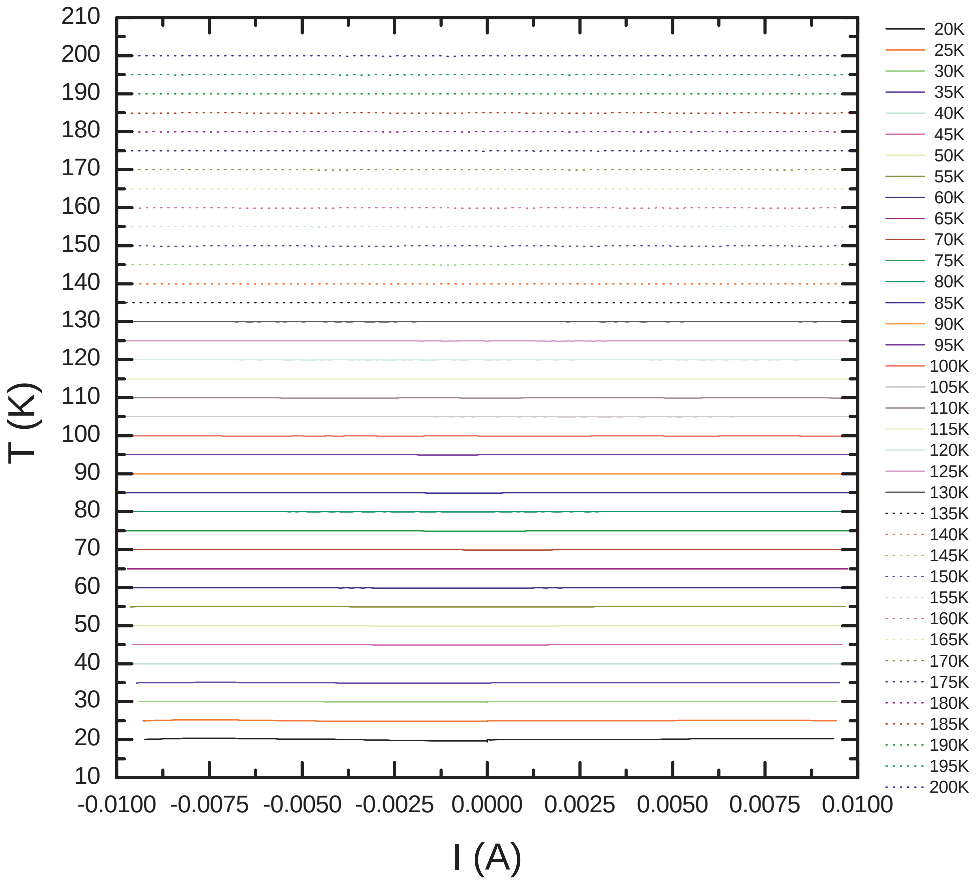

Figure 4.46: The stability of temperatures of path N-P in the pure blue bronze sample, while measuring the I-V response.

2. The observed hysteresis in R(T) of our studied pure and Rb-doped blue bronze samples: we know from the theory chapter (see the thermal memory effect section

in the theory chapter) that R(T) in the blue bronze shows a hysteresis, while cooling down and warming up below the Peierls transition temperature. This kind of hysteresis has been attributed to the presence of defects. If we take a look at Fig. 4.26, we will see that the hysteresis is bigger in the case of the Rb-doped sample than that of the pure sample. While no hysteresis has been observed in the W-doped blue bronze sample. So the concentration of defects is the highest in the case of the Rb-doped sample, while it is the lowest in the W-doped sample. We know previously that defects are one cause of the pinning centers, which do pin the CDW. This could explain why the absolute values of E_T(T) and $E_T{}^*$(T) are the highest in the case of the Rb-doped sample, while they are the lowest in the case of the W-doped sample (see Figs. 4.21 and 4.24).

5 Conclusions

In order to investigate the doping effects on the blue bronze $K_{0.3}MoO_3$, we have studied the electronic transport properties and the temperature dependence of the dc resistivity of pure, W-doped, and Rb-doped blue bronze single crystal samples. The temperature dependence of the dc resistivity of the pure sample has shown the Peierls metal-insulator phase transition at 180 K, where the transition is very sharp. The rubidium doping shifts the transition temperature to a lower temperature (170 K) and smears out the metal-insulator phase transition, i.e., the rubidium doping broadens the transition peak. Compared with the rubidium doping, the tungsten doping broadens the transition peak more and shifts the transition temperature to a lower temperature (140 K). The non-linear transport properties of pure, Rb-doped, and W-doped blue bronze single crystals have shown a nonlinear conductivity due to an incoherent CDW sliding, when the applied electric field exceeds the first threshold field (E_T). Furthermore, above a second threshold field ($E_T{}^* > E_T$) a coherent CDW-sliding sets in. For all studied materials E_T and $E_T{}^*$ increase monotonically with lowering the temperature. This finding is discussed mainly in terms of the incommensurate-commensurate transition of the CDW. The coherent and incoherent CDW movements are discussed within the frame of the Fukuyama-Lee-Rice model. The observed hysteresis in R(T) is attributed to the presence of defects. The path dependence of $E_T(T)$ and $E_T{}^*(T)$ is due to some error bar in the analysis and measurements.

Appendix

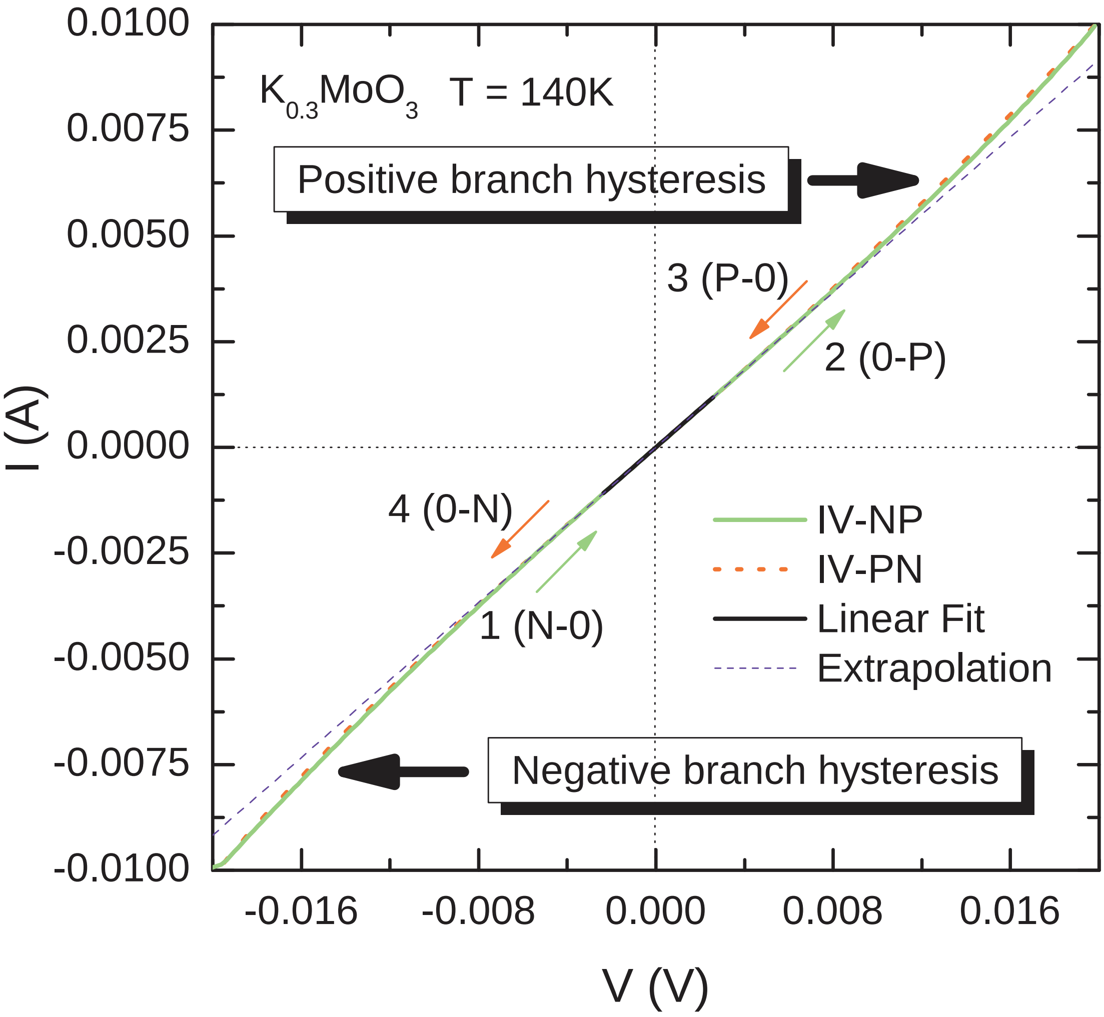

Figure .1: The I-V characteristics curves of the pure blue bronze at 140 K for the N-P and P-N paths. Path N-P means paths N-0 and 0-P, while path P-N means path P-0 and 0-N.

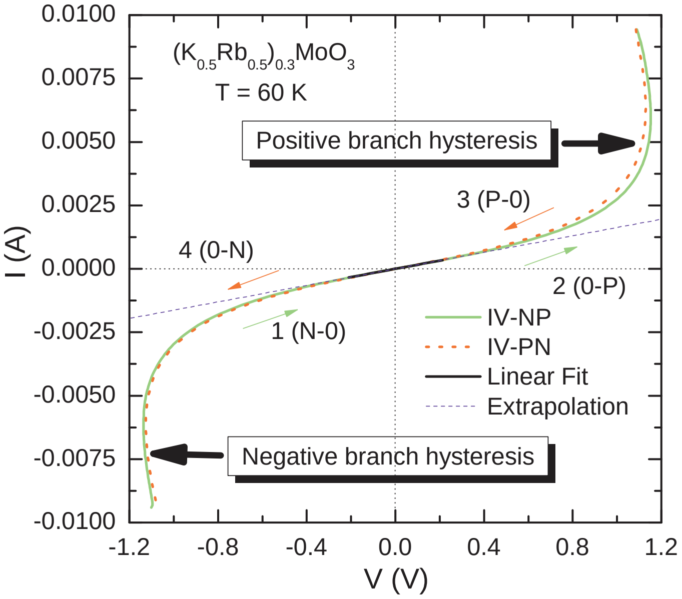

Figure .2: The I-V characteristics curves of the Rb-doped blue bronze at 60 K for the N-P and P-N paths. Path N-P means paths N-0 and 0-P, while path P-N means path P-0 and 0-N.

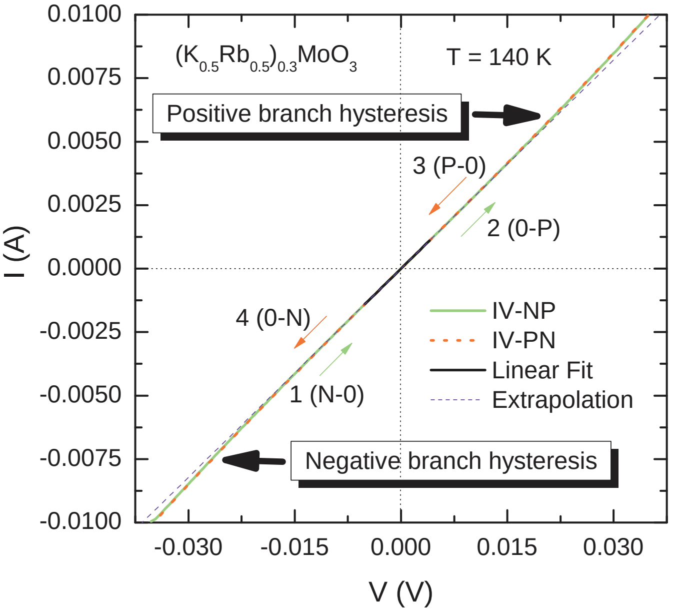

Figure .3: The I-V characteristics curves of the Rb-doped blue bronze at 140 K for the N-P and P-N paths. Path N-P means paths N-0 and 0-P, while path P-N means path P-0 and 0-N.

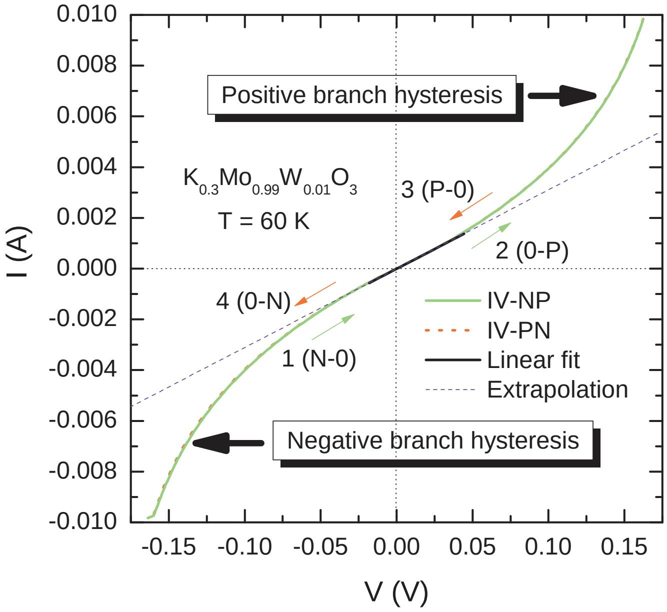

Figure .4: The I-V characteristics curves of the W-doped blue bronze at 60 K for the N-P and P-N paths. Path N-P means paths N-0 and 0-P, while path P-N means path P-0 and 0-N.

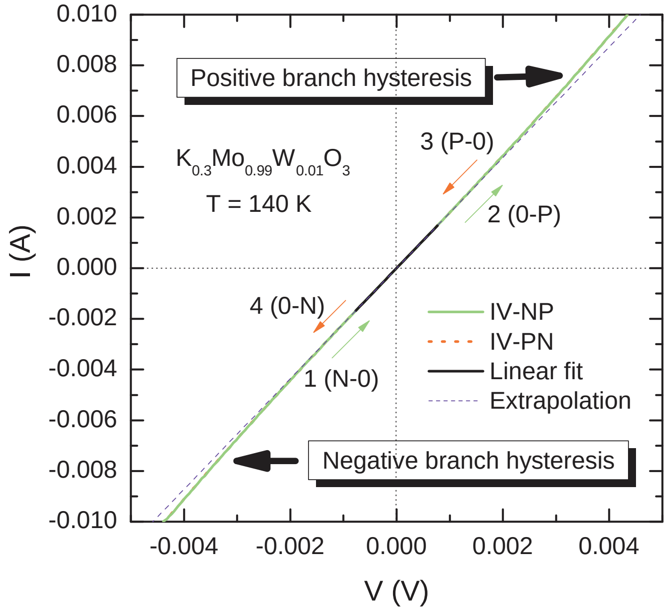

Figure .5: The I-V characteristics curves of the W-doped blue bronze at 140 K for the N-P and P-N paths. Path N-P means paths N-0 and 0-P, while path P-N means path P-0 and 0-N.

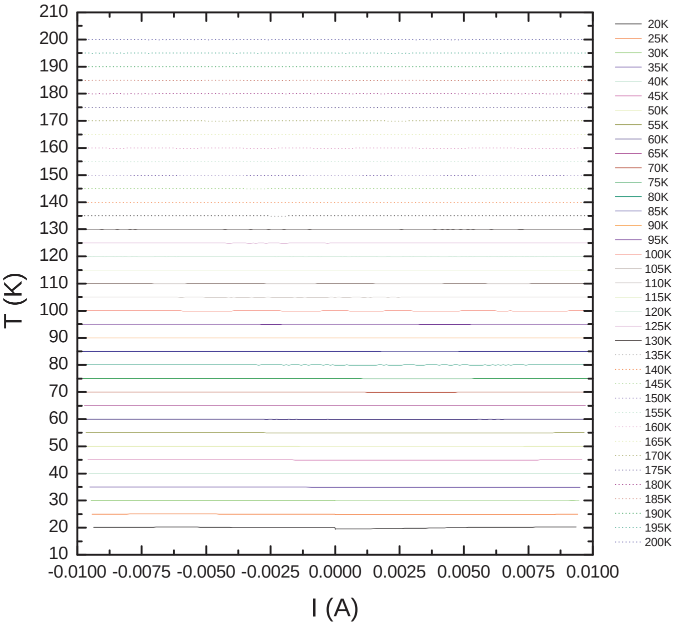

Figure .6: The stability of temperatures of path P-N in the pure blue bronze sample, while measuring the I-V response.

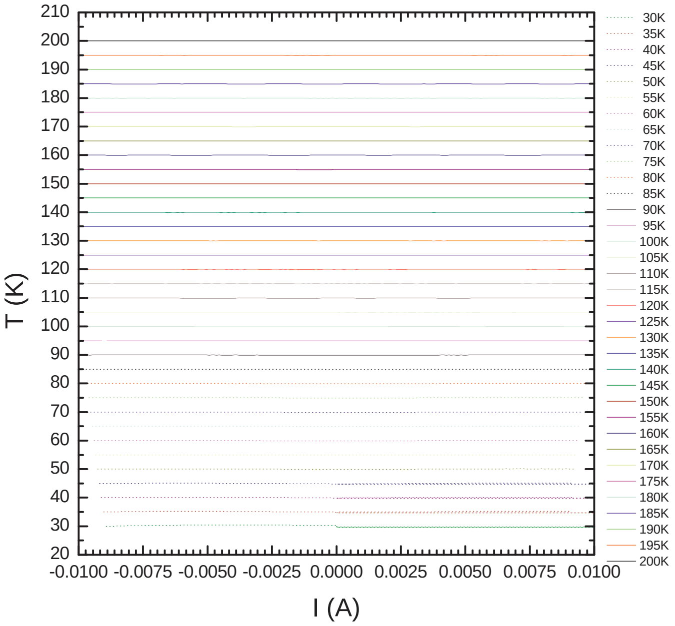

Figure .7: The stability of temperatures of path N-P in the Rb-doped blue bronze sample, while measuring the I-V response.

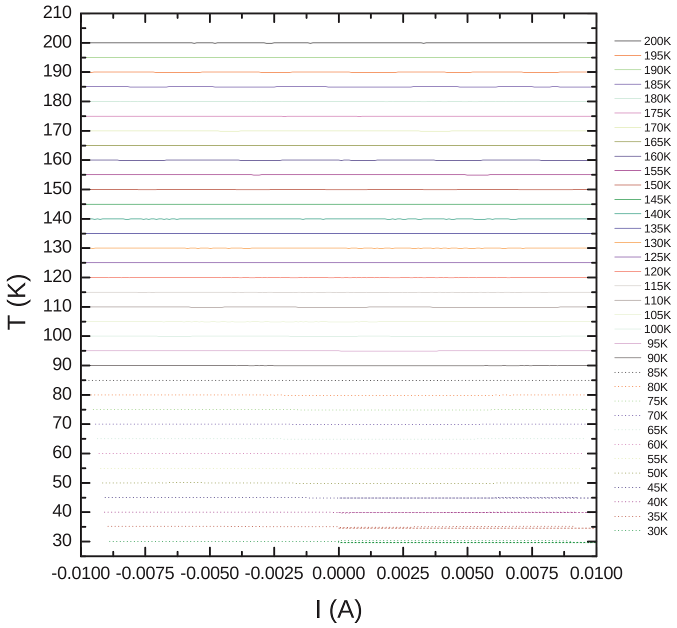

Figure .8: The stability of temperatures of path P-N in the Rb-doped blue bronze sample, while measuring the I-V response.

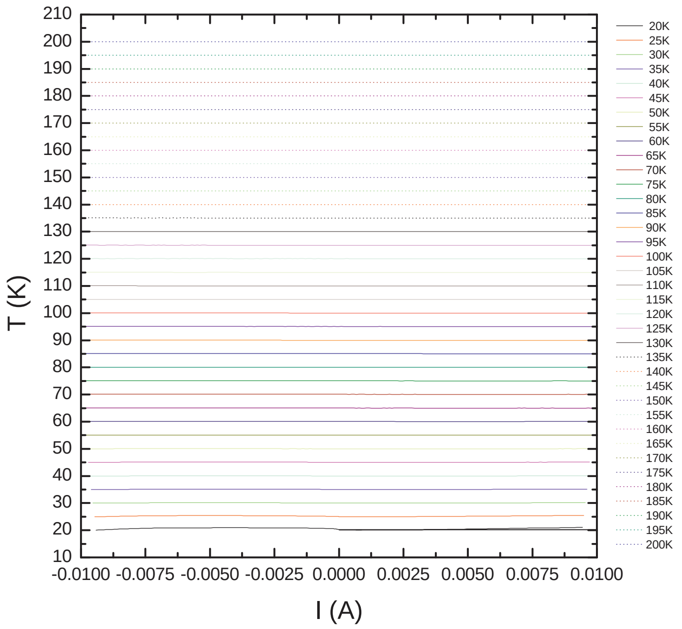

Figure .9: The stability of temperatures of path N-P in the W-doped blue bronze sample, while measuring the I-V response.

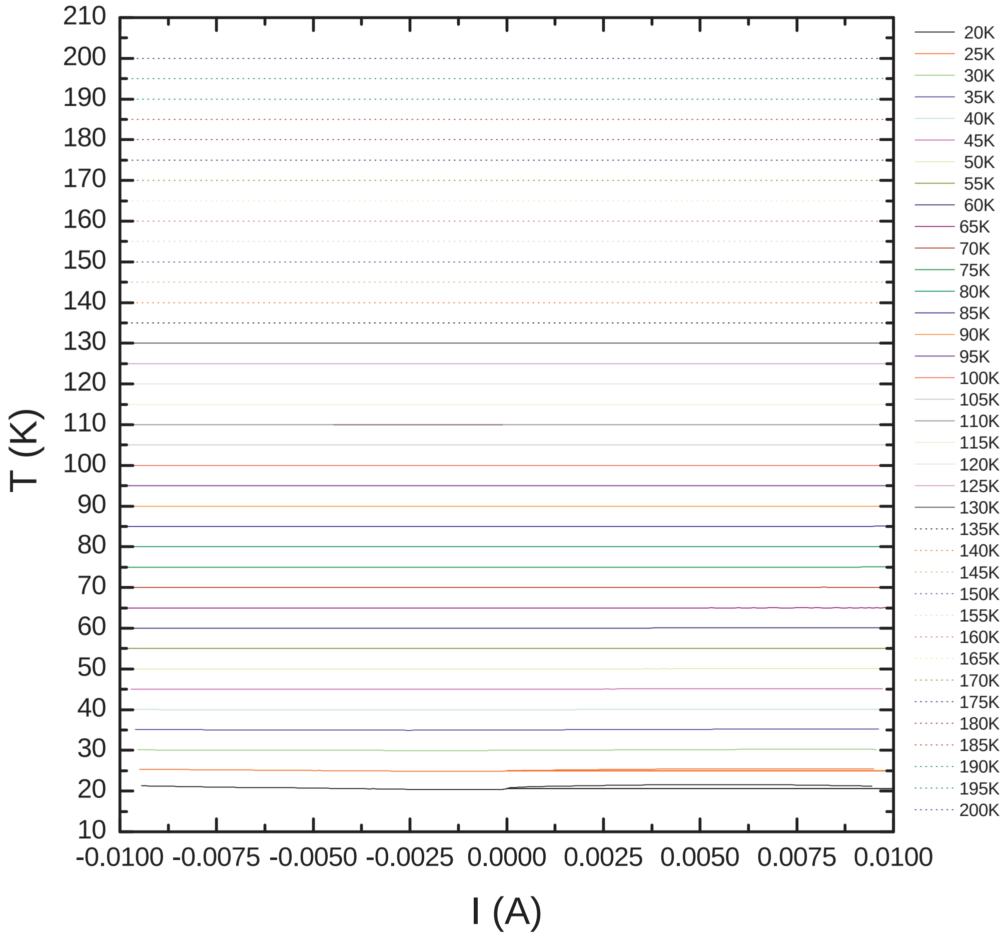

Figure .10: The stability of temperatures of path P-N in the W-doped blue bronze sample, while measuring the I-V response.

Bibliography

[1] S. Kagoshima, H. Nagasawa, and T. Sambongi, One-Dimensional Conductors (Germany: Springer-Verlag Berlin Heidelberg, 1988).

[2] Charge-Density-Wave Conductors, R. E. Thorne, Physics Today, May 1996, p. 42.

[3] Siegmar Roth, One-Dimensional Metals (Germany: VCH Verlagsgesellschaft mbH, Weinheim, 1995).

[4] R. Zallen, The Physics of Amorphous Solids (New York: John Wiley and Sons, 1983).

[5] R. E. Peierls, Quantum Theory of Solids (Oxford: Clarendon Press, 1955).

[6] Claire Schlenker, Low-Dimensional Electronic Properties of Molybdenum Bronzes and Oxides (Kluwer Academic Piblishers, The Netherlands, 1989).

[7] J. Dumas, C. Schlenker, J. Marcus, and R. Buder, Phys. Rev. Lett. **50**, 757 (1983).

[8] G. Mihaly and P. Beauchene, Solid State Commun. **63**, 911 (1987).

[9] P. B. Littlewood, Solid State Commun. **65**, 1347 (1988).

[10] S. Martin, R. M. Fleming, and L. F. Schneemeyer, Phys. Rev. B **38**, 5733 (1988).

[11] Wohler F., Philos. Mag. **66**, 263 (1825).

[12] D. W. Bullett, Theoretical Aspects of Band Structures and Electronic Properties of Pseudo-One-Dimensional Solids, ed. by H. Kamimura (Dordrecht: D. Reidel Publ., 1985).

[13] A. Wold, W. Kunnmann, R. J. Arnott, and A. Ferretti, Inorg. Chem. **3**, 545 (1964).

[14] G. H. Bouchard, J. Perlstein, and M. J. Sienko, Inorg. Chem. **6**, 1682 (1967).

[15] D. S. Perloff, M. Vlasse, and A. Wold, J. Phys. Chem. Solids **30**, 1071 (1969).

[16] P. Hagenmuller, Preparative Methods in Solid State Chemistry (ed. P. Hagenmuller), Academic Press, p. 279 (1972).

[17] W. A. Mumme and J. A. Watts, J. Solid State Chem. **2**, 16 (1970).

[18] A. F. Reid and J. A. Watts, J. Solid State Chem. **1**, 310 (1970).

[19] P. Strobel and M. Greenblatt, J. Solid State Chem. **36**, 331 (1981).

[20] R. Brusetti, B. K. Chakraverty, J. Devenyi, J. Dumas, J. Marcus, and C. Schlenker: Recent Developments in Condensed Matter Physics, ed. by J. T. Devreese, L. F. Lemmens, V. E. Van Doren, and J. Van Royen (Plenum, New York, 1982), **vol. 2**, p. 181.

[21] R. Buder, J. Devenyi, J. Dumas, J. Marcus, J. Mercier, C. Schlenker, and H. Vincent, J. Physique Lett. **43**, 59 (1982).

[22] L. F. Schneemeyer, S. E. Spengler, F. J. DiSalvo, J. V. Waszczak, and C. E. Rice, J. Solid State Chem. **55**, 158 (1984).

[23] L. F. Schneemeyer, F. J. DiSalvo, R. M. Fleming, and J. V. Waszczak, J. Solid State Chem. **54**, 358 (1984).

[24] J. P. Pouget, S. Kagoshima, C. Schlenker, and J. Marcus, J. Physique Lett. **44**, L113 (1983).

[25] L. F. Schneemeyer, F. J. DiSalvo, S. E. Spengler, and J. V. Waszczak, Phys. Rev. B **30**, 4297 (1984).

[26] C. Schlenker, C. Dumas, C. Escribe-Filippini, H. Guyot, J. Marcus, gand J. Fourcaudot, Phil. Mag. B **52**, 643 (1985).

[27] M. Ganne, A. Boumaza, M. Dion, and J. Dumas, Mat. Res. Bull. **20**, 1297 (1985).

[28] J. -M. Reau, C. Fouassier, C. Gleitzer, and M. Parmentier, Bull. Soc. Chim. Fr., p. 479 (1970).

[29] J. -M. Reau, C. Fouassier, and P. Hagenmuller, J. Solid State Chem. **1**, 326 (1970).

[30] J. -M. Reau, C. Fouassier, and P. Hagenmuller, Bull. Soc. Chim. Fr., p. 2883 (1971).

[31] W. H. McCarroll and M. Greenblatt, Solid State Chem. **54**, 282 (1984).

[32] K. V. Ramanujachary, M. Greenblatt, and W. H. McCarroll, Cryst. Growth **70**, 476 (1984).

[33] B. T. Collins, K. V. Ramanujachary, M. Greenblatt, and J. V. Waszczak, Solid State Commun. **56**, 1023 (1985).

[34] K. V. Ramanujachary, B. T. Collins, M. Greenblatt, and J. V. Waszczak, Solid State Commun. **59**, 647 (1986).

[35] K. V. Ramanujachary, B. T. Collins, M. Greenblatt, P. McNally, and W. H. McCarroll, Solid State Ionics **22**, 105 (1986).

[36] B. T. Collins, K. V. Ramanujachary, M. Greenblatt, W. H. McCarroll, P. McNally, and J. V. Waszczak, J. Solid State Chem. **76**, 319 (1988).

[37] J. Graham and A. D. Wadsley, Acta Cryst. **20**, 93 (1966).

[38] M. Ghedira, J. Chenavas, M. Marezio, and J. Marcus, Solid State Chem. **57**, 300 (1985).

[39] W. J. Schutte and J. L. De Bore, Acta Cryst. B **49**, 579 (1993).

[40] W. H. Zachariasen, J. Less Comm. Met. **62**, 1 (1978).

[41] Di Yin, Jianbo Wang, Renhui Wang, Jing Shi, and Huamin Zou, J. Phys.: Condens. Matter **16**, 9001 (2004).

[42] H. M. Tsai, K. Asokan, C. W. Pao, J. W. Chiou, C. H. Du, and W. F. Pong, Applied Physics Letters **91**, 022109 (2007).

[43] J. B. Goodenough, Czech. J. Phys. B **17**, 304 (1967).

[44] P. G. Dickens and D. J. Neild, Trans. Faraday Soc. **64**, 13 (1968).

[45] G. Sperlich, Z. Physik **250**, 335 (1972).

[46] V. A. Joffe and I. V. Patrina, Sov. Phys. Sol. State **10**, 639 (1968).

[47] Jose-Luis Mozos, Pablo Ordejon and Enric Canadell, Phys. Rev. B **65**, 233105 (2002).

[48] C. Schlenker, J. Dumas, C. Escribe-Filippini, H. Guyot, J. Marcus , and G. Fourcaudot, Philos. Mag. B **52**, 643 (1985).

[49] W. Bruetting, P. H. Nguyen, and W. Reiß, Phys. Rev. B **51**, 9533 (1995).

[50] G. Travaglini, I. Moerke, and P. Wachter, Solid State Commun. **45**, 289 (1983).

[51] Mitsuharu Nagasawa, Tokiko Nakasawa, Koichi Ichimura, and Kazushige Nomura, Physica B **404**, 392 (2009).

[52] G. Remenyi and J. Dumas, Physics Letters A **373**, 4278 (2009).

[53] M. Sato, Lect. Notes Phys. **217**, 7 (1985).

[54] M. Sato, H. Fujishita, and S. Hoshino, J. Phys. **16**, L877 (1983).

[55] R. M. Fleming, L. F. Schneemeyer, and D. E. Moncton, Phys. Rev. B **31**, 899 (1985).

[56] D. C. Johnston, Phys. Rev. Lett. **52**, 2049 (1984).

[57] H. Froehlich, Proc. R. Soc. A **223**, 296 (1954).

[58] Martha Greenblatt, Chem. Rev. **88**, 31 (1988).

[59] J. Dumas, C. Schlenker, J. Marcus, and R. Buder, Phys. Rev. Lett. **59**, 757 (1983).

[60] J. C. Gill, Solid State Commun. **39**, 1203 (1981).

[61] R. M. Fleming, Solid State Commun. **43**, 167 (1982).

[62] R. M. Fleming and L. F. Schneemeyer, Phys. Rev. B **28**, 6996 (1983).

[63] H. Mutka, F. Rullier-Albenque, and S. Bouffard, J. Physique **48**, 425 (1987).

[64] G. Travaglini, P. Wachter, J. Marcus, and C. Schlenker, Solid State Commun. **37**, 599 (1981).

[65] S. Jandl, M. Banville, and C. Pepin, Phys. Rev. B **40**, 12487 (1989).

[66] Introduction to Fourier Transform Infrared Spectroscopy @ 2001 Thermo Nicolet Corporation.

[67] Barbara Stuart, Infrared Spectroscopy: Fundamentals and Applications (John Wiley and Sons, 2004).

[68] IFS 66v/S User's Manual.

[69] HYPERION User Manual.

[70] Mark Fox, Optical Properties of Solids (Oxford University Press, 2001).

[71] Christopher C. Homes, M. Reedyk, D. A. Cradles, and T. Timusk, Applied Optics **32**, 2976 (1993).

[72] Bedienungsanleitung, KONTI-Kryostat, Typ Spektro A-HT, Kom.Nr.6872-03

[73] H. -D. Liu, Y. -P. Zhao, G. Ramanath, S. P. Murarka, and G. -C. Wang, Thickness dependent electrical resistivity of ultrathin (<40 nm) Cu Films, Thin Solid Films **384**, 151 (2001).

[74] SQM-160, Rate/Thickness Monitor, User's Guide, Version 3.05 @ Copyright Sigma Instruments, Inc. 2000-2007.

[75] S. Yue, C. A. Kuntscher, M. Dressel, S. van Smaalen, F. Ritter, and W. Assmus, Doping Effects on the Charge-Density-Wave Dynamics in Blue Bronze, arXiv:cond-mat/0501332v1 (2005).

[76] Douglas Vaughan, An introduction to Energy-Dispersive X-Ray Microanalysis (Noran Instruments, 1999).

[77] B. D. Cullity, Elements of X-Ray Diffraction, Second Edition (Addison-Wesley Publishing Company, 1978).

[78] K. Carneiro, Electronic Properties of Inorganic Quasi-One-Dimensional Compounds, p.44 (Dordrecht, Reidel, 1985).

[79] B. Zawilski, J. Marcus, and T. Klein, Europhys. Lett. **50**, 75 (2000).

[80] Rui Xiong, Dahua Li, Junfeng Wang, Changzheng Li, Wufeng Tang, and Jing Shi, Solid State Commun. **142**, 251 (2007).

[81] K. T. Tsutsumi, T. Tamegai, S. Kagoshima, and M. Sato, J. Phys. Soc. Japan **54**, 3004 (1985).

[82] R. M. Fleming, R. J. Cava, L. F. Schneemeyer, E. A. Rietman, and R. G. Dunn, Phys. Rev. B **33**, 5450 (1986).

[83] H. Fukuyama and P. A. Lee, Phys. Rev. B **17**, 535 (1978).

[84] P. A. Lee, T. M. Rice, and P. W. Anderson, Solid State Commun. **14**, 703 (1974).

[85] J. B. Sokoloff, Solid State Commun. **16**, 375 (1975).

[86] S. Ravy, S. Rouzière, J. -P. Pouget, S. Brazovskii, J. Marcus, J. -F. Bérar, and E. Elkaim, Phys. Rev. B **74**, 174102 (2006).

[87] S. Sirbu, T. Yamauchi, Y. Ueda, and P. H. M. van Loosdrecht, Eur. Phys. B **53**, 289 (2006).

[88] Leigh Sneddon, Phys. Rev. B **29**, 719 (1984).

[89] G. Mihaly, P. Beauchene, J. Marcus, J. Dumas, and C. Schlenker, Phys. Rev. B **37**, 1047 (1988).

[90] P. Butaud, P. Segransan, C. Bethier, J. Dumas, and C. Schlenker, Phys. Rev. Lett. **55**, 253 (1985).

Acknowledgements

It is an extreme pleasure to thank my first supervisor (Prof. Dr. Christine Kuntscher) for always being my guidance by motivating me and providing me with a lot of information. I really appreciate the way she has supervised me. Also I would like to thank my second supervisor (Prof. Dr. Brütting) for his nice support. Many thanks to the people working at experimental physics 2 for their nice support. Also I would like to thank the people at the mechanical and electronic workshops at the institute of physics for their great technical support. Many thanks to the DAAD organization for the financial support. I never forget to thank my parents, brother, and my sisters for always being my invisible motivation during my stay in Germany. Also many thanks to my current and former group's members for their nice support. With all that I have been able to write these words at the end of my PhD thesis.

Curriculum Vitae

Personal information

Date of birth : 14 December 1980
Nationality : Iraqi
Gender : Male
Martial status : Single

Education

1998 - 2001	Bachelor's degree in laser engineering, Al-Nahrain University, Baghdad, Iraq. Title: *Atmospheric Effects on Infrared Radiations.*
2001 - 2004	Master's degree in laser engineering, Al-Nahrain University, Baghdad, Iraq. Title: *Study of Optical Modulation using Chopping Technique.*
2007 - Present	Start of Ph.D in Physics, Universität Augsburg, Augsburg, Germany. Title: *Dc transport and optical measurements on the charge-density-wave compounds* $(K, Rb)_{0.3}(Mo, W)O_3$.

List of publications

- *Doping effects on the non-linear transport in blue bronze.*
  A. Khairi Al-Hadeethi, D. Grund, Song Yue, Martin Dressel, and Christine Kuntscher,
  To be submitted.